Graphene-based FET biosensors

by

Inna Novodchuk

A thesis
presented to the University of Waterloo
in fulfillment of the
thesis requirement for the degree of
Doctor of Philosophy
in
Mechanical and Mechatronics Engineering (Nanotechnology)

Waterloo, Ontario, Canada, 2021

Examining Committee Membership

The following served on the Examining Committee for this thesis. The decision of the Examining Committee is by majority vote.

External Examiner	Professor Jinghua Guo Advanced Light Source, Lawrence Berkeley National Library, Berkeley, CA, US
Supervisor(s)	Professor Mustafa Yavuz Mechanical & Mechatronics Engineering, University of waterloo, ON, Canada
	Professor Michal Bajcsy Electrical & Computer Engineering, University of waterloo, ON, Canada
Internal Member	Professor Kevin Musselman Mechanical & Mechatronics Engineering, University of waterloo, ON, Canada
Internal-external Members	Professor Irene Goldthorpe Electrical & Computer Engineering, University of waterloo, ON, Canada
	Professor Eihab Abdel-Rahman Systems Design Engineering, University of waterloo, ON, Canada

Author's Declaration

I hereby declare that I am the sole author of this thesis. This is a true copy of the thesis, including any required final revisions, as accepted by my examiners.

I understand that my thesis may be made electronically available to the public.

Abstract

Graphene and graphene-based materials are highly attractive for field effect transistor (FET) applications because of their elevated theoretical charge carrier mobility. Graphene FETs (GFETs) are studied for biosensing applications for their high sensitivity and fast detection times. However, beyond theory, the state-of-the-art GFETs have very low charge carrier mobilities and low ON and OFF current (I_{ON}/I_{OFF}) ratios. The reduced electrical performance of the reported GFETs hinders their use for sensitive biosensor applications. In this work, a femtosecond laser beam was used to fabricate functional graphene-based materials and to tune their structure and electrical performance. It was found that the laser ablation process could transform two insulating two-dimensional (2D) materials, graphene oxide (GO) and hexagonal boron nitride (h-BN), into semiconductors with high I_{ON}/I_{OFF} ratios and charge carrier mobilities.

Two types of nanomaterials were fabricated using a laser ablation process. The first is B and N co-doped reduced GO (rGO) nanoflakes, and the second is B and N co-doped GO (BN-GO) gels. The co-doping concentration was controlled by changing the ratio between GO and h-BN in the precursor solutions. Greater B-doping concentrations were observed for the nanoflakes (1.8-4.1 at%) compared with the gels (0.5-1.3 at%). Similarly, greater nitrogen doping was observed for the nanoflakes (3.4-5.9 at%) compared with the gels (0.3-1 at%). Increased B and N co-doping concentrations were found to reduce the sheet resistance of the nanoflakes.

Back-gated FET devices made of the BN-GO gels revealed very high I_{ON}/I_{OFF} ratios (~10^6) and electron and hole mobilities in the range of 3000-9000 $cm^2V^{-1}s^{-1}$ and 2000-6000 $cm^2V^{-1}s^{-1}$, respectively. Several electrical performance enhancement strategies were employed, and the best mobility and I_{ON}/I_{OFF} ratio values achieved were 440,000±200,000 $cm^2V^{-1}s^{-1}$ and 10^7, respectively. These values were obtained when the pulse duration of the laser ablation was reduced by 3 times to approximately 10 fs. These gels demonstrated good stability over a 2-year period.

The BN-GO gels were used for several sensing and biosensing applications. For gas sensing, the BN-GO gels were used as the receptor material in a membrane-type surface stress (MSS) sensor. It was found that the sensitivity of the sensor is enhanced for gels containing higher concentrations of B and N co-doping. Additionally, MSS using BN-GO gels demonstrated an improved limit of detection (LOD) for most tested compounds compared to other 2D receptors.

An FET with the BN-GO gel as top-channels were used for the biosensing of brain natriuretic peptide (BNP), a heart failure (HF) biomarker, and Coronavirus disease 2019 (COVID-19) synthetic proteins in buffer. The BN-GO gel channels were covalently functionalized with BNP or COVID-19 antibodies to selectively capture the desired analytes. It was found that real-time detection of BNP biomarker in buffer could be achieved in as little as 5 seconds with an LOD of 10 fM and a detection range of 10 fM – 1 pM. The Dirac point monitoring of the same biosensor revealed an LOD of 10 aM within 2 minutes and a detection range of 10 aM – 1 µM. The biosensor demonstrated great specificity and selectivity compared with K^+ OH^- ions and human epidermal growth factor receptor 2 (HER2) cancer biomarker protein.

The BN-GO gel FET covalently functionalized with COVID-19 antibodies was used for COVID-19 biosensing in buffer as a proof-of-concept by monitoring the shift in the Dirac point. The LOD and detection range were calculated as ~30 fg/mL and 0.01-100 pg/mL, respectively for COVID-19 protein in a 0.1x pH=7 buffer solution. The BNP and COVID-19 biosensors should be further investigated beyond the proof-of-concept stage. Additionally, other biomarker-bioreceptor pairs could also be investigated using the same BN-GO gel FET platform. Aptamers may be studied as a replacement for the antibody bioreceptors for improved sensitivity.

Acknowledgements

I would like to thank the following people, without whom I would not have been able to complete this research, and without whom I would not have made it through my Ph.D. degree:

First, my supervisors prof. Mustafa Yavuz and prof. Michal Bajcsy, for their enthusiasm for the project, for their support and encouragement, and for the freedom they have provided. I am especially grateful for the opportunity to work in this field.

Prof. Eihab M. Abdel-Rahman, prof. Kevin P. Musselman, and prof. Joseph Sanderson, for providing me access to their labs and for their guidance.

Prof. Goldthorpe and prof. Tang for editing advice and resources.

Dr. Z. Essen and Dr. M. Irannejad for their mentorship.

I. Prassas, Dr. D. Eleftherios, and A. Soosaipillai, for resources and their time.

Dr. M. Snowdon for editing.

I would also like to thank the following agencies for their financial contribution:

CMC Microsystems (MNT award), OGS, NSERC, and Ontario Ministry of Research and Innovation.

Dedication

I would like to dedicate this thesis to my husband and daughter, David and Abigail, who inspire me to be my best self every day.

Table of Contents

List of Figures

List of Tables

List of Abbreviations

BG	Back-gated
BN-GO	B and N co-doped GO
BNP	Brain natriuretic peptide
CG	crumpled graphene
CMOS	Complementary-metal-oxide-semiconductor
COVID-19	Coronavirus disease 2019
CSPG4	Chondroitin sulfate proteoglycan 4
CVD	Chemical vapor deposition
D	Drain
e	Electron charge
EDC	N-(3-dimethylaminopropyl)-N′-ethylcarbodiimide hydrochloride
ELISA	enzyme-linked immuno-sorbent assay
FET	Field effect transistor
FLG	Few-layers graphene
GA	Glutaraldehyde
GFET	Graphene-based field effect transistor
GNM	Graphene nanomesh
GO	Graphene oxide
h-BN	Hexagonal boron nitride
Hep-B	Hepatitis B
HER2	Human epidermal growth factor receptor 2
HF	Heart failure
HRTEM	High-resolution transmission electron microscopy
I_{ds}	Drain-source current
I_{OFF}	OFF current
I_{ON}	ON current
L	Channel length
LEG	Liquid exfoliated graphene

LOD	Limit of detection
MEH-PPV	Poly [2-methoxy-5-(2´-ethylhexyloxy-p-phenylenevinylene)]
miRNA	Micro-RNA
MSS	Membrane-type surface stress sensor
n	Electron concentration
NHS	N-hydroxysuccinimide
NPs	Nanoparticles
PBASE	1-Pyrenebutanoic acid succinimidyl ester
PNA	Peptide Nucleic Acid
QD	Quantum dot
rGO	Reduced graphene oxide
S	Source
ssDNA	Single-stranded DNA
t	Channel thickness
V_{DS}	Drain-source voltage
V_G	Gate voltage
VOC	Volatile organic compounds
W	Channel width
XPS	X-ray photo-electron spectroscopy
0D	Zero-dimensional
1D	One-dimensional
2D	Two dimensional
3D	Three-dimensional
μ_n	Electron mobility
σ	Electrical conductivity

List of publications

Peer reviewed journal articles

1. I. Novodchuk, M. Irannejad, B. Wales, K. Ibrahim, J. Sanderson, M. Bajcsy, M. Yavuz, Controlled volume production of simultaneously B/N co-doped reduced graphene oxide nanoflakes using femtosecond laser ablation, Mater. Res. Bull. 111 (2019) 80–86. doi:10.1016/j.materresbull.2018.10.039.

2. I. Novodchuk, M. Kayaharman, K. Ibrahim, S. Al-Tuairqi, M. Irannejad, E. Abdel-Rahman, J. Sanderson, M. Bajcsy, M. Yavuz, B/N co-doped graphene oxide gel with extremely-high mobility and ION/IOFF for large-area field effect transistors, Carbon N. Y. 158 (2020) 624–630. doi:10.1016/j.carbon.2019.11.034.

3. I. Novodchuk, M. Kayaharman, I.R. Ausri, R. Karimi, X.S. Tang, I.A. Goldthorpe, J. Sanderson, M. Bajcsy, M. Yavuz, An ultrasensitive heart-failure BNP biosensor using B/N co-doped graphene oxide gel FET, Biosens. Bioelectron. 180 (2021) 113114. doi:10.1016/j.bios.2021.113114.

4. K. Mistry, K.H. Ibrahim, I. Novodchuk, H.T. Ngo, G. Imamura, J. Sanderson, M. Yavuz, G. Yoshikawa, K.P. Musselman, Nanomechanical Gas Sensing with Laser Treated 2D Nanomaterials, Adv. Mater. Technol. 2000704 (2020) 1–11. doi:10.1002/admt.202000704.

5. K. Ibrahim*, I. Novodchuk*, K. Mistry*, M. Singh, C. Ling, J. Sanderson, M. Bajcsy, M. Yavuz, K.P. Musselman, Laser-Directed Assembly of Nanorods of 2D Materials, Small. 15 (2019) 1904415. doi:10.1002/smll.201904415.

(* indicates authors with equal contribution).

Review articles

1. I. Novodchuk, M. Bajcsy, M. Yavuz, Graphene-based field effect transistor biosensors for breast cancer detection: A review on biosensing strategies, Carbon N. Y. 172 (2021) 431–453. doi:10.1016/j.carbon.2020.10.048.

Book chapters

1. I. Novodchuk, A. Chakraborty, M. Irannejad, K. Musselman, M. Bajcsy, and M. Yavuz. Introduction chapter for "Nano and Micro-Electro- Mechanical Systems: Interconnections, Packaging, Testing and Reliability" book. (Chapter is complete, book is being prepared)

Conference abstracts

1. I. Novodchuk*, K. Ibrahim*, K. Mistry*, M. Singh, C. Ling, J. Sanderson, M. Bajcsy, M. Yavuz, and K. Musselman (2018). "Nanorods synthesis and Growth from 2D Materials Via Femtosecond Laser Treatment". International Symposium: Frontiers in Nanoscience and Nanotechnology – Waterloo, ON, Canada.

2. I. Novodchuk, M. Irannejad, B. Wales, J. Sanderson, Z. Esen, M. Yavuz, M. Bajcsy (2017). "Simultaneous boron and nitrogen co-doping and reduction of graphene oxide using femtosecond laser ablation". CSSTC 2017- Waterloo, ON, Canada.

3. Esen Z, Irannejad M, Novodchuk I, Wales B, Sanderson J. (2016). "Synthesis and characterization of reduced graphene oxide-gold hybrid nanostructures using femtosecond laser ablation". ICOOPMA 2016, page 34. ICOOPMA 2016- Polytechnique Montreal, Canada.

Posters

1. I. Novodchuk*, K. Ibrahim*, K. Mistry*, M. Singh, C. Ling, J. Sanderson, M. Bajcsy, M. Yavuz, and K. Musselman. "Nanorods synthesis and Growth from 2D Materials Via Femtosecond Laser Treatment". Presented at International Symposium: Frontiers in Nanoscience and Nanotechnology – Waterloo, ON, Canada.

2. I. Novodchuk, M. Irannejad, B. Wales, J. Sanderson, Z. Esen, M. Yavuz, M. Bajcsy (2017). "Simultaneous boron and nitrogen co-doping and reduction of graphene oxide using femtosecond laser ablation". Presented at CSSTC 2017- Waterloo, ON, Canada.

Chapter 1
Introduction

Heart disease and cancer are the two leading causes of death worldwide, responsible for more than 47% of overall causes of death (as of 2017) [1]. In recent years, another threat is causing a consistent rise in the number of deaths worldwide, i.e., Coronavirus disease 2019 (COVID-19) which claimed more than 2.7 million lives over the span of one year [2]. Experts agree that one of the best methods to improve the disease outcome [3] and reduce the spread of viral diseases is through early detection [4]. While much progress has been done to achieve a better understanding of early detection and screening measures, the common practices still lack the required sensitivity for early detection [5] and take a long time [6].

Field effect transistors (FETs) are one of the most promising biosensor types investigated in recent years since they offer point-of-care applications, high sensitivity, fast detection times, and compatibility with complementary metal-oxide-semiconductor (CMOS) fabrication [7]. The ability to detect a disease in its early stages is directly related to the sensitivity of the biosensor and its limit of detection (LOD). In FETs, the detection sensitivity and LOD are dictated by the electrical performance of the device, namely the charge carrier mobility and the ratio between the "ON" and "OFF" currents (I_{ON}/I_{OFF}) of the channel [8]. In addition, researchers demonstrated that the feature size also affects the device's sensitivity, with increased sensitivity reported for features in the nanometer scale [9]. For these reasons, a semiconductor nanomaterial with an increased charge carrier mobility and I_{ON}/I_{OFF} ratio is highly desired for FET biosensors.

Graphene is a two-dimensional (2D) nanomaterial with a superior theoretical charge carrier mobility above 200,000 $cm^2V^{-1}s^{-1}$ [10]. However, it is a semi-metal with a zero bandgap which eliminates its use in FETs [11]. Several approaches have been made to overcome this obstacle, such as increasing the number of layers [12], adding quantum confinement [13], or introducing stress [7]. Alternatively, graphene-based materials, such as graphene oxide (GO), reduced graphene oxide (rGO) [14], doped graphene [15], and graphene-based hybrids [16] were also studied. The highest reported charge carrier mobility (μ=36,000 $cm^2V^{-1}s^{-1}$) and I_{ON}/I_{OFF} ratio (~10^8) were achieved for graphene-based structures involving graphene and hexagonal boron nitride (h-BN) hybrids/heterostructures [17], [18]. However, common fabrication techniques require the use of harsh chemicals and lengthy processes and do not allow large-scale fabrication [13]. Therefore, it is crucial to develop a fast and CMOS-compatible fabrication technique of a graphene-based FET (GFET) with superior electrical performance. With the

correct functionalization strategies [19], these GFETs could be used as biosensors for the early detection of numerous diseases.

1.1 Objective of the thesis

The objective of the thesis is to develop a graphene-based FET that would serve as a platform for ultra-sensitive detection of various disease biomarkers. Several additional requirements are desired:

- Fast fabrication process without the use of harsh chemicals.
- High charge carrier mobilities and I_{ON}/I_{OFF} ratio.
- Good stability in room ambient conditions.
- Compatible for CMOS and large-scale fabrication.
- Compatible for different sensing and biosensing applications.

In this regard, two main goals were set. First, the fabrication of a FET device with superior electrical performance, and second, the functionalization of the device with different bioreceptor (biological capturing) molecules for selective biosensing.

1.1.1 FETs with superior electrical performance

Several approaches have been made to tailor the electrical performance of the FETs while striving to fulfill the above objectives. First, non-hazardous materials (i.e., GO and h-BN) were used throughout the thesis. These materials were chosen since graphene and h-BN hybrids were demonstrated to possess extremely-high charge carrier mobilities and I_{ON}/I_{OFF} ratios [17], [18] and increased stability in air [20]. GO is an oxygenated form of graphene with poor electrical conductivity, but reducing the oxygen content in GO could restore the electrical properties towards those of graphene [21]. Additionally, one milligram monolayer suspension of graphene costs $1100, almost 7000 times as much as one milligram of GO suspension [22].

For the second approach, laser ablation was chosen as the material processing platform, since it allows fast fabrication times in room ambient conditions [23]. Additionally, it was demonstrated as a reliable tool to reduce the oxygen content in GO. Tailoring the electrical performance of the devices was achieved through changes to the laser ablation process and changes to the ratio between the precursors. Lastly, the device fabrication processes used throughout the thesis are compatible with CMOS fabrication techniques.

1.1.2 Different biosensing platforms

A biosensor commonly has two key components: a bioreceptor and a transducer [19]. The bioreceptor is a biological molecule that can selectively recognize the target analyte in the sample and make a physical or chemical reaction with it. A transducer translates the recognition process into a measurable signal, i.e., an electrical signal in the case of a GFET. When the electrical signal is large enough to be measured, biosensing can occur. Therefore, it is theoretically possible to functionalize the GFET with different bioreceptors, as long as the recognition reaction between the analyte and the bioreceptor would generate a large enough electrical signal in the GFET.

1.2 Thesis structure

The thesis is divided into seven chapters. The organization and content of the thesis are as follows:

Chapter 2 will discuss the state-of-the-art pristine graphene and graphene-based materials, their common fabrication techniques, and their demonstrated electrical performance. Then, the working principle of FET biosensors will be presented. The biosensing performance of the state-of-the-art GFET will be compared, and the dependence of the biosensing results on the electrical performance of the GFET will be analyzed. Lastly, the challenges and opportunities the field is facing will be discussed.

Chapter 3 will present graphene-based materials fabricated by a simple and fast laser ablation technique in room ambient conditions. The compositional, structural, and electrical performance of the novel material will be analyzed. Their feasibility in GFETs will then be discussed.

Chapter 4 will present improvements to the fabrication process discussed in Chapter 3 and present a GFET with superior electrical performance and increased stability in air. The device's performance will then be compared to the state-of-the-art GFETs.

Chapter 5 will present the biosensing performance of the GFET from Chapter 4 towards early detection of heart failure. The biosensing performance will be compared to the state-of-the-art FET heart failure biosensors.

Chapter 6 will present additional sensing capabilities of the graphene-based materials and the GFETs towards gas sensing and COVID-19 biosensing, respectively.

Chapter 7 will conclude the thesis and present future avenues that could be further explored.

Chapter 8 will list the publications in journals and conferences.

1.3 Contributions

The laser ablation, characterization of materials, device fabrication, and result analysis were performed by I. Novodchuk. The electrical measurements throughout the thesis were performed in collaboration with M. Kayaharman. The gas sensing and MSS device fabrication and analysis described in Chapter 6 were performed by Dr. K. Mistry. The 2D nanorods project described in Chapter 7 was performed in collaboration with Dr. K. Mistry and Dr. K. Ibrahim.

Chapter 2
Graphene-based FET biosensors

2.1 Introduction

The structure of a GFET is similar to a metal-oxide-semiconductor FET (MOSFET) [24]. It is made up of a graphene-based channel between source and drain electrodes typically on a SiO_2/Si substrate [25]. The gate electrode could either be on top of the channel (separated by an oxide layer) or through the substrate, referred to as back-gated [26]. While the type of gate has an effect on the power consumption and the controllability of the FET, with top-gated devices needing lower power and providing better control [5], the main factors that determine the electrical performance are the channel material and its contact with the other components [27]. The following sub-sections will explore the state-of-the-art pristine graphene and graphene-based materials fabricated in recent years and their use in FET biosensor devices. The biosensing performance will be analyzed based on the transducer material and the electrical performance of the device.

2.1.1 Pristine graphene

Pristine graphene is another name for graphene in its pure form, i.e., a hexagonal network of carbon atoms [28]. Common fabrication processes of graphene include exfoliation and cleavage of graphite, chemical vapor deposition (CVD), and graphene epitaxy [8]. Single to few-layers graphene (FLG) sheets can be separated from the bulk graphite structure by exfoliation and cleavage, due to the weak Van der Waals forces between neighboring graphene sheets in the graphite. In this method, an adhesive tape is used to extract graphene from the graphite and deposit it onto a substrate [29]. While this process enables the exfoliation of high-quality graphene sheets as big as ~0.5 mm and with a charge carrier mobility of up to 12,000 $cm^2V^{-1}s^{-1}$ [29], it has several disadvantages. It is currently not possible to exfoliate graphene on a large-scale industrial level [13], it takes a long time, and the graphene's shape and location on the substrate cannot be controlled.

In contrast, the CVD growth of graphene is compatible with the industry fabrication standards and could be fabricated over large areas [30]. However, the graphene is fabricated on a metal substrate and transferred to the desired substrate by "a complex transfer procedure where some of the stamp material remains as a contaminate on the graphene surface and reduces its charge carrier mobility" [8]. Most reported CVD graphene have inferior charge carrier mobilities to exfoliated graphene, with the highest

values reaching 8,000 $cm^2V^{-1}s^{-1}$ at room temperature [31]. Epitaxial growth of graphene could be produced at a high quality and over large-areas, but the high temperatures required are not compatible with the industry standards [13].

Several of the highest reported charge carrier mobilities of the state-of-the-art graphene fabricated in the aforementioned methods are compared in Table 1 and Figure 1. As seen from the table and figure, the highest reported room temperature charge carrier mobilities were achieved for exfoliated graphene, while the lowest values were observed for epitaxial graphene. It is also important to mention that the reported I_{ON}/I_{OFF} ratios were very low (4-13), as expected for pristine graphene [32]. Lastly, for all three fabrication methods, there is a notable reduction in the charge carrier mobility with increased channel areas, as demonstrated in Figure 1. This observation is a great obstacle in fabricating large-area GFETs and is believed to be a direct result of the increased number of grain boundaries with increasing channel area [33]. This obstacle will be further discussed and addressed in Chapters 3 and 4.

Table 1 - A comparison between the room temperature electrical properties of the state-of-the-art pristine graphene fabricated by different methods.

Fabrication method	Charge carrier mobility ($cm^2V^{-1}s^{-1}$)	I_{ON}/I_{OFF}	Area (μm×μm)	Reference
Exfoliation	5700	~13	100×1000	[34]
	40000	-	0.75×2	[35]
	10000	-	180×230	[36]
CVD	900	~4	100×1000	[34]
	8000	~7	180×230	[36]
	5400	~5	250×250	[37]
Epitaxial	9000	-	-	[38]
	3200	-	100×600	[39]
	4700	-	5×5	[40]

While some astonishing progress has been made in increasing the quality and charge carrier mobility of pristine graphene, the low I_{ON}/I_{OFF} ratios are a great obstacle to numerous applications, including

biosensing applications [32]. This is one leading reason why graphene-based materials have been receiving much attention in the last several years.

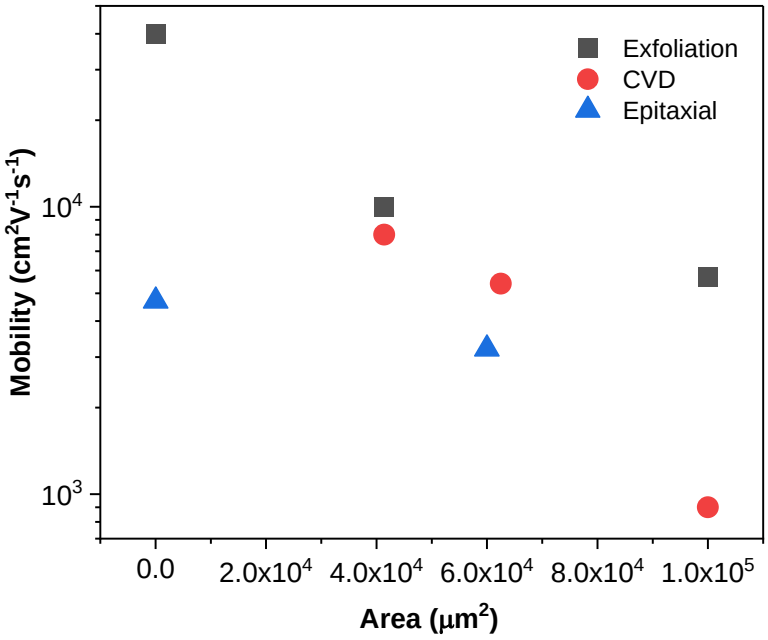

Figure 1 - A comparison between the room temperature charge carrier mobilities of several of the top-performing state-of-the-art pristine graphene fabricated in different methods.

2.1.2 Graphene-based materials

As several obstacles in using pristine graphene for electronic applications such as the high fabrication costs [22] and the low I_{ON}/I_{OFF} ratios [36] remain, alternative graphene-based materials are increasingly attracting research attention. These materials include GO and rGO which have the same carbon backbone structure as pristine graphene but with out-of-plane oxygen-based functional groups [41]. GO has high band gap (~5 eV) and is categorized as an insulator. Removing some of the oxygen functional groups restores the conductivity and structure of the GO towards that of graphene. The removal of some of the oxygen functional groups decreases the band gap and forms a semiconductor named rGO. Additional graphene-based materials include doped graphene [15], heterostructures [42], and graphene-based hybrids or composites [16]. In this sub-section, several of the top-performing state-of-the-art graphene-based materials will be compared based on their electrical properties and fabrication method.

Table 2 - A comparison between the room temperature electrical properties of the state-of-the-art graphene-based materials.

Material	Fabrication method	Charge carrier mobility ($cm^2V^{-1}s^{-1}$)	I_{ON}/I_{OFF}	Area (μm×μm)	Reference
rGO	Photothermal reduction	0.17	111	70×500	[43]
	Hydrazine reduction	~630	>500	200×2000	[44]
	Pulsed laser deposition	1600	-	-	[45]
	Pulsed laser deposition	5	-	100×100	[46]
N-doped rGO	Chemical reduction and doping	5	~1.5	20×20	[47]
N-doped graphene	CVD	520	-	-	[48]
MoO_3-doped graphene	MoO_3 flame doping	2700	7.5	0.5×10	[49]
MoS_2/graphene heterostructure	CVD	600	~100	3×5	[42]
h-BN/graphene heterostructure	CVD and exfoliation	100000	~150	2×2	[50]
	CVD	18000	~4	0.5×2	[51]
	Exfoliation	7000	~20	1×10	[17]
Graphene/Pt hybrid	CVD	1200	~3	10×100	[52]
rGO/TiO_2 composite	Chemical reduction	~4.5	~2	4×200	[53]
MEH-PPV[1]/PbS QDs[2]/ graphene hybrids	-	180	~5	100×2500	[54]

[1] MEH-PPV-poly [2-methoxy-5-(2´- ethylhexyloxy-p-phenylenevinylene)].
[2] QD- quantum dot

As seen in Table 2, there are different types of graphene-based materials with a large divergence in electrical properties. To get a better overview of the top-performing graphene-based materials, the data in Table 2 was plotted in Figure 2. Figure 2a shows the dependence of the mobility (light fill) and the I_{ON}/I_{OFF} ratio over the type of graphene-based material, while Figure 2b shows the mobility versus the I_{ON}/I_{OFF} ratio for the different types of graphene-based materials. Ideally, the desired material would have both high mobility and I_{ON}/I_{OFF} ratio, thus would be in the top right corner of Figure 2b. As seen from the figure, there is no clear candidate for an ideal type of graphene-based material, but the best performers are either from the rGO group or the heterostructure group, with h-BN/G heterostructures having the best overall electrical properties.

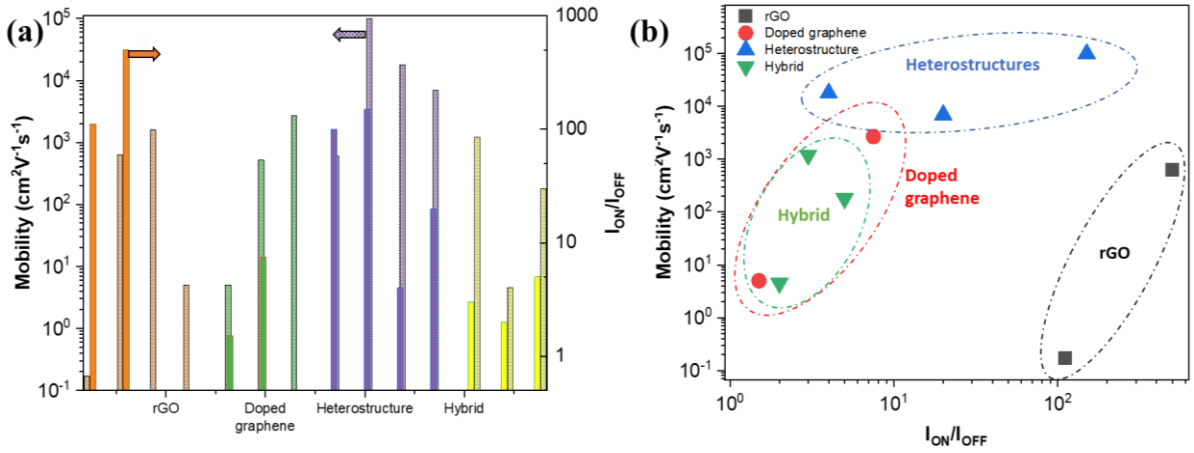

Figure 2 - A comparison between the electrical properties of the state-of-the-art graphene-based materials divided by group type. (a) Mobility (patterned) and I_{ON}/I_{OFF} ratio (solid fill) for different graphene-based types. (b) Mobility vs. I_{ON}/I_{OFF} ratio for different graphene-based types.

While GO and rGO materials can be cheaply produced [22], CVD fabrication of a wafer-scale h-BN is challenging [55]. For this reason, this thesis will employ monolayer GO solution and h-BN nanopowder as the starting materials for a novel graphene-based material with the goal to improve both mobility and I_{ON}/I_{OFF} ratio compared to the state-of-the-art.

2.2 State-of-the-art graphene-based FET biosensors

2.2.1 Working principle

In a GFET, a graphene-based channel is typically deposited between source and drain electrodes (S and D, respectively) on a doped silicon substrate separated by an oxide layer [8], as shown in Figure 3. A gate electrode is also needed for turning the device on and off by controlling the channel's conductivity, thus achieving the field effect [42]. The gate electrode could either be from the substrate (back-gate), from the top of the channel (top-gate), or through a solution (solution-gated or electrolyte-gated) [56], as demonstrated in Figure 3a-c, respectively. The voltage between the source and drain electrodes (V_{DS}) determines the direction of the current flow. A common drain current (I_{ds}) versus gate voltage (V_G) plot for GFET for a constant V_{DS} is shown in Figure 4a (reproduced with permission from [8]. ©2019 Elsevier). This plot is unique to GFET since depending on the V_G, it can either be an n-type or p-type device. This ambipolar behavior is a direct result from the symmetry between the valence and conductance bands [13]. The critical transition voltage between these two regions is defined as the Dirac point where the "OFF" current is achieved [57].

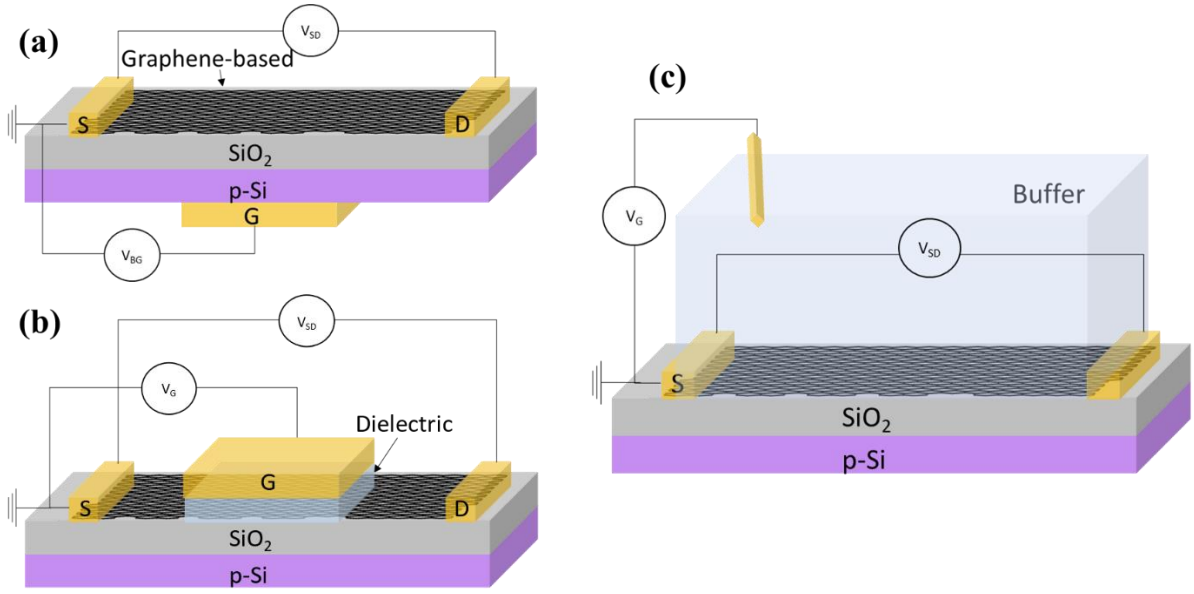

Figure 3 - A schematic of GFET working principle. (a) Back-gated (BG), (b) top-gated, and (c) solution-gated GFET.

In a GFET biosensor, the graphene-based channel is the transducer material, but it cannot distinguish between the target biomolecule and other charged molecules in its surroundings. Therefore, the GFET

needs to be functionalized with a bioreceptor that would capture the target analyte from the sample environment [19]. As discussed in [8], when constant V_{DS} and V_G are applied, the I_{ds} should be constant over time, as long as there is no change in the device's environment (such as temperature, humidity, chemicals present, etc.). If charged target biomolecules are introduced and captured by the bioreceptors (after a time known as "the detection time"), their charges will induce a change in the charge carrier concentration of the GFET channel to compensate for the additional charge. Consequently, the I_{ds} would change proportionally, as shown in Figure 4b (reproduced with permission from [8]. ©2019 Elsevier). In the case of an n-type channel, an attachment of a negatively charged target biomolecule would decrease the current, and vice-versa for a positively charged target [58]. Additionally, according to equation 1, the current (I_{ds}) is directly proportional to the magnitude of the electron mobility (μ_n) in the case of an n-type GFET [8]:

$$\boldsymbol{I_{ds} \approx \frac{en\mu_n wt}{L} V} \qquad (\mathbf{1})$$

Where e is the electron charge, n is the electron concentration, w, t, and L are the channel's width, thickness, and length, respectively, and V is the voltage. Thus, for the same device geometry, a channel with larger mobility will result in a larger sensing response. Figure 4c shows a different biosensing mechanism which is unique to GFETs. It is achieved by monitoring the change in the Dirac point, which is also a direct result from the change in the charge carrier concentration of the device.

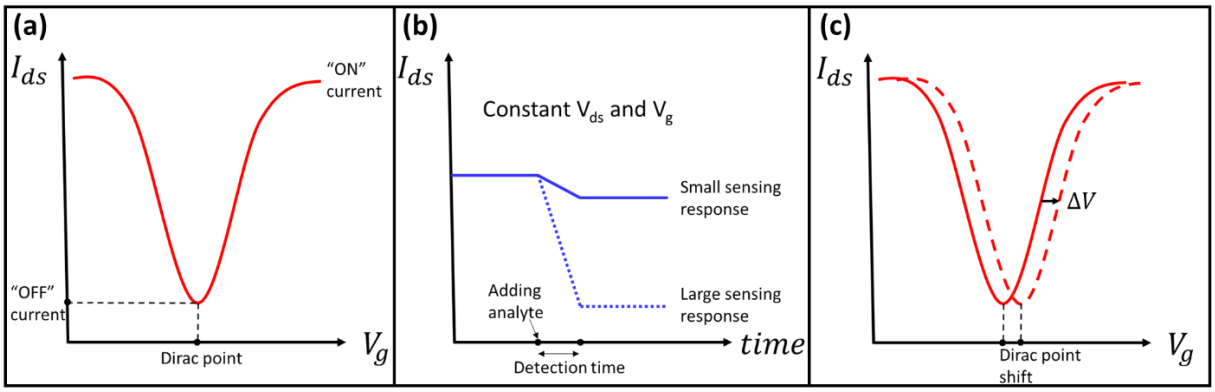

Figure 4 - Drain source current measurement (a) vs gate voltage and (b) vs time for graphene-based FET biosensor. The current changes in response to target biomarker attachment. (c) Similarly, the current vs gate voltage plot shifts in response to target biomarker attachment. Note: the current in plot (a) and (c) is in log scale (reproduced with permission from [8]. ©2019 Elsevier).

2.2.2 Bioreceptors

Bioreceptors play a key role in the success of the biosensor since their choice determines whether the device could capture the wanted target biomolecule inside a complex sample [19]. The bioreceptor should be able to interact only with the target analyte while "ignoring" all the surrounding molecules [59]. Some of the most studied bioreceptors include antibodies, aptamers, and complementary DNA (or probe DNA), as seen in Figure 5 (reproduced with permission from [8]. ©2019 Elsevier).

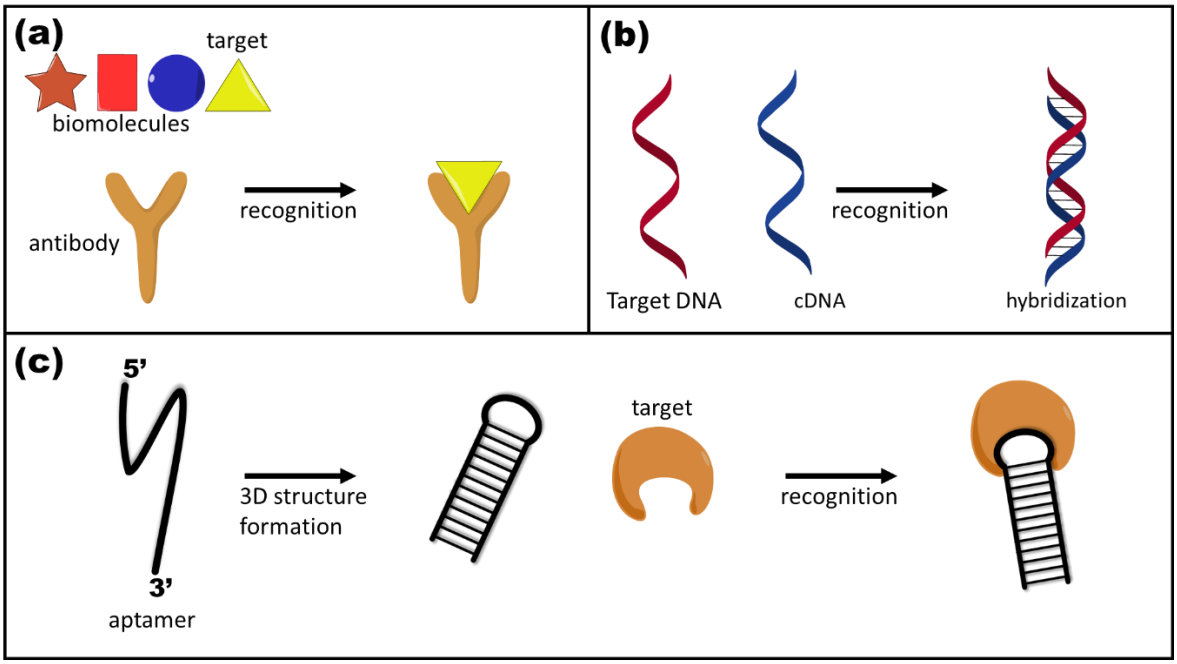

Figure 5 - Schematic mechanism of (a) a selective recognition reaction of an antibody with a target biomolecule in a bio-environment. (b) A recognition reaction of target DNA with cDNA resulting in a hybridization process. (c) An aptamer forming a three-dimensional (3D) structure and undergoing a recognition reaction with a target biomolecule (reproduced with permission from [8]. ©2019 Elsevier).

Antibodies are proteins with a "Y" structure produced by the body when it is exposed to a foreign compound [26]. A single-stranded DNA (ssDNA or probe DNA) can be designed to make a selective hybridization reaction with a complementary target ssDNA or RNA. Similarly, aptamers, which are single-stranded small oligonucleotides can specifically bind to different analyte types [60]. They often go through a three-dimensional (3D) conformation change before they can be used as the analyte anchoring component. Antibodies provide better specificity compared with aptamers and ssDNA, which can make non-specific electrostatic interactions [26]. Nonetheless, antibodies are large

molecules (above 10 nm in size), much larger than aptamers (1-3 nm) and ssDNA (~3.5 nm) [61]. The size of the bioreceptor is a very important aspect of FET biosensors. Beyond a certain length, called "the Debye screening length", the ions in the solution screen 63% of the recognition reaction between the biosensor and the target analyte, resulting in poor sensitivity [7]. The Debye screening length in blood is ~1.5 nm [62], therefore a minute bioreceptor is desired.

Circumventing the Debye screening effect [8] could be achieved by changing the bioreceptor, taking only a fraction of the bioreceptor (like using a fragmented antibody [52]), reducing the ionic strength of the sample's solution [63], or making changes to the GFET channel such as inserting structural stress, adding a curved morphology [7], or adding a permeable layer [64]. The latter two strategies will be explored in Chapters 5-6 of this thesis while reducing the ionic strength of the sample's solution will be explored in Chapter 6 of this thesis.

2.2.3 Structure and biosensing performance

This sub-section is aimed to examine the top performing GFET biosensors reported in recent years and to examine the challenges and opportunities the field faces today. Several aspects will be examined in detail: the device's structure and components, the LOD and the detection range, the detection medium, the target analyte, and the bioreceptor species, as seen in Table 3. Since the same GFET functionalized with different bioreceptors could theoretically be used to detect different biomarkers [8], this sub-section will not focus on a specific biomarker type.

DNA detection is targeted for several reasons, such as understanding biological reactions [65], and for disease diagnosis, prognosis, and assisting physicians with treatment plans [8]. Wang and Jia [65] reported a high-quality liquid exfoliated graphene (LEG) functionalized with a probe DNA through a Glutaraldehyde (GA) linker for the detection of target DNA in a buffer solution. They demonstrated the ability to functionalize amine-terminated DNA to the GA linker. The reported LOD was 10 fM with a large detection range of 1 fM- 10 nM spreading over 6 orders of magnitude. However, the biosensor's selectivity toward interfering species was not discussed. Gao et al. [66] used a GFET functionalized with an engineered hairpin probe DNA via 1-Pyrenebutanoic acid succinimidyl ester (PBASE) linker. The probe DNA enhanced target recycling and hybridization chain reaction which enhanced the sensing signal and the sensitivity of the device. They reported an LOD of 100 aM and a detection range of 100 aM-10 pM. Lastly, Chen et al. [67] used a MoS_2/graphene hybrid structure as the channel of their FET. The probe DNA was also functionalized through a PBASE linker, and the reported LOD and detection range were 100 aM and 100 aM-100 pM, respectively. They attributed their enhanced sensitivity to the

reduced Debye screening as a direct result of the hybrid structure. In addition, the authors reported enhanced selectivity by a factor of 0.5 and 24 compared to a single and 15-bases mismatched DNA, respectively.

Dysregulation of RNA and micro-RNA (miRNA) has been linked to many different diseases [8]. Thus, monitoring their levels can be used for diagnostic purposes. Hwang et al. [7] reported a crumpled graphene (CG) FET with the ability to detect miRNA with an LOD of 20 aM and a detection range of 20 aM-200 fM in serum and an LOD of 600 zM in buffer. They reported an astounding 10 orders of magnitude detection limit (600 zM-60 nM) in buffer. They attributed the enhanced sensitivity to the CG structure which increased the Debye screening length. Tian et al. [68] used a CVD-grown graphene FET functionalized with a probe DNA through a PBASE linker for the detection of RNA with an LOD of 0.1 fM and a range of 0.1-1000 fM. They used a buffer with low ionic strength (0.1x) in order to increase the Debye screening length. In a different paper [69], the same group reported the ability to enhance the LOD and detection range by changing the bioreceptor to Peptide Nucleic Acid (PNA) to 0.1 aM and 0.1 aM-1 pM, respectively. The group attributes the enhanced performance to the fact that unlike the probe DNA, the PNA is a neutral molecule thus reducing ionic interference compared to DNA. Additionally, the group demonstrated the device's ability to detect 0.1 aM RNA in serum, which is a noteworthy result.

Detection of small proteins could be very beneficial for disease diagnostics and prediction [70] or for food safety [71]. Yang et al. [70] used an FET with a graphene nanomesh (GNM) functionalized with an aptamer via a PBASE linker for the biosensing of human epidermal growth factor receptor 2 (HER2) cancer biomarker protein in a buffer solution. They reported an LOD of 0.6 fM and a detection range of 0.0001-10 ng/mL. They also demonstrated the ability to fabricate a flexible GNM FET biosensor and demonstrated signal enhancement compared with a graphene FET. Yeh et al. [72] used an FET with a graphene channel functionalized with antibodies through a PBASE linker for the biosensing of chondroitin sulfate proteoglycan 4 (CSPG4) cancer biomarker protein in a buffer solution with an LOD of 0.01 fM and a detection range of 0.01 fM -1 pM. The group attributes their great sensitivity to the enhanced graphene quality and electrical performance by the addition of self-assembled monolayers of Hexamethyldisilazane on the substrate surface. Lei et al. [73] used an rGO/Pt nanoparticles (NPs) hybrid to sense brain natriuretic peptide (BNP), a recognized heart failure (HF) protein, with a LOD and detection range of 100 fM and 0.1-1000 pM in buffer, respectively. They were also able to selectively detect 50-200 nM BNP concentrations in whole blood samples.

Around 500 million people have been infected by the hepatitis B (Hep-B) virus [74]. This virus can cause liver disease which has infected around one million people annually. For this reason, recent works have been published targeting Hep-B biosensing. Basu et al. [75] fabricated an rGO nanogrid structure using a nanoporous silicon oxide template. Their goal was to take advantage of the properties of graphene nanoribbons (GNRs) while keeping the fabrication process simple and avoiding rough edges and dangling bonds. They reported an LOD of 50 aM (but a narrow detection range) for a protein on the surface of Hep-B virus (Hep-B antigen). The bioreceptor used was a Hep-B antibody which was immobilized on the channel using N-(3-dimethylaminopropyl)-N′-ethylcarbodiimide hydrochloride (EDC)-N-hydroxysuccinimide (NHS) linkers. In a different work [76] the group reported the ability to use the biosensor for Hep-B detection in serum with an LOD of 0.1 fM and a range of 0.1 fM-1 pM.

Table 3 - State-of-the-art GFET biosensing platforms with enhanced LOD and detection range.

Transducer	Target	Bioreceptor	LOD (fM)	Detection range	Medium	Ref.
LEG/GA	DNA	Probe DNA	10	1 fM- 10 nM	Buffer	[65]
G[3]/PBASE	DNA	Probe DNA	0.1	100 aM-10 pM	Buffer	[66]
MoS_2/G hybrid	DNA	Probe DNA	0.01	10 aM to 100 pM	Buffer	[67]
G/PBASE	RNA	Probe DNA	0.1	0.1 fM-1 pM	Buffer	[68]
CG/PBASE	miRNA	Probe DNA	0.02	20 aM-200 fM	Biofluid	[7]
			0.0006	600 zM-60 nM	Buffer	
G/PBASE	RNA	PNA	0.0001	0.1 aM-1 pM	Buffer	[69]
GNM/PBASE	HER2	Aptamer	0.6	0.0001-10 ng/mL	Buffer	[70]
G/PBASE	CSPG4	Antibodies	0.01	0.01 fM -1 pM	Buffer	[72]
rGO/Pt NPs	BNP	Antibodies	100	100 fM-1 nM	Buffer	[73]
			$5x10^7$	50-200 nM	Blood	
rGO nanogrid/ EDC-NHS	Hep-B antigen	Antibodies	0.05	50 aM-10 PM	Buffer	[75]
G/PBASE	SARS-CoV-2 spike	Antibodies	1 fg/mL	1-1000 fg/mL	Buffer	[77]
			100 fg/mL	0.1-10 pg/mL	Mucus	
G/DAN[4]	H_2O_2	Cytochrome c	100	100 fM-100 pM	Buffer	[78]

[3] G- graphene
[4] DAN- 1,5-diaminonaphthalene

In the past year, another virus has been the focus of many different biosensing platforms. This is the coronavirus 2 (SARS-CoV-2) which causes COVID-19, especially since the World Health Organization (WHO) has classified the COVID-19 outbreak as a pandemic [77]. GFET is one of the solutions researchers target for highly sensitive point-of-care biosensor applications. Seo et al. [77] reported a GFET biosensing device for detecting SARS-CoV-2 in clinical samples. The channel was functionalized with a specific antibody against SARS-CoV-2 spike protein through a PBASE linker. They reported an LOD of 1 fg/mL in phosphate-buffered saline and 100 fg/mL in clinical transport medium. The selectivity of the biosensor was also tested against Middle East respiratory syndrome coronavirus (MERS-CoV) with 6 times higher detection signal towards the target.

Oxidative stress could be used to prognose many different diseases such as cancer and neurological disorders through monitoring the quantity of H_2O_2 molecules in bodily fluids [78]. Lee et al. demonstrated the ability to detect H_2O_2 in buffer with an LOD and detection range of 100 fM and 0.1-100 pM, respectively, using a graphene FET functionalized with a Cytochrome c protein through a 1,5-diaminonaphthalene linker. The device showed 10 times better LOD compared to the state-of-the-art with different FET transducers. The authors attributed the enhanced sensitivity to the increased surface charge from the Cytochrome c and H_2O_2 interaction.

2.2.4 Biosensing performance dependence on the electrical performance

In this sub-section, the biosensing performance of the state-of-the-art graphene-based biosensors discussed in the previous sub-section will be analyzed in terms of their electrical performance (i.e., charge carrier mobility and I_{ON}/I_{OFF} ratio), as summarized in Table 4. The expectation would be that FETs with higher mobilities and I_{ON}/I_{OFF} ratios could in turn have better sensitivity and low LOD [8]. However, no discussion was found for the effect of the electrical properties over the detection range, which is also a very important performance parameter.

As can be observed from Table 4, most of the state-of-the-art GFET biosensors exhibit extremely low LODs, as low as 0.6 aM, and high mobilities (mostly >1000 $cm^2V^{-1}s^{-1}$). However, the I_{ON}/I_{OFF} ratios are between 1-10, with three exceptions. An increased I_{ON}/I_{OFF} ratio showed no clear effect over the LOD and the detection range. The effect of the charge carrier mobility on the biosensing performance can be seen in Figure 6.

Table 4 - The biosensing performance and the electrical properties of the state-of-the-art GFET biosensors.

Transducer	Target	LOD (fM)	Detection range (orders of magnitude)	Mobility ($cm^2V^{-1}s^{-1}$)	I_{ON}/I_{OFF}	Ref.
LEG/GA	DNA	10	5	1200	~6.7	[65]
G/PBASE	DNA	0.1	5	2700	360	[66]
MoS_2/G /PBASE	DNA	0.01	7	~4300	~6	[67]
G/PBASE	RNA	0.1	4	~833	~1.3	[68]
CG/PASE	miRNA	0.0006	10	~4150	~3	[7]
G/PBASE	RNA	0.0001	7	~2000	~1.5	[69]
GNM/PBASE	HER2	0.6	5	~17	1000	[70]
G/PBASE	CSPG4	0.01	5	~2750	11	[72]
rGO nanogrid/ EDC-NHS	Hep-B antigen	0.05	7	~1300	~900	[75]
rGO/Pt NPs	BNP	100	4	~140	~1.4	[73]
G/DAN	H_2O_2	100	3	~3000	~1	[78]

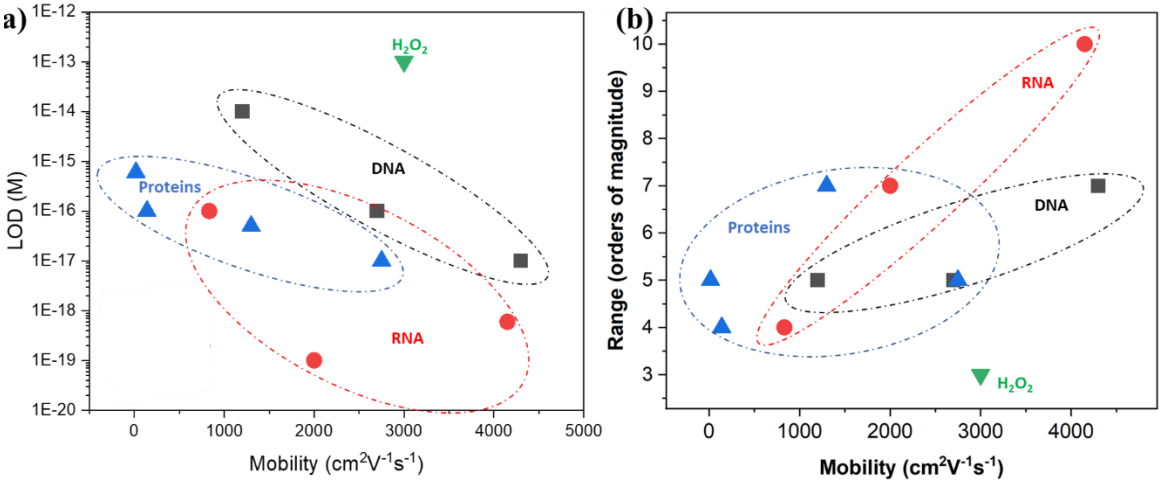

Figure 6 - The effect of the charge carrier mobility on the (a) LOD and (b) detection range of the state-of-the-art GFET biosensors.

As seen from Figure 6a, the LOD is enhanced with increasing charge carrier mobility for the same type of biosensor. Similarly, an increased mobility is associated with an increased detection range, as

seen in Figure 6b. These results confirm the demand for ultra-high charge carrier mobility materials. By roughly extrapolating the results, a GFET with a charge carrier mobility in the 10^5 $cm^2V^{-1}s^{-1}$ range would be theoretically able to detect DNA, RNA, and proteins with an LOD as low as 1 yM, 10 yM, and 1 aM, respectively. To put that in perspective, the biosensors would be able to detect a single DNA strand in one liter of buffer solution. Similarly, the detection ranges could reach up to 11, 20, and 8 for DNA, RNA, and protein, respectively. It is important to note that the above results are for buffer solution and are not applicable to real physiological samples.

2.3 Challenges and opportunities

In this section, the current challenges of the GFET biosensors will be discussed, and several approaches taken to address these challenges will be presented. First, as seen in [8], the I_{ON}/I_{OFF} ratio likely affects the LOD while not as dominant as the effect of the charge carrier mobility. Therefore, increasing the I_{ON}/I_{OFF} ratio is desirable for an enhanced LOD. Nonetheless, only a handful of GFET reported in recent years have ratios beyond 1000. Yang et al. [70] introduced high density 3 nm holes in the graphene structure which increased the I_{ON}/I_{OFF} ratio up to 1000. Deformation of graphene also increases the I_{ON}/I_{OFF} ratio up to 1000 for bilayer graphene [79]. Chen et al. [44] used rGO as the channel material and reported an I_{ON}/I_{OFF} ratio above 500. A heterostructure of graphene and MoS_2 with an h-BN dielectric was shown to have an extremely high I_{ON}/I_{OFF} ratio up to 10^8 [18]. Theoretically, increasing the channel's charge carrier mobility and the band gap would increase the I_{ON} and decrease the I_{OFF}, respectively [13].

Second, the importance of increasing the charge carrier mobility of the GFET was already covered, however, only a handful of works showed values exceeding 2000 $cm^2V^{-1}s^{-1}$ which is 2 orders of magnitude lower than the theoretical value [10]. Yeh et al. [72] were able to enhance the mobility to ~2750 $cm^2V^{-1}s^{-1}$ by using a Hexamethyldisilazane buffer layer between the graphene and the substrate. A different approach was to deform the graphene which increased its mobility to ~4150 $cm^2V^{-1}s^{-1}$ [7]. Tian et al. [67] used a heterostructure of graphene and MoS_2 with a charge carrier mobility of ~4300 $cm^2V^{-1}s^{-1}$.

Third, for the biosensor to be effective, the recognition reaction between the bioreceptor and the analyte must occur within the Debye screening length [7]. However, only a small number of the state-of-the-art GFET used small bioreceptors, such as aptamers [70] or PNA (1.5-2.2 nm [80]) [69]. Other groups used different strategies to increase the Debye screening length, such as using buffers with low

ionic strength [7], [68]. However, future work should be done to show the usefulness of such biosensors in real physiological samples. Other strategies to increase the Debye screening length included the deformation of the graphene channel [7], using hybrid structures [67], or using a channel with a permeable layer [64].

Lastly, since graphene is a hydrophobic material [8], bioreceptors are commonly functionalized through linkers. The most used linker is PBASE [66], however some groups used GA [65], DAN [78], EDC-NHS [75], or NPs [73]. However, the linker adds to the total length of the bioreceptor, thus contributing to the Debye screening [8].

2.4 Summary

In conclusion, graphene and graphene-based materials show great promise for FET biosensors, due to their extremely high theoretical charge carrier mobility. However, the fabrication of GFETs with high mobility is challenging. In addition, the short Debye screening length and low I_{ON}/I_{OFF} ratio in GFETs are also two important limiting factors for biosensing performance parameters, such as LOD and detection range. Analysis of the state-of-the-art GFET revealed enhanced mobility and I_{ON}/I_{OFF} values for graphene heterostructures and rGO materials.

GFETs biosensors reported in recent years were able to reach mobilities of up to ~4300 $cm^2V^{-1}s^{-1}$ and I_{ON}/I_{OFF} ratios up to 1000. LODs as little as 0.6 aM and detection ranges of up to 10 orders of magnitude were also reported. Analysis of the electrical and biosensing performance revealed improved LOD and detection range for GFETs with higher charge carrier mobility. However, most results were reported for buffer solutions and not for real physiological samples.

Several approaches were made for enhanced biosensing performance, with the most promising electrical enhancement results for heterostructures of graphene and h-BN or MoS_2. Other successful strategies for increasing the Debye screening length included the addition of curved or permeable surfaces. Lastly, all the GFETs reported in recent years used some sort of linker for bioreceptor immobilization, thus increasing the overall bioreceptor length. Therefore, a graphene-based material that does not require a linker is attractive for further investigation.

Chapter 3

B/N co-doped reduced graphene oxide nanoflakes solution

3.1 Introduction

Since 2004, when pristine graphene was first discovered by Novoselov and Geim [81], numerous graphene-based materials have been developed and listed into different categories, including zero-dimensional (0D, such as QDs [23]), one-dimensional (1D, such as nanoribbons [82]), 2D (such as nanoflakes [83]), and 3D (such as graphene hybrids [84] and gels [85]). The common graphene-based structures divided into different categories are schematically presented in Figure 7. Specifically, the incorporation of boron and nitrogen in graphene-based materials has gained interest because of their ability to introduce a bandgap and enhance the semiconducting properties of graphene [86], reduce substrate effects, decrease noise, increase room temperature mobility [17], increase electrical conductivity [87], and increase the chemical reactivity [88]. As a result, structures such as hybrid structures [86], heterostructures [17], and co-doped structures [87] of graphene and BN have been increasingly reported.

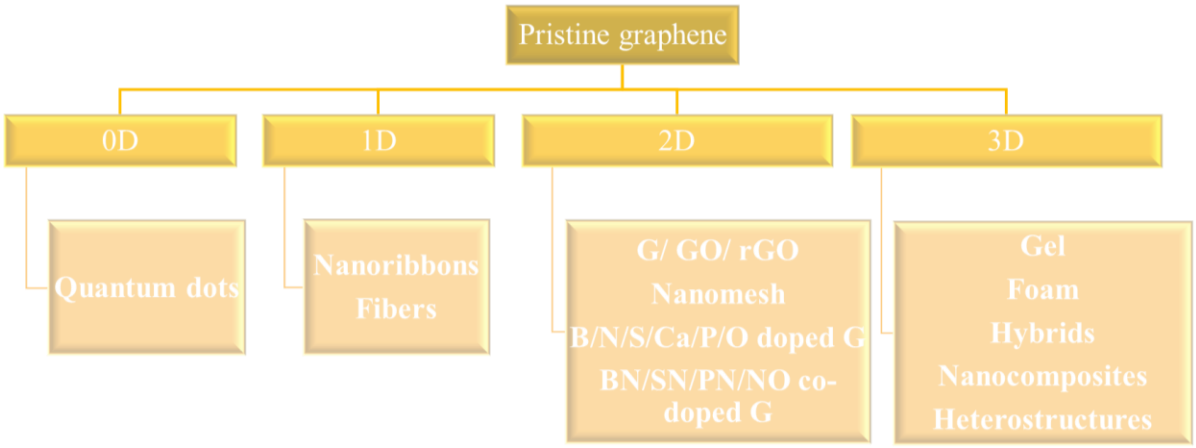

Figure 7 - Common graphene-based materials divided into structural categories.

Numerous processes have been proposed for the incorporation of boron and nitrogen in graphene. Several of the reported processes include pyrolysis [89], CVD [88],[90], thermal treatment [91], thermal annealing [92], microwave-hydrothermal method [93], and submerged liquid plasma exfoliation [94]. Nonetheless, challenges such as controlling the doping concentration and doping sites, and preventing stacking of sheets, while making the process scalable, quick, and without using harsh chemicals still remain [95].

This chapter will present the fabrication process of a 2D B/N co-doped reduced graphene oxide nanoflakes solution from h-BN nanopowder and GO nanoflakes solution via a laser ablation process, as reported in [95]. This process allows a quick and controllable fabrication from non-hazardous precursor materials.

3.2 Synthesis method

A Ti:Sapphire regenerative amplifier, with an operating wavelength of 800 nm, pulse duration of 35 fs, and repetition rate of 1 kHz was used in all laser ablation processes. The extremely short pulse duration of the laser does not cause thermal heating in the material, since it is much shorter than "the electron-phonon thermal process" [23]. Instead, it transfers the energy to the electrons, thus forming ionized atomic and molecular fragments by a process called "Coulomb explosion" [96]. The laser beam was focused through a lens (f=50 mm) with the focal waist located approximately 2 mm below the air/solution interface, as schematically presented in Figure 8a (reproduced with permission from [95]. ©2019 Elsevier). A 0.124 mg/ml solution of h-BN ultrafine powder (Graphene Supermarket) in 50:50 DI water:ethanol was ablated by a focused (f=50mm) laser beam for 70 min at an average pulse power of 2 W, followed by centrifuge process to extract 0.05 mg/ml h-BN quantum dot (BNQD) solution, as presented in Figure 8 b and c, respectively. A 0.5 mg/ml GO solution in DI (Graphene Supermarket) was mixed with BNQD solution at different vol% (0%, 5%, 15%, and 30% BNQD) to form GO, 5%BN-95%GO, 15%BN-85%GO, and 30%BN-70%GO, respectively. These solutions were ablated for 1 hour at an average pulse power of 1 W, and the ablated solutions were denoted as rGO, 5%BN-95%rGO, 15%BN-85%rGO, and 30%BN-70%rGO, respectively (also referred to as BN-rGO in general).

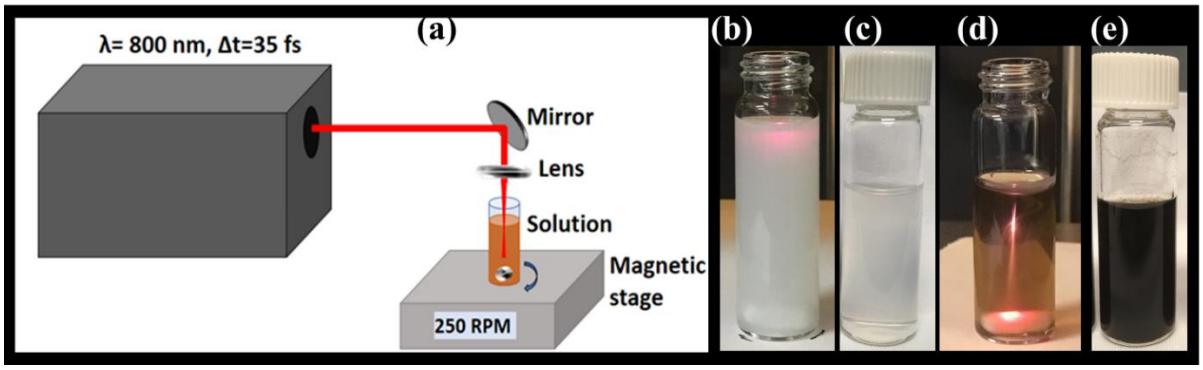

Figure 8 - (a) Schematics of the laser ablation setup (reproduced with permission from [95]**. ©2019 Elsevier). (b) and (c) digital images of BN and BNQD solutions (during and after laser**

ablation), respectively. (d) and (e) digital images of GO and rGO solutions (during and after laser ablation), respectively.

3.3 Characterization

3.3.1 UV-Vis absorbance

The most simple crude estimate of the reduction process of a GO solution is a visual examination of the solution color, where a light-brown GO solution changes to a dark-brown or black colored rGO solution [97], as can be evident from Figure 8d-e. While this estimate is a very effective indication of reduction, it is not a good indication of the chemistry and structure of the rGO nanoflakes. For this reason, often a combination of characterization techniques is used.

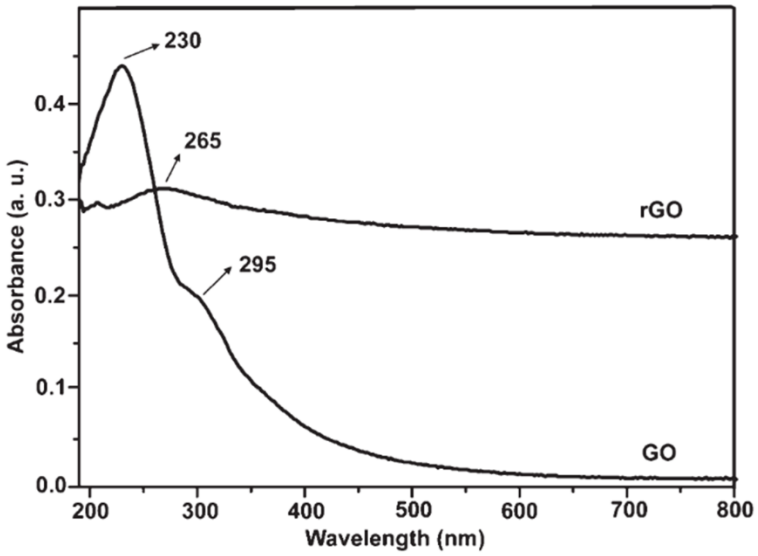

Figure 9 - UV-Vis absorbance spectrum of GO and rGO solutions (reproduced with permission from [98]**. ©2012 RSC).**

UV-Vis spectroscopy is commonly used to determine the degree of reduction and to estimate the bandgap of the material [41]. A common UV-Vis absorbance spectrum of GO and rGO solutions is presented in Figure 9 (reproduced with permission from [98]. ©2012 RSC). The absorbance plot contains two features of interest: a peak around 230 nm and a shoulder around 300 nm corresponding to π–π* in-plane C-C transitions and n–π* out-of-plane C=O transitions, respectively [98]. When reduction occurs, the n–π* shoulder disappears, and the π–π* absorption band shifts to higher

wavelengths, while the incorporation of B and N dopant atoms results in a shift towards lower wavelengths [95].

Consequently, UV-Vis absorbance analysis using a UV-2501PC spectrometer (Shimadzu Corporation) of the BN-rGO solutions revealed [95]:

1- the successful reduction of all solutions by the laser ablation process,

2- increased reduction with increasing BN concentration,

3- increased doping with increased BN concentration, and

4- increased bandgap with increased BN concentration.

3.3.2 Raman spectroscopy

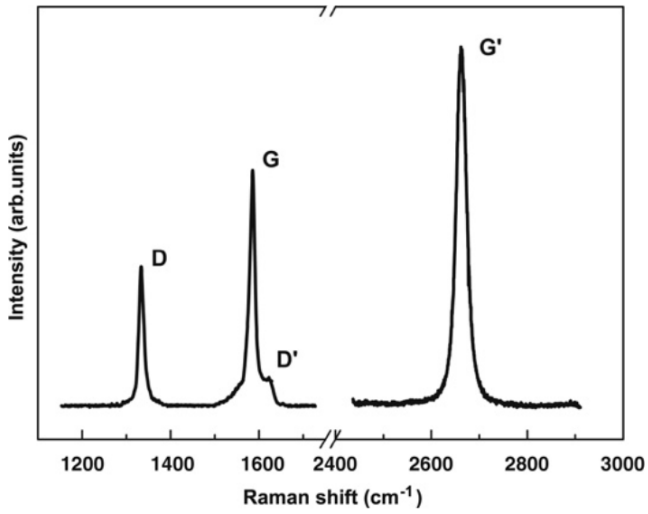

Figure 10 - Common Raman spectroscopy spectrum features of graphene-based materials (reproduced with permission from [100]**. ©2009 Elsevier).**

Other than UV-Vis absorbance, Raman spectroscopy is an additional qualitative characterization technique used for graphene analysis [99]. Graphene-based materials have several common features in the Raman spectrum, denoted as D, G, and G' (or 2D) peaks, as shown in Figure 10 (reproduced with permission from [100]. ©2009 Elsevier). The G band (at ~1580 cm^{-1} for 513 laser excitation) corresponds to the bond stretching of all sp^2 C-C atoms [101], while the D band (at ~1350 cm^{-1} for 513 laser excitation) corresponds to sp^2 atoms breathing mode [102] and the G' band (at ~2700 cm^{-1} for 513

laser excitation) corresponds to structural phonons. Lastly, the less common D' band (at ~1620 cm^{-1} for 513 laser excitation) corresponds to randomly distributed impurities.

Table 5 – A summary of the effect of graphene structural and electrical changes over the Raman spectrum.

	Increased intensity	Decreased intensity	Upshift	Downshift
G band	- Longer sp^2 domains [103]. - Increase in number of layers [104].	- Decrease in number of layers [104].	- Intrinsic h and e doping [101]. - Longer sp^2 domains [105].	- Shorter sp^2 domains [105]. - Compressive stress / different lattice constants [106]. - Increased extrinsic doping [104],[107].
D band	- Increased disorder [101]. - More defects [108].	- Decreased disorder [101].	- More oxygen functional groups [105].	- Less oxygen functional groups [105].
G' band	- Decreased e concentration [104].	- Increased e concentration [104].	- Increased e doping [104].	- Increased h doping [104]. - Increased compression strain [104].
D/G ratio	- Increased disorder [101]. - Decrease in number of layers [104]. - Decrease in the average interdefect distance [101].	- Restored conjugation [109]. - Increased doping [107]. - Increase in number of layers [104]. - Increase in the average interdefect distance [101].	-	-
G'/G ratio	- Increased n-type doping [95]. - Decrease in number of layers [104].	- Increased p-type doping [95]. - Increase in number of layers [104].	-	-

Table 5 Summarizes the effect of changes to the graphene structure and electrical properties over the Raman spectrum, namely the band's locations and intensities. For the purpose of this thesis, the band

intensity refers to the integrated peak intensity [104] and does not refer to the value at the band peak. An improved sp^2 structure would be reflected by an upshift in G band and an increase in its intensity [105],[103], and a decrease in I_D/I_G (intensity ratios between D and G bands, respectively) [109]. Similarly, an increase in the average interdefect distance [101] would be reflected by a decrease in I_D/I_G, and increased disorder and defect density would be reflected by an increase in D band intensity [101]. An increase in the number of graphene layers would result in an increased G band intensity and a decrease in I_D/I_G [104]. An increase in compression stress would result in a downshift in the G [106] and G' [104] bands. Lastly, doping would have different effects over the spectrum. An increase in intrinsic and extrinsic doping would translate to a G band upshift [101] and downshift [104],[107], respectively, while the type of doping could be monitored by the G' band intensity and shift direction [104].

A series of thin film were drop-casted onto a Si substrate from the GO, rGO, and BN-rGO solutions and dried overnight at room ambient. The analysis of the Raman spectra of the thin films is presented in Table 6 (reproduced with permission from [95]. ©2019 Elsevier).

Table 6 - D, G, and 2D Raman peak position and I_D/I_G and I_{2D}/I_G intensity ratios of drop-casted GO, rGO and BN-rGO nanoflakes. The excitation wavelength and incident laser power were fixed at 632.8 nm and 10.55 mW/cm2. Reproduced with permission from [95]**. ©2019 Elsevier.**

	D (cm^{-1})	**G (cm^{-1})**	**2D (cm^{-1})**	**I_D/I_G**	**I_{2D}/I_G**
30%BN-70%rGO	1331	1581	2641	2.17	0.041
15%BN-85%rGO	1332	1579	2671	2.41	0.043
5%BN-95%rGO	1337	1585	2676	2.17	0.055
rGO	1338	1585	2673	2.13	0.06
GO	1341	1586	2676	1.78	0.043

Based on Table 5 and Table 6, the laser ablated BN-rGO thin films (deposited on Si substrates) were analyzed using a Horiba HR800 Spectrometer equipped with a 532 nm excitation source, and the results revealed [95]:

(1) reduction of GO to rGO by femtosecond laser irradiation,

(2) formation of defect sites (e.g., vacancies and radicals) reducing the average interdefect distance,

(3) increased stress with increasing BN vol%, and stress relaxation for 30%BN-70%rGO, and

(4) increased p-type doping with increased BN vol%.

3.3.3 XPS spectroscopy

X-ray photo-electron spectroscopy (XPS) is a useful tool for quantitative composition analysis of a graphene-based thin film [110]. The XPS analysis of C1s, B1s, and N1s bands of GO, rGO, and BN-rGO nanoflakes are presented in Figure 11 and Figure 12, respectively (reproduced with permission from [95]. ©2019 Elsevier).

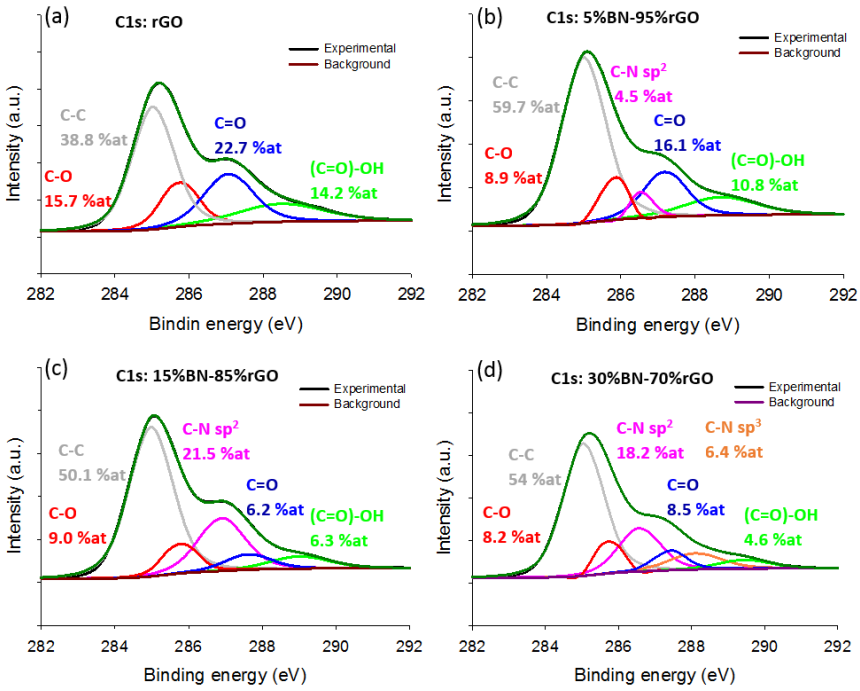

Figure 11 - C1s XPS spectrum and at% of each molecular bond in (a) rGO, (b) 5%BN-95%rGO, (c) 15%BN-85rGO, and (d) 30%BN-70%rGO thin films. Reproduced with permission from [95]**. ©2019 Elsevier.**

As seen in Table 7, Figure 11, and Figure 12, the XPS analysis of C1s, N1s, and B1s transitions in the GO, rGO, and BN-rGO samples has revealed [95]:

(1) reduction of GO to rGO by femtosecond laser irradiation (the amount of C-O bonds decreased by 33.3 at% from GO to rGO, whilst the amount of C=O and COOH bonds increased by 14 at%, and 10.6 at%, respectively),

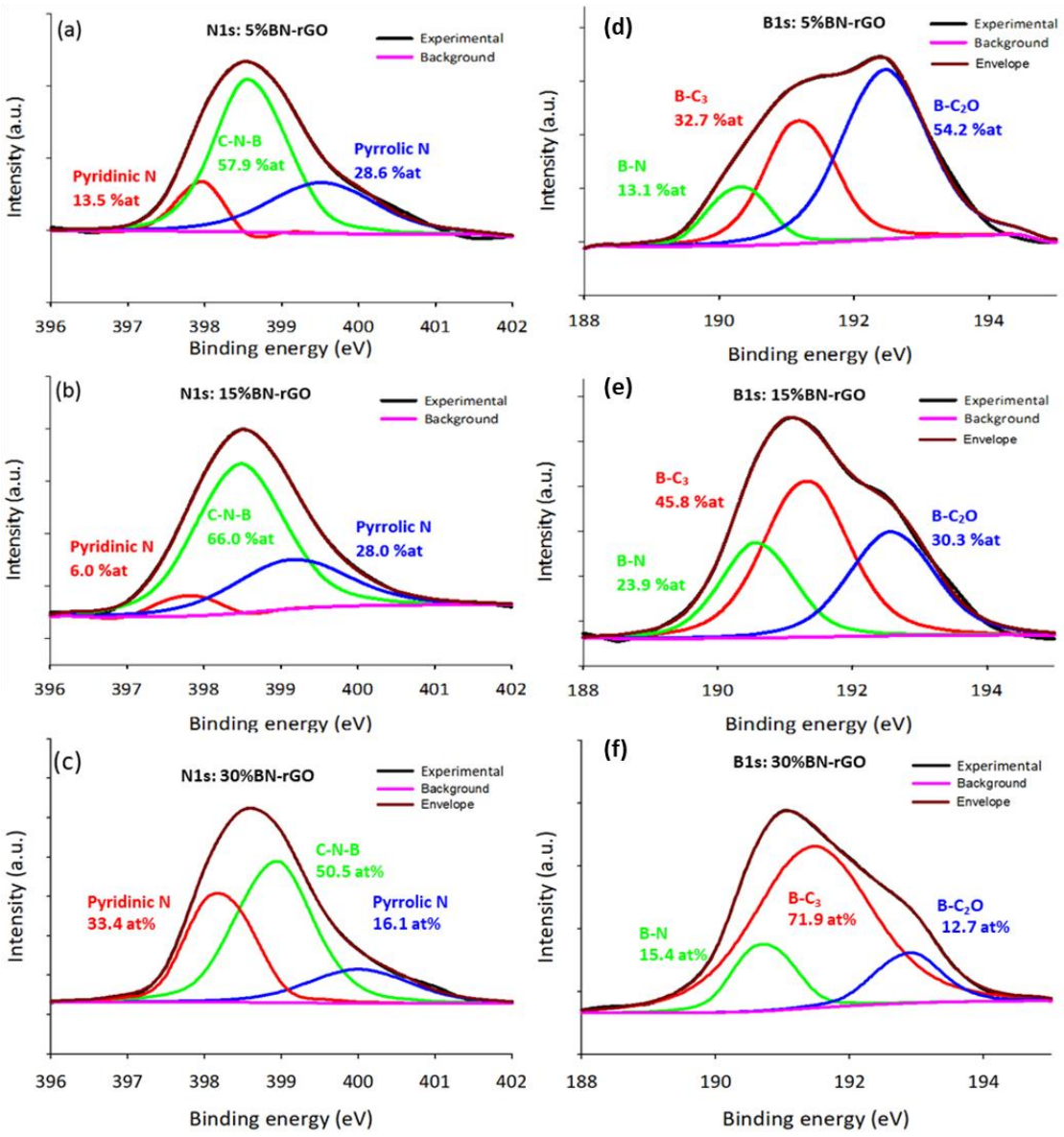

Figure 12 - N1s XPS spectrum and at% of each molecular bond in (a) 5%BN-95%rGO, (b) 15%BN-85rGO, and (c) 30%BN-70%rGO thin films. B1s XPS spectrum and at% of each molecular bond in (d) 5%BN-95%rGO, (e) 15%BN-85rGO, and (f) 30%BN-70%rGO thin films. Reproduced with permission from [95]**. ©2019 Elsevier.**

(2) increased reduction with an increasing BN vol% in the solutions,

(3) Pyridinic N is more energetically favorable than Pyrrolic N for increased BN vol% samples,

(4) BC_3 is more prominent than BC_2O for increased BN vol% samples, and

(5) formation of sp^3 CN bonds for high BN concentrations (30 vol%).

Table 7 - XPS composition analysis of GO, rGO, and BN-rGO samples.

Transition	Bond type	Composition (at%)				
		GO	rGO	5%BN-95%rGO	15%BN-85%rGO	30%BN-70%rGO
C1s	C-C	38.8	47.5	59.7	50.1	54
	C=O	56	22.7	16.1	6.2	8.5
	COOH	3.5	14.1	10.8	6.3	4.6
	C-O	1.7	15.7	8.9	9	8.2
	C-N sp^2	0	0	4.5	21.5	18.2
	C-N sp^3			0	0	6.4
N1s	C-N-B	0	0	57.9	66	50.5
	Pyrrolic N			28.6	28	16.1
	Pyridinic N			13.5	6	33.4
B1s	B-N	0	0	13.1	23.9	15.4
	B-C_3			32.7	45.8	71.9
	B-C_2O			54.2	30.3	12.7

Additionally, an XPS survey (using Thermo ESCALAB 250 with an unmonochromatic AlKa X-ray source and incident energy of 1486.6 eV) revealed that increasing BN concentration in the precursor solution translated into higher doping percentages. From 0 at% N in GO and rGO, the N doping increased to 1.8 at%, 3.1 at%, and 4.1 at% for 5%BN-95%rGO, 15%BN-85%rGO, and 30%BN-70%rGO, respectively. Similarly, 0 at% B in GO and rGO increased to 3.4 at%, 4.1 at%, and 5.9 at% B-doping for 5%BN-95%rGO, 15%BN-85%rGO, and 30%BN-70%rGO, respectively, confirming the dominance of p-type doping observed by the Raman spectrum analysis.

The XPS results revealed several advantages to the laser ablation fabrication method. First, the ability to co-dope the GO nanoflakes while simultaneously reducing them to rGO in a relatively quick process. Second, the ability to control the doping amount, while avoiding the use of harsh chemicals. Finally, while it is common for the GO nanoflake size to decrease during the reduction process [111], the

nanoflake sizes remained well above 1 µm for all BN-rGO samples (2.3-2.7 µm on average compared with an average GO nanoflake size of 3.2 µm).

Several groups reported the ability to simultaneously reduce GO and co-dope it with B and N atoms. Mannan et al. [112] reported the ability to produce B and N co-doped rGO from GO and tris(dimethylamino)borane via a hydrothermal synthesis process, however, the process demanded elevated temperatures of 200-400 ºC for 2-4 hours and drying at 60 ºC overnight, producing B and N doping of up to 2.3 at% and 4.12 at%, respectively. In a different work, Umrao et al. [87] reported the fabrication of B and N co-doped rGO from ammonia (which is highly toxic), boric acid , and GO solutions via a microwave-assisted process. The group reported a relatively long fabrication process (>8 hr at 60-80 ºC), producing B and N doping of up to 1.03 at% and 0.5 at%, respectively. Lastly, Kang et al. [111] heated a GO solution mixed with ammonia borane at 80 °C for 6 h to form B and N co-doped rGO, with B and N doping of up to 2.3 at% and 0.8 at%, respectively, and a nanoflake size below 1 µm.

3.3.4 HRTEM

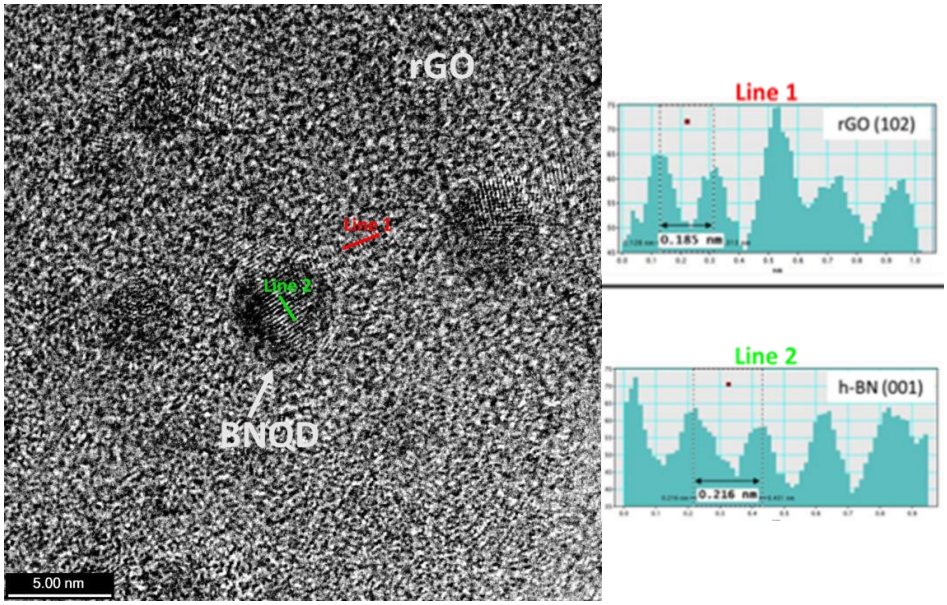

Figure 13 - HRTEM image of 30%BN-70%rGO, indicating the regions containing a BNQD and rGO nanoflake. The d spacing measured from line 1 and 2 was 0.185nm and 0.215nm, corresponding to (102) plane in rGO and (001) plane in h-BN, respectively. Reproduced with permission from [95]**. ©2019 Elsevier.**

High-resolution transmission electron microscopy (HRTEM) studies of BN-rGO are challenging for several reasons. First, observing GO requires very high electron beam acceleration voltages (above 50 kV) which quickly degrade the sample [113]. Second, GO contains many surface contaminants (compared to graphene) which "mask the atomic structure", making it difficult to observe the sp^2 structure. Lastly, B, C, and N are neighboring atoms in the periodic table, which means they have very similar atom sizes. While these similarities make B and N very compatible as dopant atoms in graphene [114], it hinders the ability to observe the dopants in the graphene structure. In addition, distinguishing between BN and graphene structures could also be very challenging, since the lattice mismatch is a mere ~1.7% [51].

With the above characterization obstacles in mind, HRTEM analysis of the BN-rGO samples was still used to characterize BN domains from rGO domains (due to the high order of the BN atoms), as seen in Figure 13 (reproduced with permission from [95]. ©2019 Elsevier). The HRTEM analysis revealed that the BN domains were approximately circular with a diameter of ~5 nm and a plane direction of (001), while the plane direction of the rGO was (102).

3.3.5 Other characterization

Optic microscope, which offers a non-destructive characterization, was recognized as a very helpful tool to qualitatively analyze the thickness, size, and shape of graphene-based materials. It can be achieved when the graphene is deposited on a Si substrate with a specific oxide thickness (285-300 nm) [115]. In addition, it was discovered that a GO monolayer offers a lower contrast compared to an rGO monolayer, providing an additional indication of a successful reduction [116]. As seen in Figure 14, there is a clear difference in contrast between the GO (a-b) and the rGO and BN-rGO (c and d, respectively) samples. This difference could either mean a change in nanoflake thickness or a reduction of the GO [116]. AFM analysis revealed no change in nanoflake thickness following the laser ablation process [95], confirming a successful GO reduction by the laser ablation process, as was discussed in the previous sub-sections.

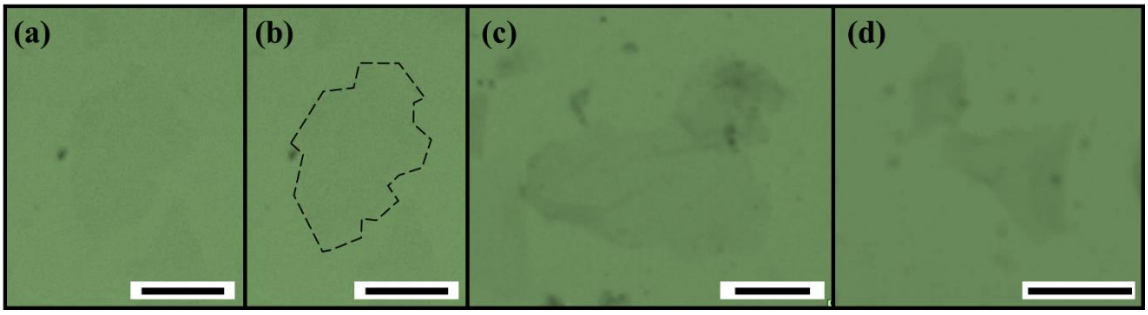

Figure 14 - Optic microscope image of graphene-based nanoflakes on 285-nm-thick silicon dioxide/ Si substrates with a 5 µm scale. GO (a) without and (b) with dashed-line indication. (c) rGO and (d) BN-rGO.

3.3.6 Device fabrication

3.3.7 Thin films deposition experiments

The preferred method of deposition that was chosen in this thesis was drop-casting, since spin-coating requires solutions with high viscosity [117]. First, a series of 285-nm-thick SiO_2/p-Si substrates were cleaned in an ultrasonic bath using Acetone, IPA, and DI water, followed by air drying, and an APTES treatment [118]. The APTES treatment was shown to enhance the wettability (and the spreading) of the graphene-based solutions on the substrates, as was measured by the change in contact angle from ~67° to ~52° prior and post APTES treatment, respectively.

3.3.7.1 Drop-casted films from diluted solutions

The graphene-based solutions (GO and 30%BN-70%rGO) were diluted using DI water to the following concentrations: 0.5, 0.25, 0.15, 0.1, and 0.05 g/L. The solutions were left in an ultrasonic bath for 1 hr and drop-casted onto the APTES-treated substrates and left to dry overnight at room temperature.

The samples were studied using Raman spectroscopy to understand the short-term (within several days) effect of the dilution on the oxygen content of the films. The results are presented in Figure 15 and Table 8. As can be observed, the ratio between the D and G peaks slightly changes for the GO samples, but within a 2% error (the average ratio is 1.21±0.023). Similarly, the ratio between the D and G peaks of the 30%BN-70%rGO samples changed within a 0.5% error (the average ratio is 1.36±0.006). Moreover, as indicated by the dashed lines in Figure 15, there is no D or G peak shift for both GO and 30%BN-70%rGO samples. Based on the Raman spectra analysis, it was concluded that the oxygen content in the films was not affected by the dilution of the GO solution.

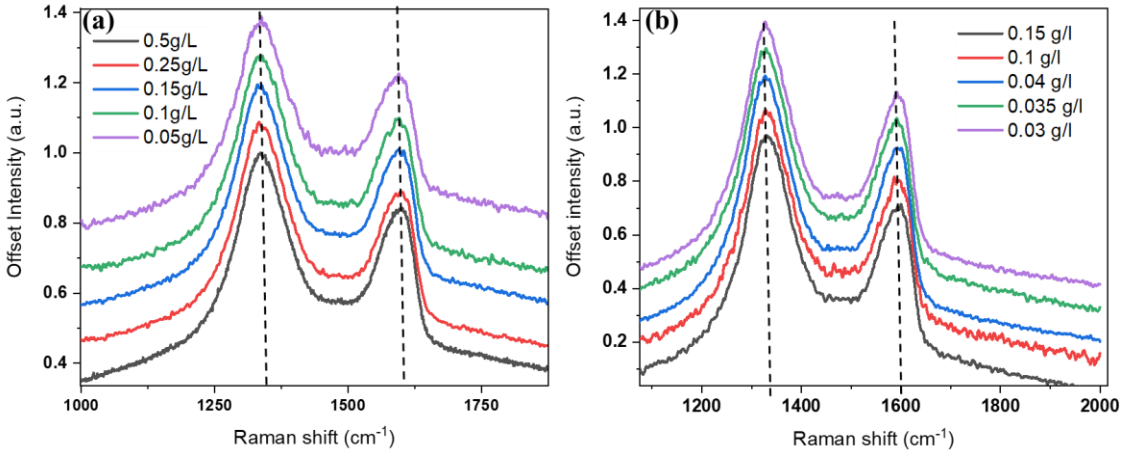

Figure 15 - Raman spectra of (a) GO and (b) 30%BN-70%rGO thin film deposited from different concentration solutions.

Table 8 - Analysis of Raman spectra of GO thin film deposited from different concentration solutions.

GO				30%BN-70% rGO			
concentration (g/L)	**I_D (a.u.)**	**I_G (a.u.)**	**I_D/I_G**	**concentration (g/L)**	**I_D (a.u.)**	**I_G (a.u.)**	**I_D/I_G**
0.5	1.0	0.85	1.19	0.15	0.976	0.713	1.37
0.25	0.99	0.80	1.24	0.1	0.966	0.7144	1.35
0.15	0.99	0.81	1.23	0.04	0.994	0.732	1.36
0.1	0.98	0.80	1.23	0.035	0.996	0.734	1.36
0.05	0.98	0.82	1.19	0.03	0.986	0.727	1.36

A series of thin films were deposited onto cleaned substrates (as discussed earlier), and the thickness of each sample was evaluated using a Dektak profilometer. The film profile and thickness dependence on the solution concentration for GO and 30%BN-70%rGO are presented in Figure 16 a and b, respectively. Equations 2 and 3 show the dependence of the drop-casted film thickness (t) on the GO and 30%BN-70%rGO solution concentration (C), with an R-square fit of 0.976 and 0.98, respectively. Theoretically, when C is approaching 0, the thickness will not approach 0, but rather would approach 0 when the concentration approaches 0.0307 and 0.03 for GO and 30%BN-70%rGO solutions, respectively. This phenomenon could be explained by the formation of a thick outer ring (or coffee-

ring [119]) for drop-casted samples, as seen in Figure 16a. At low concentrations, instead of a continuous film, the graphene-based nanoflakes would form non-continuous structures, as shown in Figure 16c. In practice, the lowest thickness (~80 nm) of a continuous film was observed for 0.05 g/L GO, however, at that thickness, the material should behave as a bulk graphite oxide and not as the desired few-layer GO [100].

$$t_{GO} = 123.6 ln C_{GO} + 433.2 \quad (2)$$

$$t_{70\%BN-30\%rGO} = 173.7 ln C_{30\%BN-70\%GO} + 605.2 \quad (3)$$

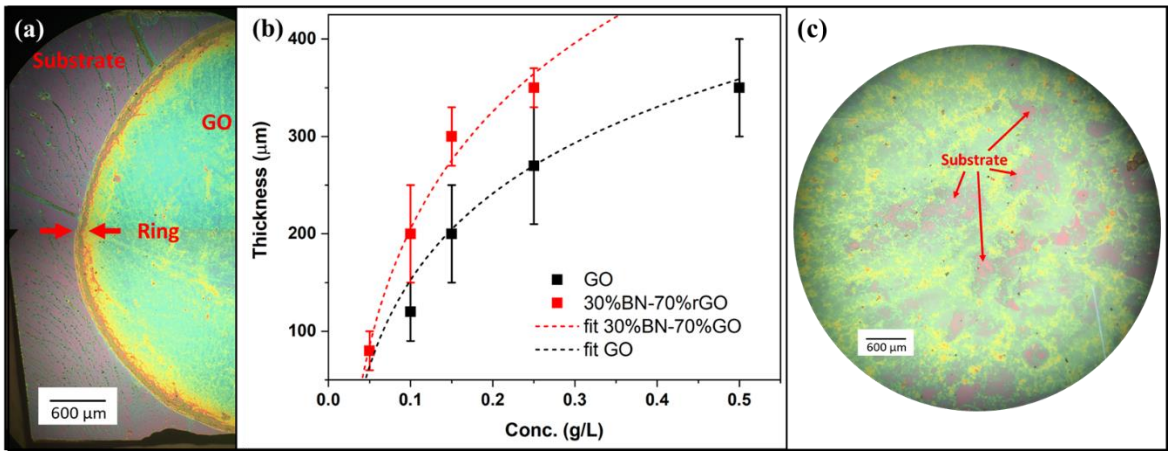

Figure 16 - (a) Optic microscope image of a drop-casted GO film. The substrate, continuous GO film, and "coffee-ring" [119] **are indicated in the image. (b) Drop-casted film thickness dependence on the GO and 30%BN-70%rGO solution concentration. (c) Optic microscope image of a drop-casted non-continuous film from 0.03 g/L GO solution.**

3.3.7.2 Controlling film thickness by plasma etching

A series of drop-casted rGO and BN-rGO were exposed to O_2 plasma etching (10 SCCM, 100 mTorr, 50 W, 25 °C) with the goal to create an ultra-thin large-area graphene-based layer onto a SiO_2/Si substrate. This route was chosen based on previous works which found the ability to create few-layer graphene from graphite [120]. Bobadilla et al. [121] found that the etch rate of graphene at 200 mTorr and 50 W was 1 atomic layer per second (~18 nm/min), while Hung et al. [122] found that the plasma etch rate of GO was 0.25 nm/min (although the plasma etching parameters were not stated). Park et al. [123] found that the plasma etch rate of hexagonal BN was 0.4 nm/min (200 mTorr, 80 W). Profilometer

measurements of the film thickness of the samples at times 0, 8, 10, and 12 min revealed the oxygen plasma etch rate of the rGO and the BN-rGO films was 6 ± 1 nm/sec. The increased rate compared to that of graphene could be partially because of the increased interlayer distance [124].

While thickness control could be achieved following a simple plasma etching process, few points should be kept in mind. First, the plasma etch rate is enhanced at the film edges, and the length of the film is also reduced with increased etching times (at a rate of 66 ± 23 μm/min). Other groups [125], [126], have also demonstrated a selective etch of graphene edges over the basal plane. Second, it was found that oxygen plasma degrades the electrical properties of graphene [127]. Exposure to oxygen plasma reduces the graphene mobility by 96% and degrades the graphene structure to a "more amorphous carbon phase". In conclusion, plasma etching is not a favorable route for an ultra-thin large-area graphene-based film deposition for electrical devices.

3.3.8 Device fabrication process

3.3.8.1 Batch 1 (B1) device fabrication

The first batch (B1) of graphene-based devices were fabricated using the following process. A series of 285-nm-thick SiO_2/p-Si substrates were cleaned in an ultrasonic bath using Acetone, IPA, and DI water, followed by air drying, and an APTES treatment [118]. The undiluted GO, rGO, and BN-rGO solutions were drop-casted onto the APTES-treated substrates and left to dry overnight at room temperature. 100 nm PMMA and 1,300 nm Ma-N 1410 were spin-coated onto the graphene-based surface, then post-baked at 100 °C for 90 sec, as schematically shown in Figure 17. Then, the samples were exposed using UV lithography through a Cr-coated glass mask, followed by Ma-D 533/S development, O_2 plasma etching (200 W, 300 mTorr, 40 sccm, 25 °C) and lift-off in Acetone. 100 nm PMMA and 1,300 nm Ma-N 1410 were spin-coated onto the samples, then post-baked at 100 °C for 90 sec. Then, the samples were exposed using UV lithography through a second Cr-coated glass mask, followed by Ma-D 533/S development, O_2 plasma etching. 20 nm Ti and 100 nm Au films were deposited using e-beam evaporator (Intlvac Nanochrome II-UHV), followed by a lift-off process in Acetone. The final devices could be observed in Figure 18, where a single 4 cm^2 substrate contains 15 individual devices.

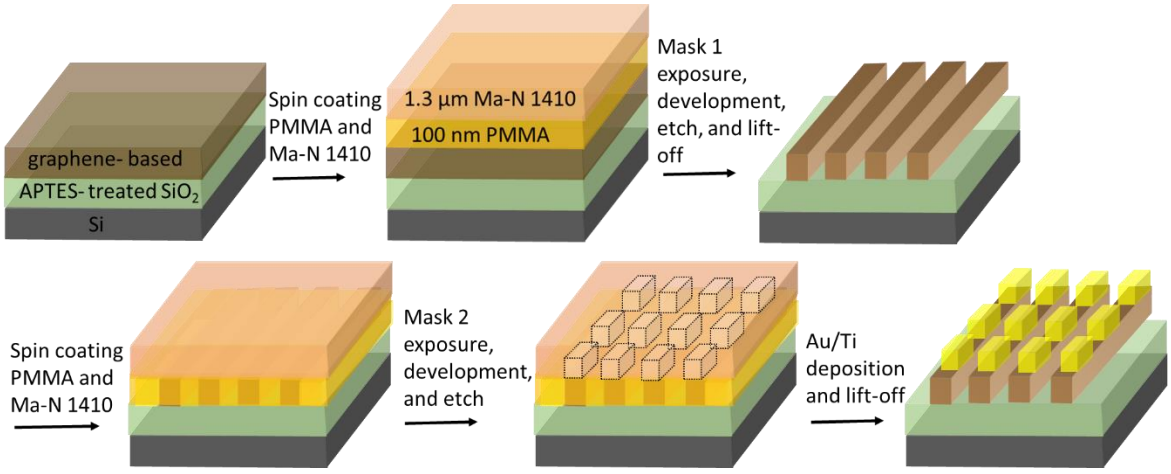

Figure 17 - Schematic diagram of GO, rGO, and BN-rGO B1 device fabrication process.

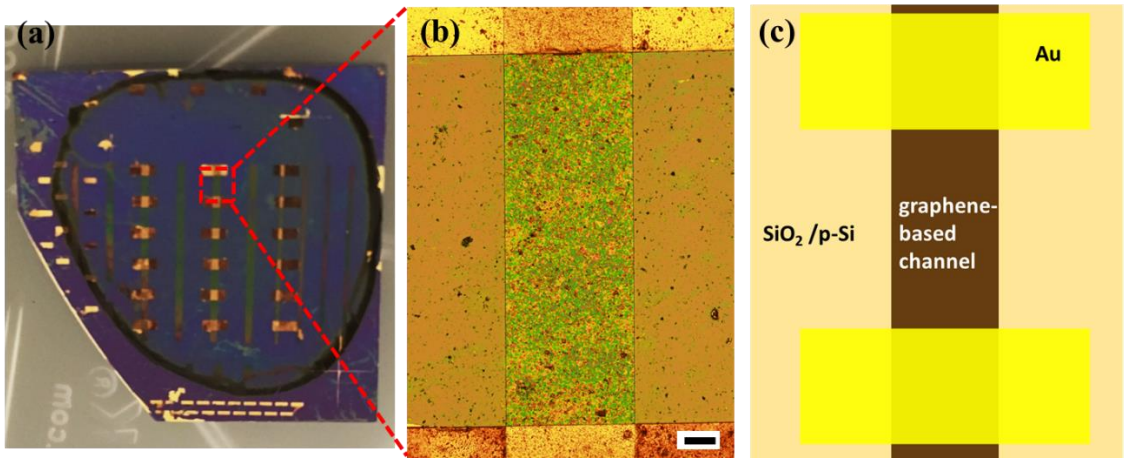

Figure 18 - Batch 1 (B1) graphene-based devices. (a) Digital image, (b) optic microscope image (scale is 100 µm), and (c) a schematic of a single device.

3.3.8.2 Batch 2 (B2) device fabrication

The second batch (B2) of graphene-based devices were fabricated using the following process. A series of 285-nm-thick SiO_2/p-Si substrates were cleaned in an ultrasonic bath using Acetone, IPA, and DI water, followed by air drying, and an APTES treatment [118]. 100 µL of the GO, rGO, and BN-rGO solutions (0.1 mg/mL) were drop-casted onto the APTES-treated substrates and left to dry overnight at room temperature, as shown in Figure 19a. 30 nm Ti and 80 nm Au films were deposited through a shadow mask using an e-beam evaporator (Intlvac Nanochrome II-UHV), as shown in Figure 19b-c.

An optic microscope image of the B2 samples revealed clean-cut lines, as shown in Figure 19d. As seen from Figure 18 and Figure 19, the channel widths and lengths were changed from 450 µm and 1.2 mm (for B1) to 2.5 mm and 0.5 or 0.7 mm (for B2), respectively.

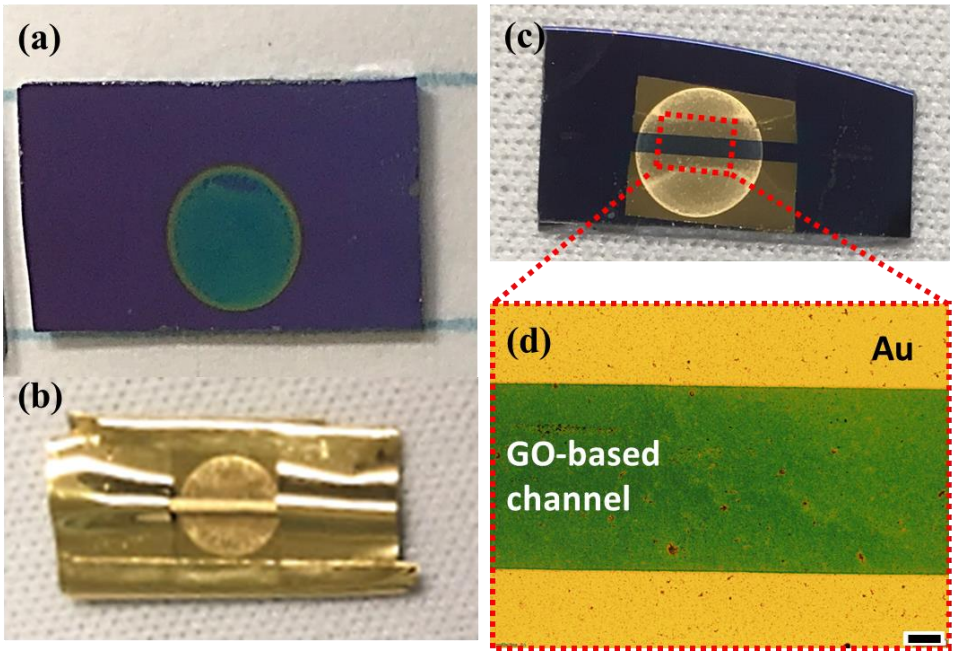

Figure 19 - Batch 2 (B2) device fabrication. Digital image of (a) graphene-based thin film on an APTES-treated SiO2/Si substrate, (b) Au/Ti deposition through a shadow mask, and (c) the B2 device. (d) Optic microscope image of the B2 device (scale bar is 100 µm).

3.3.9 Electrical performance

The B1 and B2 samples were assessed using a 2400 Keithley source measuring unit (SMU) connected to a probe station. The sheet resistance results for B1 devices were 30, 9.4, and 2.8 Gohm/sq for rGO, 5%BN-95%rGO, and 30%BN-70%rGO, respectively. These values are consistent with GO sheet resistance [128], either meaning that the laser ablation process kept the materials in their classification as insulators or that the fabrication process deteriorated the electrical properties of the materials. Further discussion would be given in the next sub-section. In contrast, electrical measurements of the B2 devices revealed much lower sheet resistance values in the range of 0.5-2 Mohm/sq for the rGO and BN-rGO films, and 11-16 Gohm/sq for the GO films, as presented in Figure 20.

From Figure 20a, the conductivity of the films was enhanced following the laser ablation treatment, and the B/N co-doping enhanced the electrical performance of the films (as seen from the 30%BN-70%rGO sample). Figure 20b supports the previous observation and confirms that the laser ablation process decreases the sheet resistance of the GO by approximately 10,000. Furthermore, the addition of B/N atoms in the form of co-doping revealed a slight decrease in the sheet resistance, especially for the samples with a channel length of L=0.5 mm. For these samples, the sheet resistance reduced from 2 Mohm/sq for rGO to 0.85, 0.77, and 0.46 Mohm/sq for 5%BN-95%rGO, 15%BN-85%rGO, and 30%BN-70%rGO, respectively. Lastly, the sheet resistance measurements reveal that the channel length affects the measurement, where longer channels (L= 0.7 mm compared to 0.5 mm) show increased sheet resistance. This phenomenon can be explained by the fact that longer channel lengths mean a larger number of boundaries between flakes. It was found [33] that the electrical mobility and resistivity are different inside the flake or in the boundary between flakes. Thus, it is possible to think of these channels as a composite material containing x volume fraction of flakes and 1-x volume fraction of boundaries.

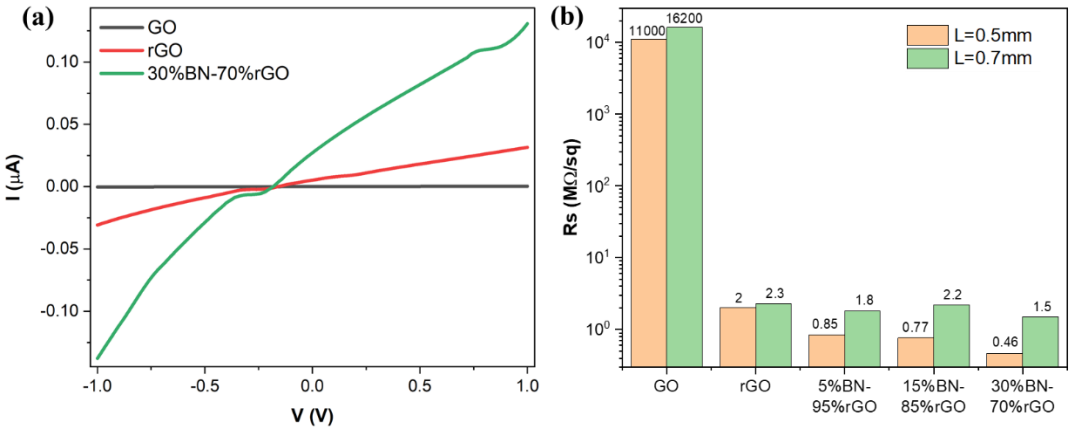

Figure 20 - The electrical characterization measurements of B1 devices. (a) I-V plots for devices with 0.7 mm channel length, and (b) sheet resistance measurements for different channel length (L) devices.

3.3.10 Issues and conclusions

In conclusion, the device fabrication process has an effect over the electrical properties of the graphene-based channels. When the thin films were exposed to the fabrication process of B1 devices (discussed in sub-section 3.3.8.1), the electrical properties of the graphene-based devices were deteriorated. This could be explained by the fact that oxygen plasma etching of graphene degrades its crystalline structure

and deteriorates its electrical performance [127]. Moreover, studies revealed that the photoresist itself leaves a residue on the surface of graphene, which reduces its electrical conductivity [25].

While using the fabrication process of B2 devices (discussed in sub-section 3.3.8.2) solves both these issues (does not use plasma etching and photoresist), the electrical performance was revealed to depend on the channel length of the device, where shorter channel lengths revealed lower sheet resistance. This difference could be understood when considering that each graphene-based nanoflake is only a few micrometers long [95], meaning that devices with longer channel length have more grain boundaries which were shown to increase the sheet resistance of graphene-based films [33].

3.4 Summary

In conclusion, laser ablation is a useful tool for GO reduction and B/N co-doping from non-hazardous precursor GO and h-BN solutions. Control over the doping concentration can be easily achieved by controlling the ratio of the two precursor solutions, where 5 vol% BN and 95 vol% GO produced the lowest co-doping (1.8 at% B and 3.4 at% N) and the 30 vol% BN and 70 vol% GO produced the highest co-doping (4.1 at% B and 5.9 at% N). While the aforementioned method allows a quick process that prevents re-stacking of the mono- to few-layer nanoflakes, it does not allow control over the doping sites.

Several efforts were made to fabricate continuous ultra-thin films from the rGO and BN-rGO solutions, but the lowest experimental thickness was much larger (~80 nm for drop-casted films and ~100 nm for plasma etched films) than the cut-off for few-layer rGO (~10 nm). This difficulty hinders the use of these solutions for large-area graphene-based applications but does not affect their use for micro-scale FET devices.

Electrical measurements of rGO and BN-rGO thin films revealed an approximate 10,000 times decrease in sheet resistance compared to GO thin films. In addition, samples with higher co-doping percentages revealed lower sheet resistance compared to rGO thin film for samples with 0.5 mm channel length. Lastly, the channel length has an effect over the sheet resistance, where longer channel length devices have higher sheet resistance (as a result from a larger number of grain boundaries).

Chapter 4
B/N co-doped GO gel

4.1 Introduction

Ultra-thin films of large-area graphene-based materials are highly desired for many transistor applications, however, the fabrication price and complexity increase proportionally with the single crystal graphene area [129]. On the other hand, using a large-area film of small graphene nanoflakes, while less costly, introduces many grain boundaries that affect the electrical performance of the device [33]. Recently, a new category of 3D graphene-based materials appeared: gels, hydrogels, foams, nanomeshes, etc. (as seen in Figure 7). There are several advantages with these types of materials, including "multi-dimensional conductivity, low mass transport resistance, abundant hierarchically porous architectures, large surface area, and excellent mechanical/chemical stability" [85]. These properties make 3D graphene-based materials attractive for large-area applications. In addition, 3D graphene-based materials should theoretically have fewer grain boundaries compared with the same film of 2D graphene-nanosheets.

This chapter explores the properties of a 3D graphene-based gel fabricated by laser ablation, as was reported in [130]. This process allows for a quick and controllable fabrication from non-hazardous precursor materials, as discussed in Chapter 3. The main properties are divided into material composition, morphology, and electrical performance. The reproducibility of the gel, enhancement strategies, and the stability in ambient conditions over time are also covered.

4.2 Synthesis method

The synthesis method described in section 3.2 was changed to allow the fabrication of a GO gel while simultaneously doping it with boron and nitrogen atoms. Two fabrication processes were performed. A Ti:Sapphire regenerative amplifier, with an operating wavelength of 800 nm, pulse duration of 35 fs, and repetition rate of 1 kHz was used in all laser ablation processes. The laser beam was focused through a lens (f=50 mm), and the focal waist was set at the air/solution interface. During the irradiation process, the solutions were stirred continuously by a magnetic stirrer to ensure homogeneity.

In the first process, the goal was to make two different gels, GO and h-BN, by following a similar fabrication process reported in [95]. For this purpose, precursor solutions were used containing 6.5 ml of each of the following:

- 6.2 mg/ml h-BN suspension in 50:50 ethanol:DI water.
- 6.2 mg/ml GO in DI water.
- Three BN-GO solutions with the same BN:GO ratios as in Chapter 3 (5%, 15%, and 30%).

All precursor solutions spent 1 hr in an ultrasonic bath for suspension. Each solution was irradiated for 60 min at a 2 W beam power. The beam waist was adjusted during irradiation to compensate for the rapid evaporation of the solution. After 60 min of irradiation, the h-BN solution changed color from white to grey and its volume reduced to 3 ml. However, the solution did not become noticeably more viscous, suggesting no gel formation [131]. All solutions containing GO had a considerable increase in viscosity and volume reduction to ~3.5 ml. Post irradiation the solutions were denoted as G_{GO}, G_1, G_2, G_3, and G_{BN}, corresponding to irradiated GO, 5%BN-95%GO, 15%BN-85%GO, 30%BN-70%GO, and h-BN, respectively.

In the second process, 6.5 ml of 1.24 mg/ml h-BN solution in 50:50 ethanol:DI water was irradiated for 55 min at room ambient with 2W beam power. The irradiated solution was then centrifuged for 15 min at 3000 RPM, and only the upper portion was extracted, with a measured concentration of 1±0.05 mg/ml. Four solutions were prepared by mixing the ablated BN solution and the GO solution at different volume percentages: 0 vol% BN and 100 vol% GO, 2 vol% BN and 98 vol% GO, 5 vol% BN and 95 vol% GO, and 15 vol% BN and 85 vol% GO. 6.5 ml of each solution was irradiated for 50 min in a similar setup as the BN solution, but with 1W beam power. During the laser ablation process, the solutions' viscosity increased until it resembled the consistency of gels. The fabricated gels containing 0 vol% BN, 2 vol% BN, 5 vol% BN and 15 vol% BN were denoted as S_0, S_1, S_2, and S_3, respectively, or BN-GO gels in general.

4.3 Characterization

4.3.1 UV-Vis absorbance

The first measurement used to identify the effect of the laser irradiation over the various solutions was UV-Vis absorbance, because it is a simple and non-destructive analysis method. It can shed light on the change in oxidation levels and possible doping [95]. The UV-Vis measurements for all produced gels are presented in Figure 21 (reproduced with permission from [130]. ©2019 Elsevier). The G_{GO} and G_1-G_3 samples exhibited an increase in the n–π* shoulder and no apparent shift in π –π* compared with the precursor GO. In addition, an increase in the peak around 200 nm with increasing h-BN

concentration was observed. These observations indicate that the G_{GO} and G_1-G_3 became gels due to the laser ablation process [131] and suggested no B and N doping [95].

In contrast, the S_0-S_3 samples revealed both gel formation and increased doping with increased h-BN concentration [130]. Thus, samples S_0-S_3 were chosen for further investigation. It is also important to note that the G_{GO} and G_1-G_3 gels were much more viscous than S_0-S_3, which complicates the deposition of ultrathin layers, as discussed in the next sub-section.

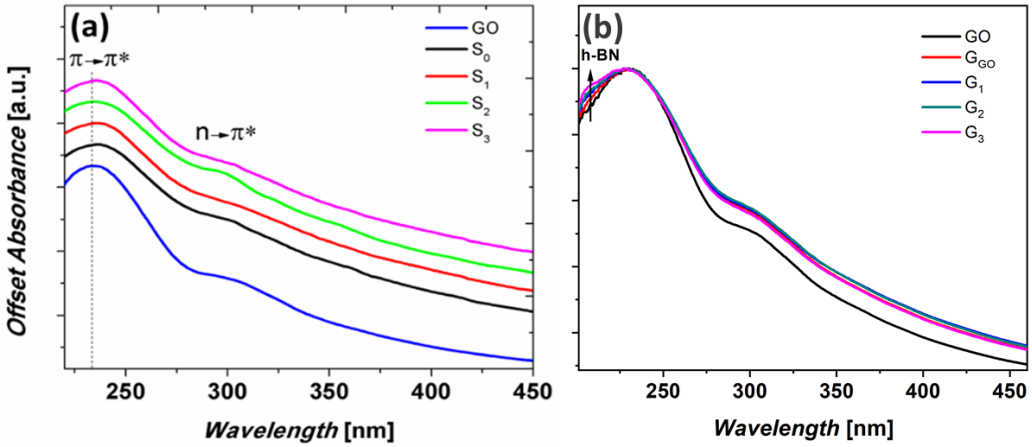

Figure 21 - UV-Vis absorbance spectra of (a) S_0-S_3 (reproduced with permission from [130]**. ©2019 Elsevier) and (b) G_{GO} and G_1-G_3 compared with precursor GO solution. The arrow in (b) represents increasing h-BN concentrations.**

4.3.2 Optical and profilometer analysis

Both gel types were deposited onto a SiO_2/Si substrate using spin-coating to study the spin-coating parameters' effect over the continuity and thickness of the film. Each spin-coating experiment had two 10-second steps. For the G_{GO} and G_1-G_3 samples, the first step had a speed of 1000 RPM, and the second step had a speed that changed between experiments to include 4000, 5000, and 6000 RPM. A ramp-up speed of 300 RPM was used in all experiments. For S_0-S_3 gels, the first step had a speed of 500 RPM, and the second step had a speed that changed between experiments to include 2200, 2500, and 2800 RPM. All samples were placed on a 95 ºC hot plate for 2 min post-deposition. The quality of the films was studied using optical microscopy and a Dektak profilometer.

For each film, the thinnest part was examined under an optical microscope and by a profilometer, as seen in Figure 22a-b. The film thickness plotted against the spin-coating speed in the second step, as seen in Figure 22c-d. As can be observed from Figure 22a-b, the gels are homogenous and continuous.

Compared with Figure 14a-b, the nanoflake size increased from ~ 5 µm for precursor GO up to 30 µm after the gel formation (as indicated by an arrow in Figure 22b). This observation suggests the growth in GO nanoflakes size, reducing the overall grain boundaries in the gel film compared to a precursor GO film. When exploring the effect of the second-step spin-coating speed over the film thickness and homogeneous area, it is found that both decrease with increasing speed, as seen in Figure 22c-d. The highest spin-coating rate for the G_{GO} sample reached 6000 RPM, which was the highest available speed in the spin-coater, gave a film thickness of 35±20 nm. The highest second-step spin-coating speed for the S_0 sample that provided a continuous film was 2800 RPM, which gave a film thickness of 25±15 nm. Considering S_0-S_3 samples were easier to deposit as an ultra-thin layer and were expected to be doped with B and N atoms (as discussed in section 4.2), these samples were further studied using various microscopy and spectroscopy tools, as will be discussed in the coming sub-sections (sections 4.3.3-4.3.4).

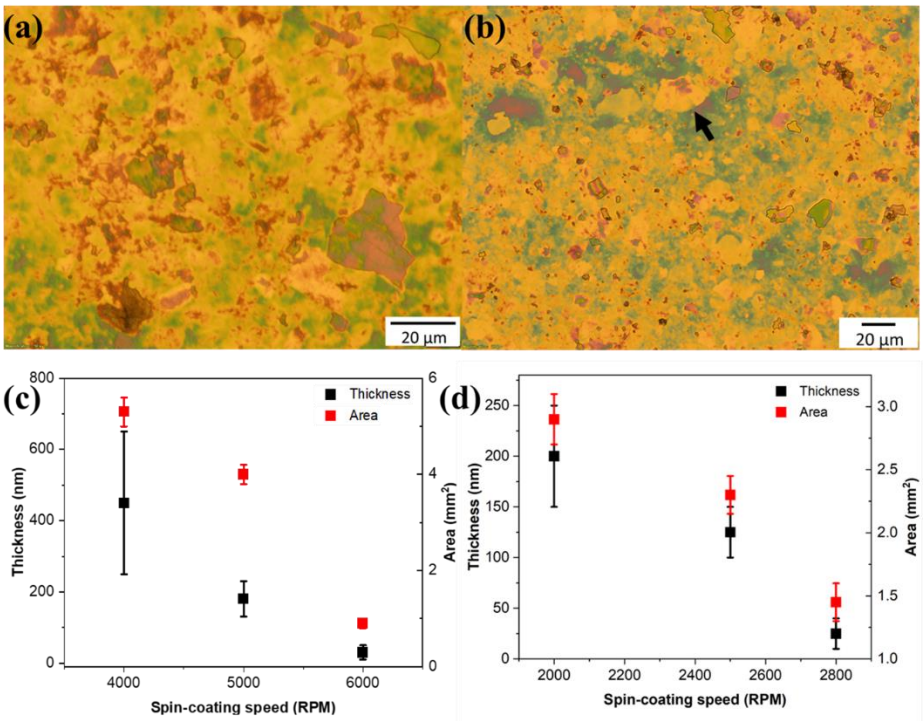

Figure 22 - (a) and (b) are optic microscopy images of G_{GO} and S_0 with a second-step spin coating speed of 5000 and 2500, respectively. (c) and (d) are the dependence of the film thickness and homogeneous area over the spin-coating speed in the second step for G_{GO} and S_0, respectively.

It was later found that small tweaks to the deposition process could increase the homogeneity of the area up to 4.3 ± 0.3 mm^2 for an S_0 thin film thickness of ~50 nm. The spin-coating process was as

follows: first, the substrate spends 5 minutes on a 200 ºC hot plate. Second, the gel was dropped onto the surface at room temperatures and rests for 3 seconds. Then, the samples were spun at a speed of 500 RPM with 200 RPM ramp-up speed for 10 seconds and then another 2800 RPM with a ramp-up at a speed of 300 RPM for 10 seconds.

4.3.3 XPS and Raman spectroscopy

This sub-section discusses the compositional analysis of the S_0-S_3, as was discussed in detail in [130]. A series of thin films were drop-casted onto SiO_2/Si substrates for Raman and XPS analysis (using a Horiba HR800 Spectrometer equipped with a 532 nm excitation source and Thermo ESCALAB 250 with an unmonochromatic AlKa X-ray source and incident energy of 1486.6 eV, respectively). Analysis of the Raman and XPS results are summarized in Table 9 (reused with permission from [130]. ©2019 Elsevier) and Table 10, respectively.

Table 9 - Raman spectroscopy analysis of thin films made of S_0-S_3 gels (reused with permission from [130]**. ©2019 Elsevier).**

	D (cm^{-1})	G (cm^{-1})	I_D	I_G	I_D/I_G	2D (cm^{-1})	$I_{G'}$	$I_{G'}/I_G$
GO	1345	1587.4	106.5	78.4	1.36	2708.6	50.2	0.64
S_0	1347	1592.6	97.3	76.5	1.27	2693.90	42	0.55
S_1	1347.8	1591.9	94.6	72.8	1.30	2692.3	44.3	0.61
S_2	1347.2	1590.7	96.3	73.1	1.32	2695.9	36.1	0.49
S_3	1346.7	1590.6	102.6	71.4	1.44	2691.6	33.2	0.46

From Table 9 and Table 5, after the laser ablation process, the gels had: (1) restored conjugation, (2) shortening of sp^2 domain lengths due to doping and vacancy, (3) increased dopant concentration, and (4) increased p-type doping with increasing h-BN concentration in the precursor [130]. These observations confirm the UV-Vis absorbance analysis since it affirms that the gels were doped but could not confirm the gel formation. For this reason, and to better understand the doping concentrations and doping sites, the films were also studied by XPS.

The XPS analysis is summarized in Table 10 and Figure 23 (reused with permission from [130]. ©2019 Elsevier). As seen from the table, there is an increased conjugation post-laser treatment as observed from the increase in C-C bonds concentration (by 1.3-3.5 at%). The high concentration of C-O-C bonds confirm the gel formation post-laser ablation, which act as "bridges" that connect different

nanoflakes to a 3D network [131]. Interestingly, the atomic percentage of O-C=O bonds increased from 3.5 at% for GO to 10.2-12.9 at% for the S_0-S_3 gels. These bonds can be thereafter used for bioreceptor immobilization [132].

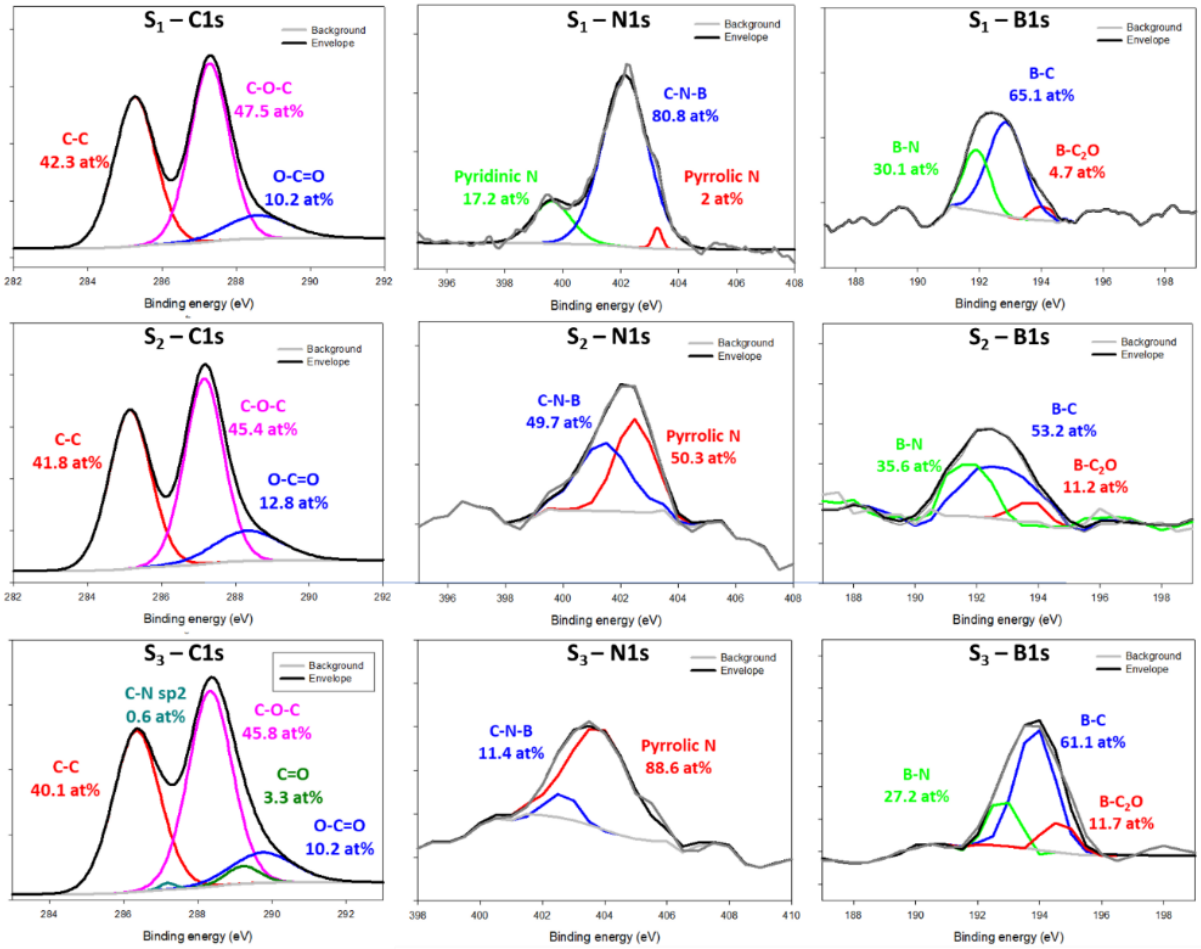

Figure 23 – XPS spectrum analysis of C1s (left column), N1s (center column), and B1s (right column) of S_1-S_3 gels. Reused with permission from [130]**. ©2019 Elsevier.**

From Table 10 and Figure 23, "N doping was increased from 0.5 at% in S_1 and S_2 to 1.3 at% in S_3. B doping was gradually increased from 0.3 at% to 0.5 at%, and to 1 at% in S_1-S_3, respectively. The total B/N co-doping percentage was calculated as 0.8 at% in S_1, 1 at% in S_2, and 2.3 at% in S_3, suggesting that control over the doping percentage and types can be gained by controlling the vol% of BN in the precursor solution" [130]. The dominant N dopant was Pyridinic N and Pyrrolic N for S_1 and S_2-S_3 samples, respectively, while the dominant B dopant was through a substitutional site (according to the B-C_3 bond concentrations).

Table 10 - XPS analysis of GO and S_0-S_3 thin films.

Transition	Bond type	Composition (at%)				
		GO	S_0	S_1	S_2	S_3
C1s	C-C	38.8	41	42.3	41.8	40.1
	C-O-C	56	46	47.5	45.4	45.8
	O-C=O	3.5	12.9	10.2	12.8	10.2
	C-O	1.7	0	0	0	0
	C-N sp^2	0	0	0	0	0.6
N1s	C-N-B	0	0	80.8	49.7	11.4
	Pyrrolic N			2	50.3	88.6
	Pyridinic N			17.2	0	0
B1s	B-N	0	0	30.1	35.6	27.2
	B-C_3			65.1	53.2	61.1
	B-C_2O			4.7	11.2	11.7

4.3.4 Additional characterization

Figure 24 demonstrates the 3D structure of the BN-GO gel (reused with permission from [130]. ©2019 Elsevier). As seen from the image, the gel structure is beyond 10 μm in length, a large increase from the nanoflake size of the precursor GO. Figure 25a-c demonstrates the SEM images of rGO nanoflakes, S_1 3D structure, and S_0 thin film morphology, respectively. As seen from the figure, the 2D structure of the ~2 μm long rGO nanoflake becomes a 3D ~16 μm long structure. It is also evident from Figure 25c that the film has curved surfaces. Figure 25d presents a schematic of the S_1-S_3 chemical structure, based on the optical, AFM, XPS analysis, and the electrical measurements in Section 4.4. The nanoflakes are connected by C-O-C "bridges" to form a B and N co-doped GO gel structure. This "bridges" are providing interflake conduction pathways, thus, effectively reducing some of the grain boundaries compared with a "non-gel" structure.

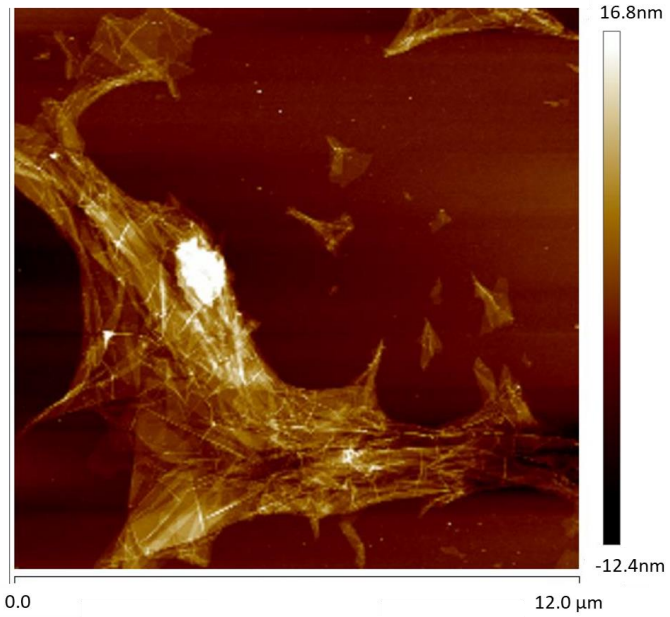

Figure 24 - AFM image of the 3D structure of the BN-GO gel (reused with permission from [130]**. ©2019 Elsevier).**

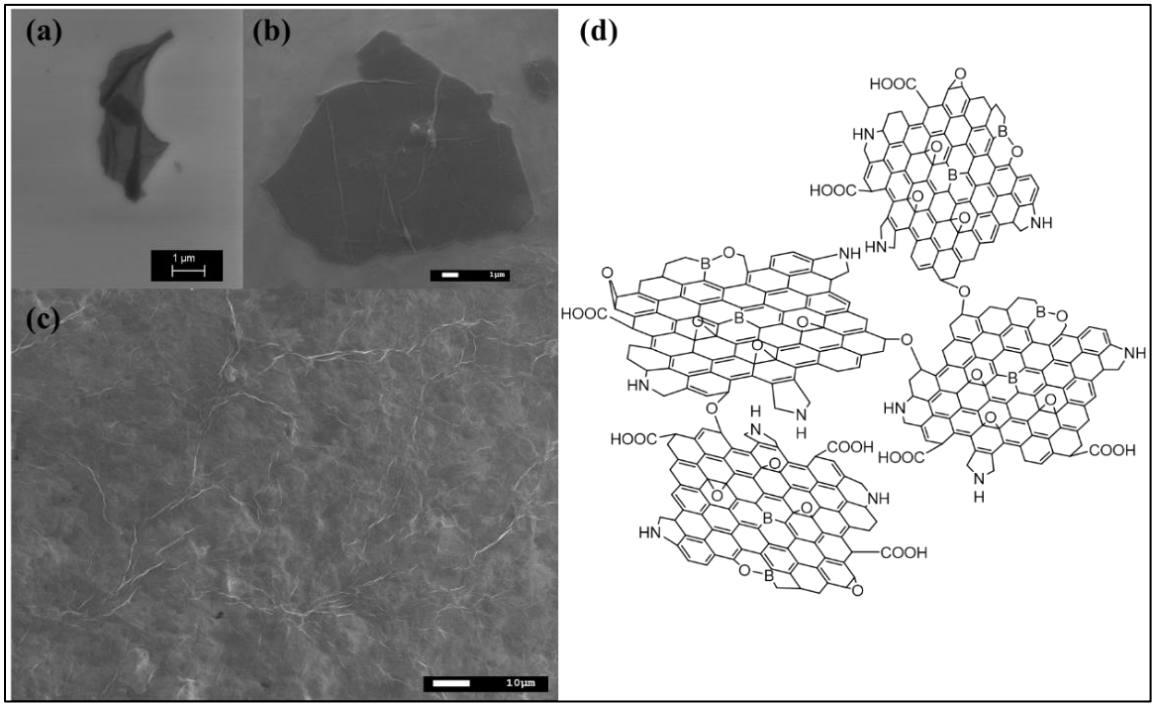

Figure 25 - SEM image of (a) rGO nanoflakes, (b) S_1 3D structure, (c) S_0 film, and (d) schematic 3D structure of BN-GO gels.

The reduction in grain boundaries and increase in chemical reactivity following the incorporation of B and N atoms into the gel structure was confirmed by measuring the contact angle of a DI water droplet on the gels' surface. S_0-S_3 were deposited onto a Si substrate and left to dry at room temperature overnight. A 50 µm DI water droplet was drop-casted onto each gel, and the samples were photographed using an iPhone camera, as seen in Figure 26 (reused with permission from [130]. ©2019 Elsevier). As may be observed from the figure, the contact angle decreased with increased B and N doping, confirming the increased chemical reactivity of the gels [133].

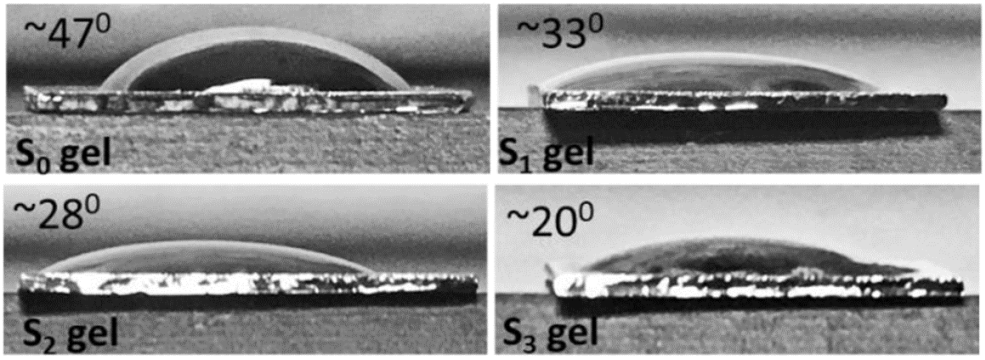

Figure 26 - Contact angle measurements of S_0-S_3 gels using DI water droplets on the gel's surfaces (reused with permission from [130]**. ©2019 Elsevier).**

4.4 Device fabrication and electrical properties

Two different device types were fabricated. The first type had top-electrodes, where the electrodes were deposited onto the graphene channel without a gate electrode. The second type had bottom-electrodes, where the source, drain, and gate electrodes were pre-patterned before the deposition of the S_0-S_3 gels.

4.4.1 Top-electrode devices

Approximately 2x2cm^2 p-doped silicon substrates with a 285nm oxide layer were cleaned in an ultrasonic bath in Acetone, IPA, and DI water, followed by air drying. The BN-GO gels were spin-coated onto the clean SiO_2/Si substrates in the method previously described. Source, drain, and back-gate Au(50 nm)/Ti(30 nm) electrodes were deposited on the substrates through a shadow mask using an Intlvac Nanochrome II—UHV system. The back-gate electrode had contact with the p-doped Si from the side, as discussed in [130]. A schematic of the top-electrode FET device with the BN-GO gels as the channel material can be seen in Figure 27a.

The top-gated device's sheet resistance was measured using a 2400 Keithley SMU connected to a probe station. It was found that the back-gate electrode had minimal control over a voltage range of -5-5 V, suggesting that the lack of sample cleaning between the gel deposition and the electrodes deposition is responsible for a poor gate contact. The average sheet resistivity (ρ_s) was calculated based on 7 measurements for each gel, as presented in Figure 27b. As seen in the figure, the sheet resistivity reduced from more than 10^7 kΩ/sq for precursor GO to ~3000 kΩ/sq for S_0 gel, confirming the restored conjugation of the gel, and may suggest less grain boundaries [33]. It may also be observed that the sheet resistivity further decreases with increased doping, down to ~11 kΩ/sq for S_3 gel.

The sheet resistivity results of the gels were fitted with equation 4, which gave an R^2 value of 0.983, as presented in the inset of Figure 27b. C in equation 4 represents the total B and N doping:

$$\rho_s = 12 + 3889e^{-C/0.29} \qquad (4)$$

It is clear from equation 4 that the sheet resistivity saturates at 12 kΩ/sq for total doping values larger than 3 at%. Whilst these values are in-line with values found for rGO [134], they are ~10 times larger than those observed for N-doped graphene [48], and ~100 times larger than pristine graphene [38].

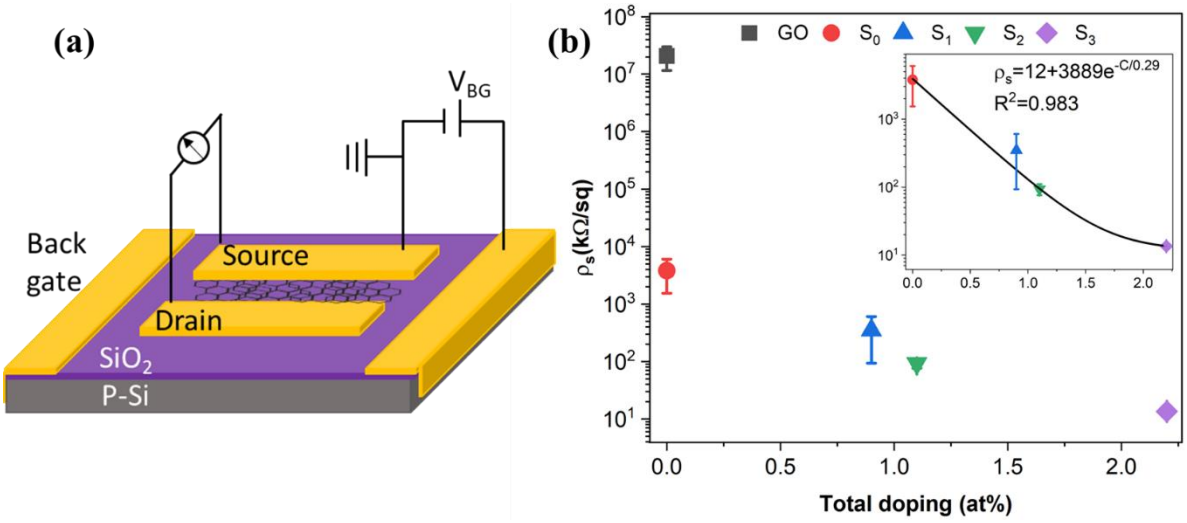

Figure 27 - (a) A schematic configuration of the top-electrode FET device with BN-GO gel as the channel material. (b) Average sheet resistivity of precursor GO and S_0-S_3 gels as measured from top-electrode devices. The inset is an exponential decay fit.

4.4.2 Bottom-electrode devices

Approximately 2x2cm^2 p-doped silicon substrates with a 285nm oxide layer were cleaned in an ultrasonic bath in Acetone, IPA, and DI water, followed by air drying. Source, drain, and back-gate Au(50 nm)/Ti(30 nm) electrodes were deposited on the substrates through a shadow mask using an Intlvac Nanochrome II—UHV system. The samples were then cleaned in an ultrasonic bath in Acetone and IPA, followed by nitrogen drying. The gels were spin-coated onto the channels following two-step spin-coating. First, the samples are spun at a speed of 500 RPM with 300 RPM ramp-up speed for 10 seconds and then another 2850 RPM with a ramp-up at a rate of 300 RPM for 10 seconds. Any gel between the source and gate or drain and gate electrodes was removed with a tweezer. The difference between the top-electrode and bottom-electrode devices can be seen in Figure 28a.

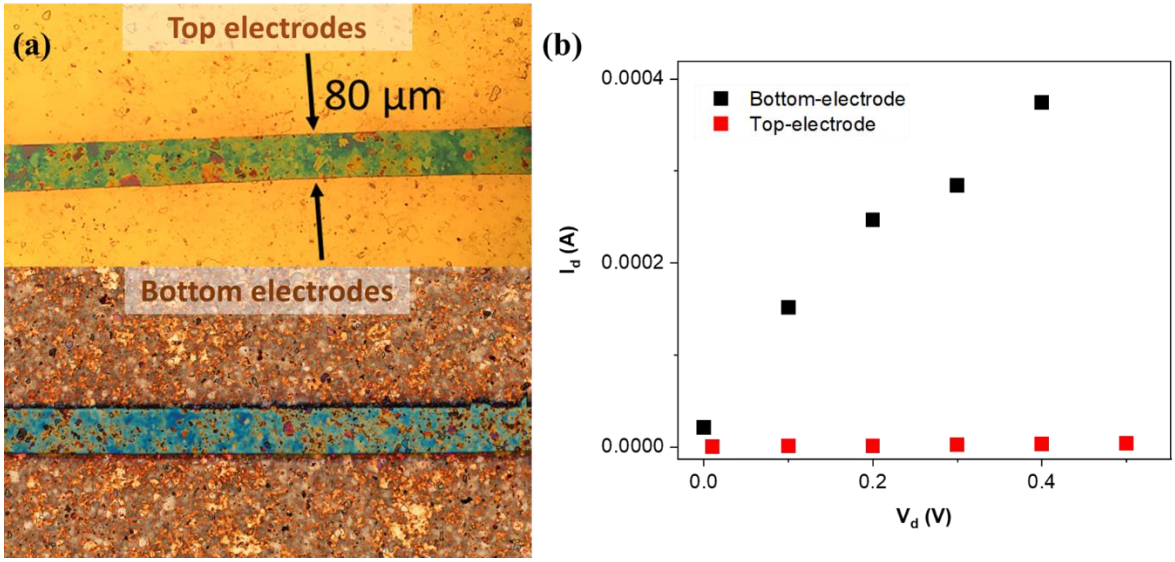

Figure 28 - (a) An optic microscope image of S_1 gel with top and bottom source and drain electrodes. The channel length is 80 µm in both devices. (b) The I_d-V_d plots of top and bottom-electrode devices (gate voltage=0 V).

The electrical characterization was obtained using two Keithley 2400 SMUs. One SMU was used to supply a back-gate voltage, while the second SMU supplied the drain voltage and measured the drain current. The source was grounded. A laptop controlled and synchronized the two SMUs through serial ports and recorded their measurements. All measurements were performed at room temperature.

The I_d-V_d plots of top and bottom-electrode devices with no gate are presented in Figure 28b. As seen from the figure, the current of the bottom-electrode device is approximately 1000 times larger than

that of the top-electrode device (I_d =2.9 µA) for the same applied drain voltage. In addition, the bottom-electrode devices exhibited good gate control in the range of -4-4 V (Figure 29a-b). The I_d-V_g of the BN-GO gels were plotted for different drain voltages. The graphs showed good repeatability when plotted from -2 V to 2 V (referred to as up sweep) or from 2 V to -2 V (referred to as down sweep). The gels exhibited a repeatable I_d-V_d plot when measured 50 days apart [130].

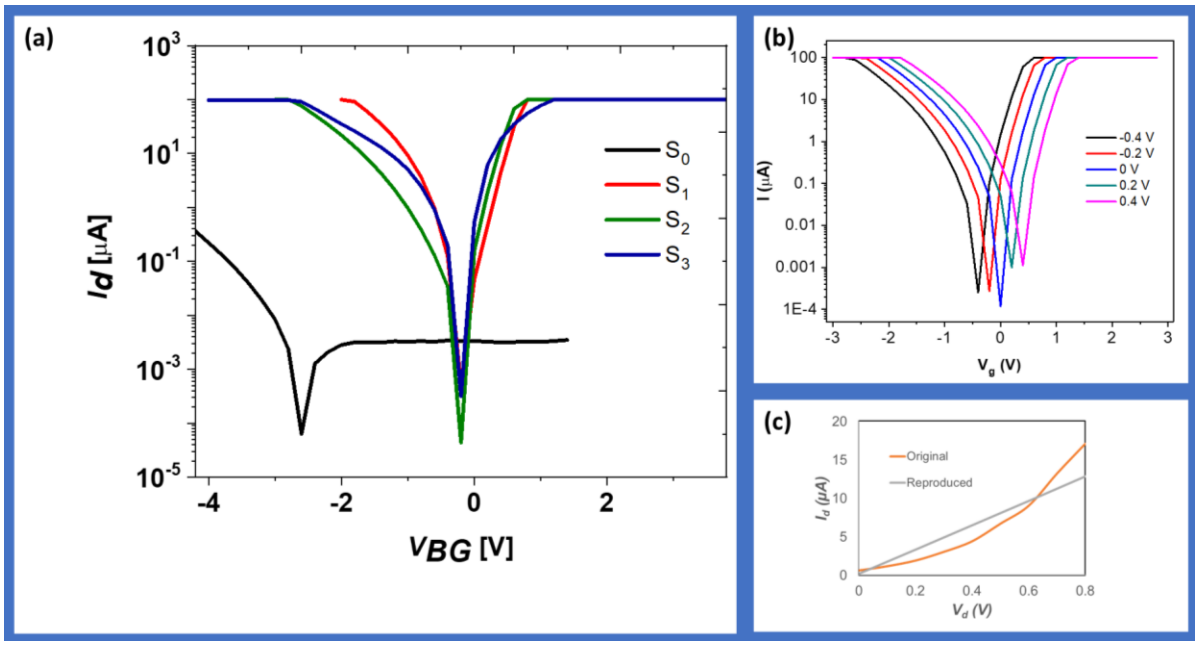

Figure 29 - (a) Drain current vs gate voltage characteristics of the BN-GO gels for a constant drain voltage of -0.1 V. (b) Drain current vs gate voltage characteristics of S_2 gel for a sweep in drain voltage. (c) The electrical behavior of S_2 gels fabricated at different times (reused with permission from [130]**. ©2019 Elsevier).**

Several electrical performance parameters were extracted from the graphs: the ON and OFF currents, the ON/OFF current ratios, and the electron and hole mobilities. The ON current is defined as the largest drain current the device can reach, while the OFF current is the current at the Dirac point [57]. The electron and hole mobilities can be extracted from equation 6, where µ is the mobility, g_m is the transconductance, C_{ox} is the SiO_2 capacitance, and W and L are the channel width and length, respectively. The extracted values are summarized in Table 11 (reused with permission from [130]. ©2019 Elsevier).

$$\mu = \frac{g_m L}{W V_d C_{ox}} \qquad (6)$$

Table 11 - The electron and hole mobilities and the I_{ON}/I_{OFF} ratios of the S_0-S_3 gels (reused with permission from [130]**. ©2019 Elsevier).**

Channel	S_0			S_1					S_2				S_3				
Sample #	1	2	3	1	2	3	4	5	1	2	3	4	1	2	3	4	5
μe (cm^2/Vs)	1.7	0.8	3.8	103.9	187.1	483.3	404.8	509.5	758.3	1013.1	1181.2	521.0	534.0	32.2	229.3	535.0	548.8
μh (cm^2/Vs)	4.1	0.2	5.2	503	482	272.9	346.5	263.2	320.6	8165	5885	262.6	284.4	40.1	210.5	155.3	329.7
I_{ON}/I_{OFF} (E+03)	2	1	21	1	1	144.8	227	195	113.6	104	2274	368	0.2	31	315	151	243

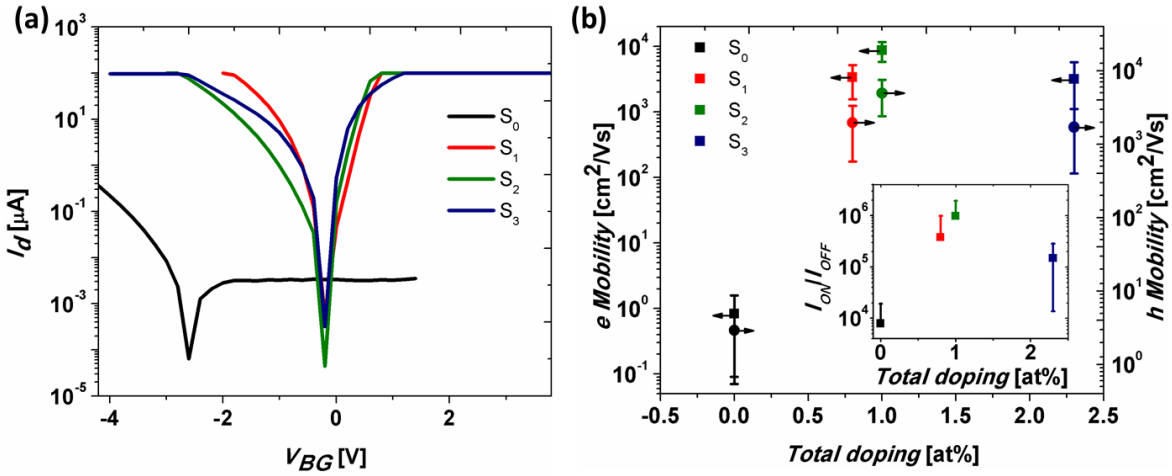

Figure 30 - The electrical properties of the S_0-S_3 gel FETs at room temperature. (a) The drain current vs back gate voltage for a constant (-0.1 V) drain voltage measured for S_0-S_3 gel FETs. (b) The average electron and hole mobilities and I_{ON}/I_{OFF} ratios (in the inset) of the S_0-S_3 gel FETs (reused with permission from [130]**. ©2019 Elsevier).**

Figure 30a presents the I_d-V_g for a constant V_d=-0.1 V of the S_0-S_3 gels (reused with permission from [130]. ©2019 Elsevier). As seen from the figure, the ON current is identical (~100 μA) for the doped gels, while much lower (~0.3 μA) for the S_0 gel. In contrast, the OFF current was lowest for the S_0 and S_2 gels. Figure 30b presents the average electron and hole mobilities and I_{ON}/I_{OFF} ratios (in the inset) of the S_0-S_3 gel FETs, as calculated from Table 11 (reused with permission from [130]. ©2019 Elsevier). As may be observed, the S_0 gel exhibits the lowest mobilities and I_{ON}/I_{OFF} ratio, while the S_2 gel exhibits the highest. The electron, hole, and I_{ON}/I_{OFF} ratio of S_2 were calculated as 9000 ± 3000 cm^2/Vs and 6000 ± 2600 cm^2/Vs, and ~10^6, respectively. S_1 and S_3 gels exhibited slightly worse mobilities and I_{ON}/I_{OFF}

ratios compared to S_2 gel, suggesting that the improvement of the electrical properties saturates for approximately 1 at% of total dopants, and then further introduction of dopants increases scattering and reduces the electrical performance [135].

Table 12 - The room-temperature electrical properties of the state-of-the-art graphene-based FETs.

Graphene type	Fabrication process	Mobility (cm^2/VS)	I_{ON}/I_{OFF}	Substrate	Length (μm)	Ref.
Pristine graphene	Exfoliated multilayer	6,000	-	SiO_2/Si	5	[136]
	Exfoliated	5700	~13	h-BN/ SiO_2/Si	1000	[34]
	Exfoliated	40,000	-	h-BN/ SiO_2/Si	2	[35]
	LEG	1200	~6.7	SiO_2	3000	[65]
	CVD	1,700-3,500	~100	h-BN/ SiO_2/Si	160	[137]
	Monolayer CVD	3,300	~7.5	SiO_2/Si	290	[138]
	CVD	450	~7	Al_2O_3/ SiO_2/Si	30	[139]
	single-crystalline monolayer CVD	12,000	-	h-BN/ SiO_2/Si	~1	[140]
	single-crystalline monolayer CVD	13,500	~100	h-BN	~6	[141]
	MOCVD-grown	100	100	SiO_2/Si	0.1	[142]
	CVD	900	~4	h-BN/ SiO_2/Si	1000	[34]
	CVD	5400	~5	Quartz	250	[37]
	CVD	~3000	~1	SiO_2/Si	50	[78]
	CVD	~2750	11	SiO_2/Si	2	[72]
	CVD	845	-	Si_3N_4/ poly-Si/ p-Si	100,000	[143]
	Transfer- free CVD	4,820	-	Glass	40,000	[144]
	Monolayer CVD	1,695	3.5	SiO_2/Si	250	[145]
	CVD	2700	360	SiO_2/Si	150000	[66]
	LPCVD	~2000	~1.5	SiO_2	100	[69]
	CVD	~17	1000	polyethylene terephthalate	2	[70]
	Epitaxial	3200	-	SiC	600	[39]
	Epitaxial	4700	-	SiC	5	[40]
rGO	Photothermal rGO	0.17	111	Polyethylene terephthalate	500	[43]
	Hydrazine rGO	~630	>500	SiO_2/Si	2000	[44]

	Pulsed laser rGO	5	-	SiO_2/Si	100	[46]
	rGO	~1300	~900	SiO_2/Si	60	[75]
Doped graphene	5.6 at% N-doped	12	~2	SiO_2/Si	40	[146]
	3.4 at% N-doped	630	~1400	SiO_2/Si	450	[147]
	7.49 at% N-doped	1.3	~4	SiO_2/Si	20	[47]
	9.69 at% N-doped	0.9				
	MoO_3-doped	2700	7.5	SiO_2/Si	10	[49]
Heterostructure	MoS_2/graphene	600	~100	SiO_2	5	[42]
	h-BN/graphene	100000	~150	SiO_2	2	[50]
	h-BN/graphene	18000	~4	SiO_2	2	[51]
	h-BN/graphene	7000	~20	SiO_2/Si	10	[17]
	h-BN/MoS_2/graphene	~1	10^6	SiO_2/Si	5	[18]
Hybrid	Graphene/Pt	1200	~3	SiO_2/Si	100	[52]
	rGO/TiO_2 composite	~4.5	~2	SiO_2/Si	200	[53]
	Hydrazine rGO/Pt NPs	~140	~1.4	SiO_2/Si	60	[73]
	MEH-PPV/PbS QDs/ graphene	180	~5	SiO_2/Si	2500	[54]
	MoS_2/graphene	~4300	~6	SiO_2/Si	10000	[67]
Gel	BN-GO gel	9000	10^6	SiO_2/Si	100	This work

The room-temperature electrical properties of the gels were compared to the state-of-the-art graphene-based materials, as summarized in Table 12. As seen from the table, the electrical performance depends on the channel length, fabrication process, and substrate material. The charge carrier mobility of pristine graphene covers a wide range of ~17-40,000 cm^2/Vs, with the largest mobility reported for an h-BN/SiO_2/Si substrate [35], which has reduced charge scattering compared to a SiO_2/Si substrate. While the largest mobilities overall were observed for heterostructure graphene with a range of 1-100,000 cm^2/Vs, recorded for short channel lengths of 2-10 μm. Doped graphene and rGO structures have low mobility ranges of 0.9-630 cm^2/Vs, 0.17-1,300 cm^2/Vs, respectively, while

hybrid structures have moderate to high mobilities of 4.5-4,300 cm^2/Vs. The I_{ON}/I_{OFF} ratios for all graphene-based materials stretch over 1.5-1,400, with a single exception of 10^6 [18]. However, the same device gave very low mobility at room temperature, reaching only 630 cm^2/Vs.

Figure 31 visually presents the data summarized in Table 12. In Figure 31a, the reported mobilities are plotted against the I_{ON}/I_{OFF} ratios. As previously mentioned, the preferred device would have both as high as possible; therefore, should appear in the top right corner of the graph. However, from the graph and Table 12, it seems that there is a tradeoff between the mobility and the I_{ON}/I_{OFF} ratio. For example, when the mobility is high (18,000 cm^2/Vs) [51], the I_{ON}/I_{OFF} ratio is low (~4). In contrast, the BN-GO gel discussed in this thesis showed high mobility and extremely high I_{ON}/I_{OFF} ratio and is the only device in the top-right corner of the graph.

Figure 31b-c presents the mobility and the I_{ON}/I_{OFF} ratio versus the channel length of the devices in Table 12. Theoretically, an increased channel length will translate to increased charge scattering from the grain boundaries, resulting in reduced electrical performance [130]. This effect, however, is only apparent in Figure 31b, where the mobility reduces by more than an order of magnitude when the channel length increases from 1-2 µm to 10 µm. For short channel length, a single graphene nanoflake can cover the length of the channel. When increasing the channel length above the average length of the nanoflake, inter-flake boundaries scatter the charge carriers thus reducing the overall mobility [33]. It is also interesting to note that the BN-GO gel was comparable to short-channel pristine graphene and graphene heterostructures, all fabricated in a more costly manner (as discussed in Chapters 2-3).

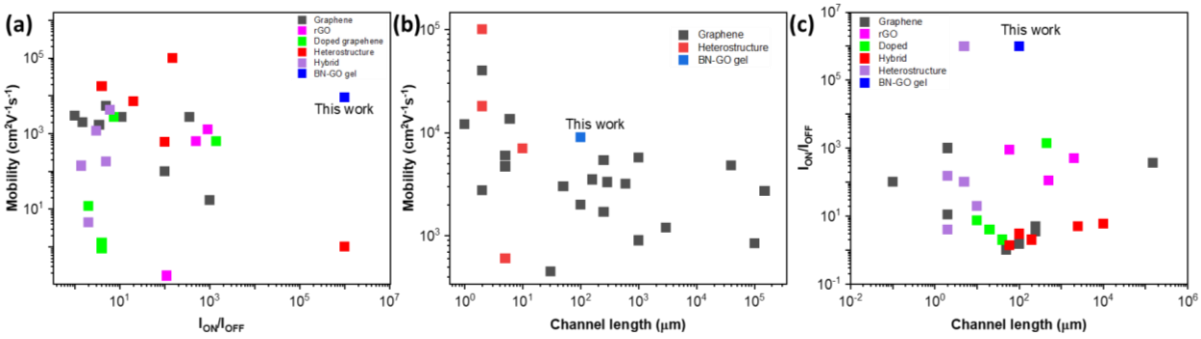

Figure 31 - The room-temperature electrical performance of BN-GO gel FETs compared to the state-of-the-art graphene-based FETs. (a) Mobility vs I_{ON}/I_{OFF}, (b) mobility vs channel length, and (c) I_{ON}/I_{OFF} vs channel length.

4.5 Reproducibility and stability

Reproducibility and stability are two critical measures of a successful fabrication process and device performance [148]. In order to investigate the repeatability, the S_2 gel was fabricated from scratch on a different occasion following the same fabrication process discussed above. An FET device with the gel as a top channel was deposited using spin-coating and measure using an SMU device. The electrical behavior was compared to the original S_2 gel, demonstrating similar currents over the same voltage range as for the original gel (Figure 29c).

The air-stability of the gels was measured over a 30-day, 50-day, and 2 years periods, as seen in Figure 32. Over a 50-day period, the electrical behavior is roughly the same with an ON current, OFF current, and I_{ON}/I_{OFF} ratio within a 20-100 µA, 0.1-0.2 nA, and 200,000-500,000 range, respectively. After a 2-year period, the ON and OFF current values are reduced to ~2 µA and ~0.01 nA, respectively, while the I_{ON}/I_{OFF} ratio remains 200,000. This observation indicates that the deterioration rate in the ON current is approximately 0.14% per day. In addition, the Dirac peak shifts to negative values, suggesting increased p-type doping which is expected to stem from the oxidation of the gels [46].

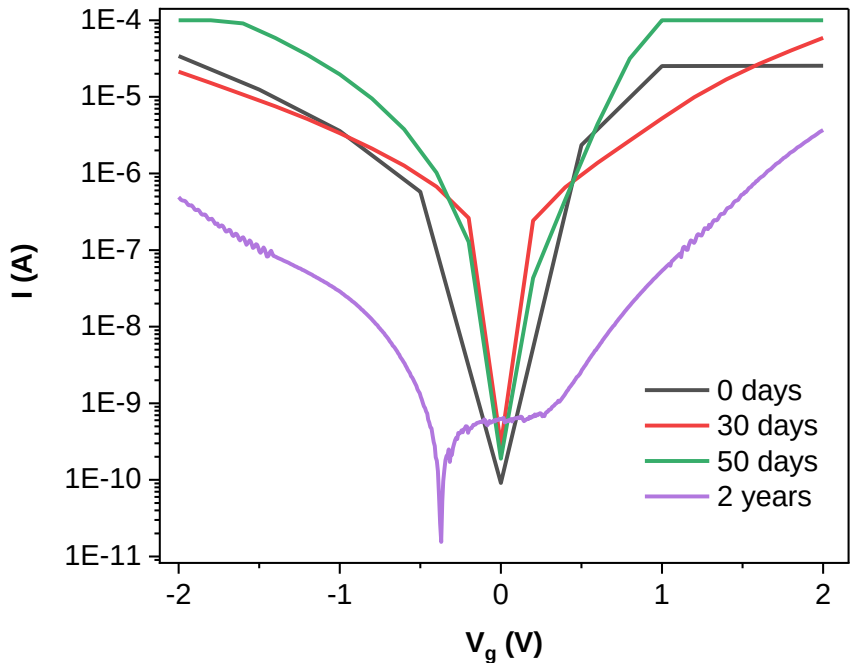

Figure 32 - The electrical stability of S_1 FET measured 30 and 50 days apart and after 2 years. V_{ds}=-0.1 V for all measurements.

Shin et al. [149] demonstrated improved air stability of their graphene FET by inserting a fluoropolymer layer between the graphene and the SiO_2/Si substrate. However, their device's stability was measured over a short 3-week period with the ON current reducing from 450 to 400 µA, and the long-term stability is unclear. Xu et al. [148] demonstrated a continuous reduction in the ON current from 420 nA to 340 nA and in the I_{ON}/I_{OFF} ratio from ~4.2 to ~3.4 in a 41-day interval. Peng et al. demonstrated the improved air-stability of an rGO FET during a 3-day period when an rGO and octadecyltrichlorosilane (OTS) heterostructure is used. Without the OTS, the ON current degradation rate is estimated as 7.5% per day, while the rGO-OTS heterostructure has a degradation rate of ~5.6% per day. Compared with these reports, the gels discussed in this thesis have enhanced air-stability over a more extended time and demonstrated no noticeable degradation for 50 days.

4.6 Device enhancement strategies

4.6.1 Electrical performance for increased laser ablation intensity

Gel S_2 was reproduced with the same fabrication process discussed but for at least three times shorter pulse duration (~10 fs). Since the beam's energy was kept constant, the shorter pulse durations translated to higher laser ablation intensities [150]. The electrical properties, chemical structure, and morphology of the "new" S_2 gels were reported in [151]. As was reported, the ON and OFF currents and the I_{ON}/I_{OFF} increased to 20 mA, 0.6 nA, and ~10^7. "In addition, the charge carrier mobilities were calculated as 440,000±200,000 $cm^2V^{-1}s^{-1}$ and 8,700 $cm^2V^{-1}s^{-1}$ for holes and electrons, respectively. This observation was a great increase from the values observed for the "old" gel of 5,000±2,500 $cm^2V^{-1}s^{-1}$ and 8,700±3,000 $cm^2V^{-1}s^{-1}$ for holes and electrons, respectively" [151]. The difference in electrical properties may stem from the higher laser ablation intensity, which in turn can break more bonds in the same process duration [150].

The XPS analysis of the "new" gel is presented in Figure 33 (reused with permission from [151]. ©2021 Elsevier) revealed approximately 2 at% more C-C bonds than the old gel, indicating a restored conjugation in the "new" gel [33]. In addition, the N-dopants were attached in the pyridinic locations (21.7 at% of the N 1s peak) and the C-N-B locations, while the B-dopants were through the substitutional site (with a B-C bond giving 4.4 at% of the B 1s peak). In the "old" gels, some N-doping was through pyrrolic sites, which cause more scattering compared to pyridinic sites [152]. The reduced structural defects and restored conjugation in the "new" gel are expected to increase the charge carrier mobility compared to the "old" gel.

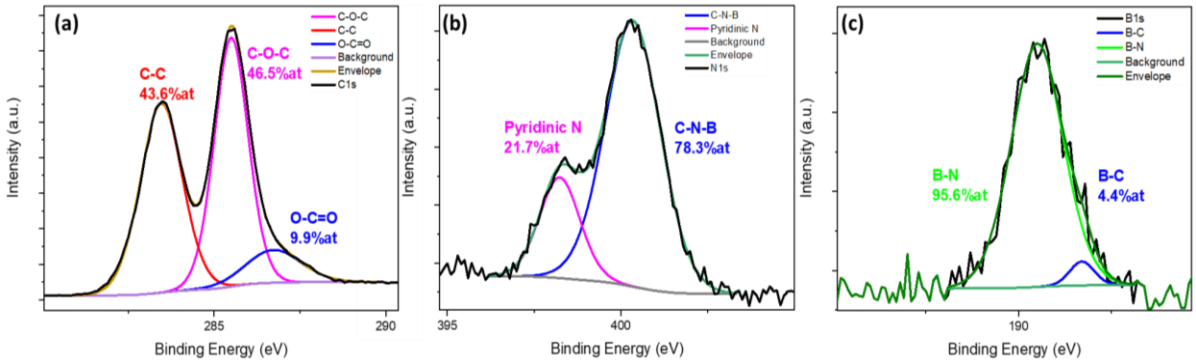

Figure 33 - XPS analysis of (a) C1s, (b) N1s, and (c) B1s peaks of the "new" gel. Reused with permission from [151]**. ©2021 Elsevier.**

The stability of the "new" gel was studied over a 1-year period, as presented in Figure 34. The "new" gel shows the degradation of hole mobility and an increase in electron mobility over time. The I_{ON}/I_{OFF} ratio remains ~10^7. The charge carrier mobilities after a 6-month storage were calculated as 8,800±3,500 $cm^2V^{-1}s^{-1}$ and 10,000±2,500 $cm^2V^{-1}s^{-1}$ for holes and electrons, respectively [151]. Interestingly, the Dirac point does not seem to be affected by the exposure to air, as was the case for the "old" gel.

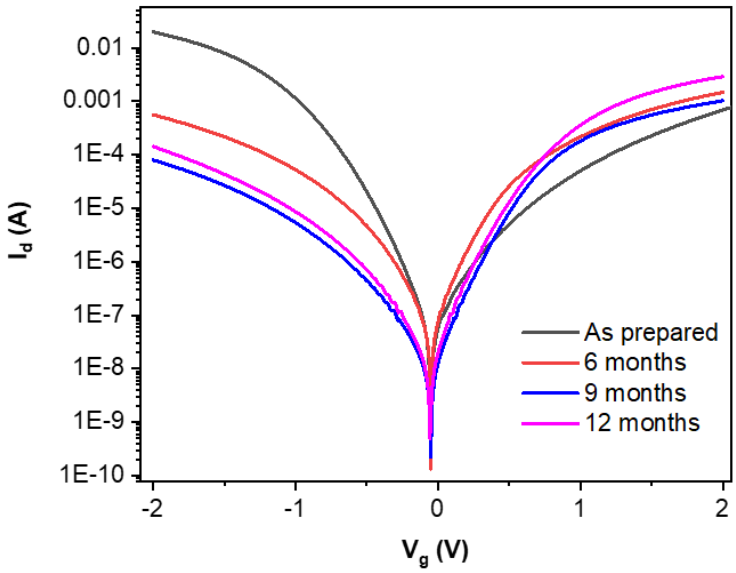

Figure 34 - The air-stability of the "new" S_2 gel over a 1-year period.

4.6.2 Changing the volume fraction in the precursor solution

Figure 30b demonstrated the charge carrier mobility versus the total doping of the BN-GO gel. It was found, that out of the four concentrations used, that of S_2 showed the best mobility values. However, it does not mean that the volume fraction used in the precursor materials (5 vol% h-BN and 95 vol% GO) is the optimal one. Therefore, another gel was fabricated using the same fabrication process discussed earlier for the "new" S_2 gel, but for different volume fractions of the precursor materials, i.e., 10 vol% h-BN and 90 vol% GO. This gel was denoted as $S_{10\%}$.

XPS analysis of the C 1s and the N 1s peaks of the $S_{10\%}$ gel is presented in Figure 35a and b, respectively. The XPS analysis of the C 1s peak in Figure 35a has revealed the same C-C concentration as "new" S_2 gel (46.3 at%), and a slightly higher O-C=O concentration (10.3 at% compared to 9.9 at%). The XPS analysis of peak N 1s in Figure 35b revealed 6.3 at% more Pyridinic N and 3.2 at% Pyrrolic N than in the "new" S_2 gel. The XPS analysis of peak B 1s showed no B-type doping, and all the B atoms stayed connected to nitrogen atoms. A survey spectrum revealed only 0.5 at% of N-doping in the sample.

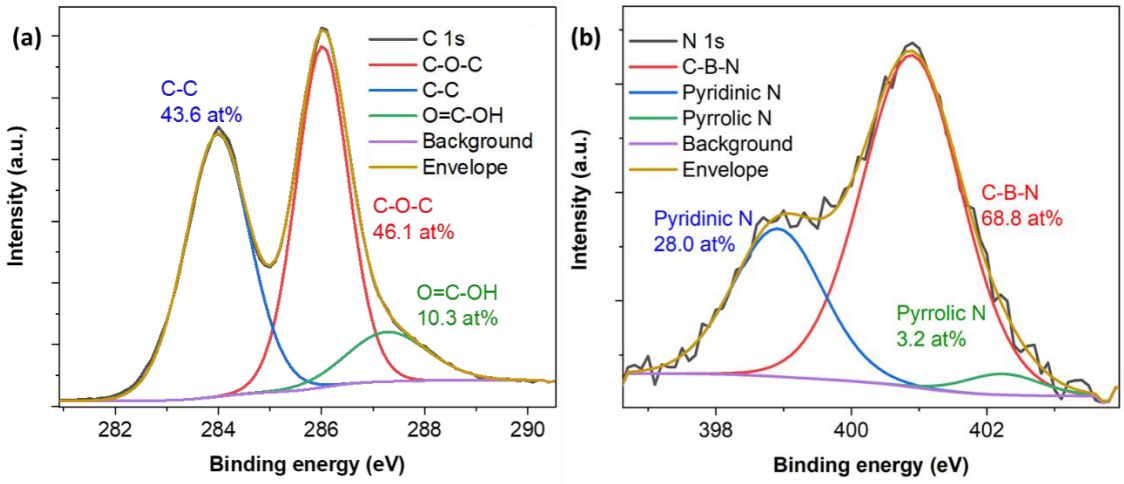

Figure 35 - XPS analysis of the (a) C 1s and (b) N 1s peaks of the $S_{10\%}$ gel.

Since the bonds in the C 1s peak are similar between the "new" S_2 and the $S_{10\%}$ gels, it is hypothesized that the gel formation and the restoration of the C-C bonds are directly related to the intensity of the laser ablation process. This hypothesis should be explored further in future experiments. It is unclear, however, why there was no B doping in the $S_{10\%}$ gel.

The electrical performance of the $S_{10\%}$ gel was studied and compared to the "new" S_2 gel, as seen in Figure 36a. Curiously, the plot for the $S_{10\%}$ gel is different than all the other gels and has much higher hole mobility compared to electron mobility. The major difference between the $S_{10\%}$ gel and the other gels is that there is no B-doping, so further investigation should concentrate on discovering whether this is the reason for the asymmetry. The hole and electron mobilities were calculated as 1500 $cm^2V^{-1}s^{-1}$ and 250 $cm^2V^{-1}s^{-1}$, respectively. The ratio between the ON and OFF currents is also ~10^7.

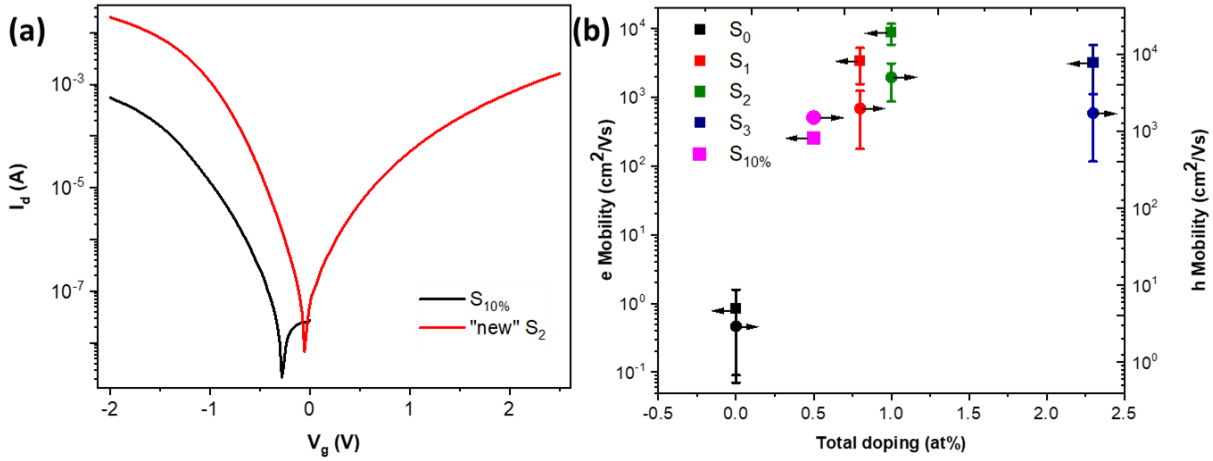

Figure 36 – (a) I_d-V_g plots of the "new" S_2 and the $S_{10\%}$ gels (V_d=-0.05 V). (b) the calculated mobilities vs the total doping (reused with permission from [130]**. ©2019 Elsevier).**

The hole and electron mobilities of the $S_{10\%}$ gel were added to the plot in Figure 30b, as seen in Figure 36b (reused with permission from [130]. ©2019 Elsevier). Although the aim was to produce a gel with a total doping concentration of approximately 1.5 at%, the actual doping concentration was 0.5 at%, and the mobility values are in line with previously reported results.

4.6.3 Decreasing the channel length

Scattering from grain boundaries drastically reduces the mobility of a GFET device [33]. Therefore, devices with longer channels demonstrate reduced charge carrier mobilities [130]. It was hypothesized that reducing the channel length of the gel devices to values below 100 µm would enhance the mobilities further. The same experiment was repeated as described before, but this time a cat's hair was used as the shadow mask since its diameter is lower than 50 µm [153]. The optical microscopy image of the BN-GO gel FET produced using a cat hair shadow mask is demonstrated in Figure 37a. As seen from the image, the channel length is approximately 25 µm, four times shorter than the channels

discussed above. However, the surface of the cat hair is not smooth, resulting in rough edges in the electrodes.

The mobilities of the "new" S_2 and the $S_{10\%}$ gels of the 25-µm-long channels were compared to those of the 100-µm-long channels, as seen in Figure 37b. Contrary to expected, the mobility values were lower for the shorter channels. The unexpected results could be due to high contact resistance caused by the rough edges of the electrodes.

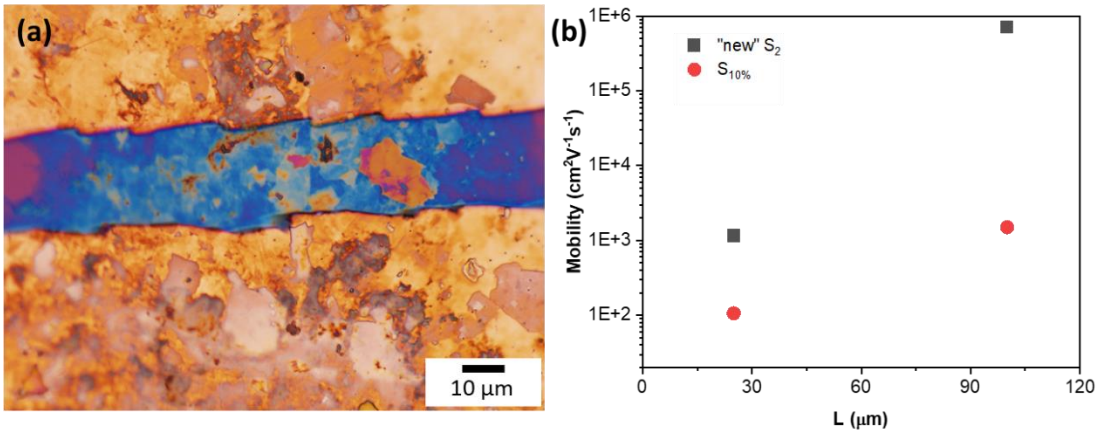

Figure 37 - (a) Optic microscopy image of a bottom-electrode FET with a 25 µm channel length. (b) The mobility dependence on the channel length for two types of gels.

4.6.4 Adding a h-BN buffer layer

Numerous works demonstrated the "substrate-effect" which causes deterioration in the electrical properties of graphene-based materials deposited on a SiO_2/Si substrate [8]. Therefore, one enhancement strategy was to incorporate an h-BN thin layer onto the substrate. In this regard, a 0.1 mL of 1.24 mg/mL h-BN in 50:50 DI water:ethanol was drop-casted onto a SiO_2/Si substrate and let set overnight before the patterning of the source, drain, and gate electrodes. The thickness of the non-contentious h-BN layer was measured using a profilometer (Dektak) as 25±7 nm. A bottom-electrode device with S_2 gel as the channel material was fabricated in the same manner described above, but for the h-BN/SiO_2/Si substrate.

The electrical performance of the S_2 gel FET device with the h-BN/SiO_2/Si substrate was compared to that of the S_2 gel FET device with a SiO_2/Si substrate, as seen in Figure 38. As seen from the figure, the ON and OFF currents, the I_{ON}/I_{OFF} ratio, and the Dirac point do not change between the different devices, while the hole mobility is slightly enhanced for the device with the h-BN/SiO_2/Si substrate, as

seen from the steeper left side of the plot. Interestingly, this device demonstrates a completely symmetrical I_d-V_g plot, which could stem from the fact that the h-BN layer reduces scattering from the dangling bonds present in the SiO_2 [8]. While some improvement is observed, it is unclear whether the extra fabrication step is worth the slight enhancement in mobility.

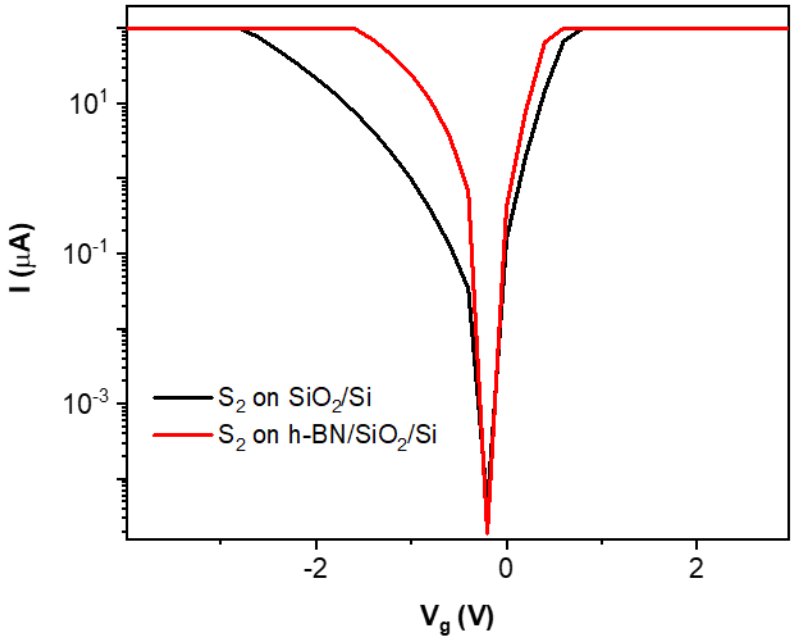

Figure 38 - The I_d-V_g electrical performances of S2 gel FET with an h-BN/SiO_2/Si substrate compared to a SiO_2/Si substrate.

4.7 Summary

In conclusion, the state-of-the-art graphene-based materials demonstrate lower mobility than predicted by theory. The mobility decreases exponentially when increasing the channel length of the device as a direct result of increased charge carrier scattering from the grain boundaries. The BN-GO gels discussed in this chapter were fabricated using a simple laser ablation method that transformed inexpensive insulating 2D materials in a solution into a 3D gel structure. The laser ablation process restored the conjugation and co-doped the gels with boron and nitrogen up to 2.3 at%. An FET with the gel as the top channel demonstrated a charge carrier mobility comparable to short-channel pristine graphene, and an I_{ON}/I_{OFF} ratio 1000 times higher than the state-of-the-art, with a single exception. The improved electrical performance was attributed to the restored conjugation and the reduced number of grain boundaries due to the gel formation.

The gels also demonstrated good stability over a 2-year period and good repeatability. Lastly, the electrical properties of the gels could be further enhanced by controlling the pulse duration during the laser ablation process, reaching the theoretical values of pristine graphene (μ= 440,000 ± 200,000 $cm^2V^{-1}s^{-1}$). Two additional enhancement experiments were performed with an increased volume fraction of h-BN precursor and for reduced channel length, however, fabrication issues reduced the electrical performance. These avenues should be further explored in future experiments. Lastly, an S_2 gel FET device with an h-BN buffer layer between the gel and the SiO_2/Si substrate demonstrated some hole mobility enhancement. The gels could be used in FET devices that require high mobility and a high I_{ON}/I_{OFF} ratio, such as electrical sensors and biosensors.

Chapter 5
GFET heart failure biosensor with enhanced biosensing performance

5.1 Introduction

HF and cardiovascular diseases are the number one cause of death in the world, affecting more than 26 million people per year [154]. While it is possible to detect HF using current protocols, the process is time-consuming and usually involves multiple tests. Considering that HF can be treated and prevented when discovered early, many researchers targeted the fabrication of HF biosensors with faster results and improved LODs. While several groups reported an LOD of 2 fg/mL for an electrochemical biosensor [155] or an LOD of 1 aM for an optical biosensor [156], they take 30-60 min and don't allow real-time monitoring. For these reasons, some groups focused on FETs for HF biosensing, since they are compatible with point-of-care, fast, and sensitive detection [77]. However, the state-of-the-art FETs targeting HF biomarkers show low LODs and narrow detection ranges.

Since the detection capability of an FET biosensor was shown to be directly correlated to the electrical performance (see Chapter 2), it is hypothesized that an FET with enhanced electrical performance would allow improved LOD and longer detection ranges. To test this hypothesis, the "new" S_2 gel discussed in the previous chapter was chosen as the channel material in an FET biosensor targeting BNP, since it had the highest charge carrier mobility compared to the rest of the produced gels. BNP was chosen as the biomarker since it is a well-documented HF biomarker, and its affinity towards the 50E1 antibody was previously reported [6].

This chapter will discuss a proof-of-concept FET biosensor with a BN-GO gel channel targeting BNP, as was reported in [151]. This biosensor offers 4 orders of magnitude improvement in LOD (10 aM) and a long detection range that stretches over 11 orders of magnitude. It also shows good selectivity and specificity and a short detection time of 2 min.

5.2 Fabrication process and equipment

All electrical and biosensing measurements in this chapter were performed using a probe station setup connected to a software-controlled source measure unit (KEYSIGHT B2900A Series). The "new" S_2 gel discussed in Chapter 4 was deposited as a top channel in the same process covered in that chapter. The biosensing experiments were performed 6 months past the fabrication date of the gel. BNP

antibodies (50E1 with pI = 6.6-7.2) were diluted in a pH=7 buffer solution (VWR) to a 1 nM concentration. 5 µL droplets were dropped onto the BN-GO gel channels and left at 4 ˚C for 48 hr, similar to a previously reported method [157].

The immobilization of the antibodies was confirmed by the shift of the Dirac point in the I_d-V_g plot, similar to observations made elsewhere [73]. After immobilization, the Dirac point downshifted by approximately 30 mV, confirming that the antibodies were negatively charged. To confirm a strong immobilization of antibodies, the device went through three consecutive rinsing rounds. In each rinsing round, 10 µL droplets of buffer solution were pipetted on and off the device 5 times.

The BNP biomarker was serially diluted to multiple concentrations (1 aM- 1 µM) in a pH=7 buffer solution. Similarly, K^+ and OH^- solution and HER2 solution in buffer were also diluted to multiple concentrations (1 aM- 1µM) for selectivity experiments. All solutions were mixed for 30 seconds at a setting of 7 using a Vortex mixer (Fisherbrand) for homogeneity.

5.3 Characterization of the biosensor

5.3.1 Antibody immobilization

One of the obstacles in using pristine graphene for FET biosensors is their low chemical reactivity [88], which makes antibody functionalization unfavorable. To overcome this barrier, often a linker is used to physically bind to the graphene through π-π stacking and to covalently bind to the amine groups of the antibody [158]. Nonetheless, the linker increases the bioreceptor size, which is unfavorable for Debye screening considerations [8]. Other groups [132] used the carboxylic groups present in rGO and GO for direct immobilization. However, since the immobilization is directly on the graphene, it is expected to increase the charge scattering and reduce charge carrier mobility.

On this premises, it was hypothesized that the immobilization of the antibodies onto the BN-GO gel could be achieved through the functional groups of the gel, namely the carboxyl functional groups. The XPS analysis of the gel revealed that the C 1s peak is composed of COOH bonds in a concentration of 9.9 at%, much larger than the concentration in the precursor GO (3.5 at%). The increased concentration is a direct result of the laser ablation process [95].

After the channels were covered by the antibody solution for 48 hr at 4˚C, a large change in the I_d-V_g plots was observed, as seen in Figure 39a (reused with permission from [151]. ©2021 Elsevier). First, the Dirac point shifted by ~-30 mV, confirming the attachment of the negatively charged

antibodies. “Second, a large change in the ON and OFF currents was observed after immobilization of antibodies, suggesting the attachment was through covalent bonds, since this type of attachment tends to scatter charges and decrease the current of GFETs. Lastly, an additional minimum point appeared at V_g~0 V, further confirming the attachment of the charged antibodies” [151].

The biosensing in GFET is monitored through the shift in the Dirac point or through the change in current when the biomarker is added to the device. Therefore, the buffer should have a minimal effect over the I_d-V_g plot of the device. To test the buffer effect over the device, a 3 µL buffer was dropped onto the antibody-functionalized and non-functionalized gels, as seen in Figure 39a and b, respectively (reused with permission from [151]. ©2021 Elsevier). As seen from the figures, the buffer solution had almost no effect over the I_d-V_g plots. This means that any Dirac shift or current change resulting from the addition of a BNP solution in buffer would be solely from the BNP.

Next, the nature of the antibody functionalization was tested by subjecting the device to three consecutive rinsing cycles. The I_d-V_g was plotted after antibody functionalization, and after one and three rounds of rinsing, as seen in Figure 39c (reused with permission from [151]. ©2021 Elsevier). The minimal change to the plots confirmed that the antibodies had attached through covalent bonds because physical bonds can be easily detached by rinsing the device in buffer [159].

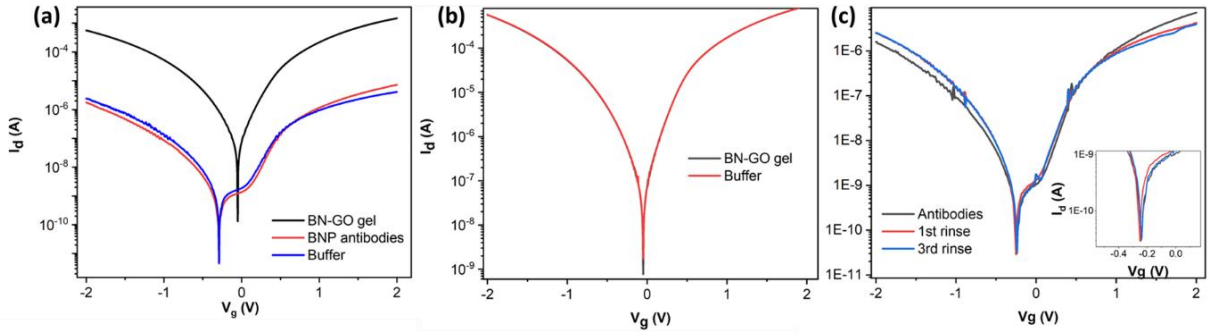

Figure 39 - The change in the I_d-V_g plots of BN-GO gel FET after (a) antibody-immobilization and buffer solution deposition and (b) buffer solution deposition. (c) The change in Id-Vg plots after one and three washing cycles (the inset is an enlargement of the plot). Reused with permission from [151]**. ©2021 Elsevier**

5.3.2 Real-time biosensing

Point-of-care applications favor biosensors that offer real-time monitoring [7] which is one of the advantages that FET biosensors offer. The real-time BNP biosensing was monitored through the change

in the device's current (for constant drain and back gate voltages of -0.05 V and -0.6 V, respectively) as a response to the addition of increasing concentrations of BNP in pH=7 buffer. Specifically, a 2.5 µL droplet of BNP solution with increasing concentrations was dropped onto the antibody-functionalized BN-GO gel channel approximately every 50 seconds.

As seen from Figure 40a, the real-time biosensing is not reliable for low BNP concentrations. While there is some change in current in response to the addition of BNP solution, even for concentrations as low as 10 aM, the current is unstable. This instability may stem from the fact that the high currents (~100 µA) contribute to joule heating [160]. On the other hand, when looking at higher concentrations of BNP solution (Figure 40b), the current is more stable. The detection time is as low as 5 seconds, but the LOD and detection range is very low (10 fM and 10 fM-1 pM, respectively).

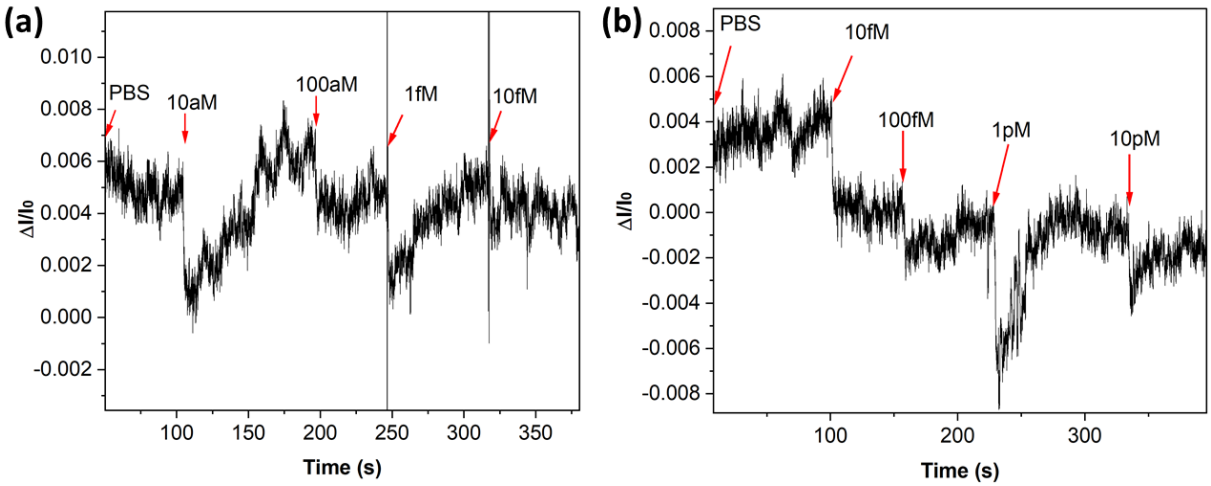

Figure 40 - Real-time BNP biosensing results. Figure (b) was reused with permission from [151]**. ©2021 Elsevier**

The selectivity of the biosensor was measured against a solution containing different concentrations of K^+ OH^- ions. The biosensing experiment was performed in the same manner, but for increasing concentrations of K^+ OH^- ions instead of BNP. These ions were chosen since they are small charged ions present in blood [161]. It was found that the biosensor's current changed by ~3 nA in response to K^+ OH^- ions with 1 fM- 1 µM concentration range. This current change is within the error range of the measurement [151]. Biosensing performance can be compared using a sensitivity parameter, defined as the biosensing response divided by the initial value (the current for the buffer). In real-time biosensing, it is defined using equation 7:

$$Sensitivity\ (\%) = (100\%)\ \mathrm{x}\ \frac{I_{response} - I_{buffer}}{I_{buffer}} \qquad (7)$$

In the case of BNP, the sensitivity for 10 fM was found to be ~0.4%, while the sensitivity for 1 μM K^+ OH^- was calculated as 0.01%. Meaning, that real-time detection of BNP is 40 times more sensitive compared to high concentrations of K^+ OH^-.

5.3.3 Biosensing through Dirac point monitoring

Graphene is a unique material that has symmetrical electron and hole conductance curves [57]. Therefore, it allows a different type of biosensing than conventional FETs, i.e., the monitoring of the Dirac point. For the Dirac point change monitoring, a 2.5 μL droplet of BNP solution with increasing concentrations was dropped onto the channel, and the I_d-V_g (at a constant drain voltage of -0.05V) was plotted after a 2-minute incubation period. Between measurements, the channel was rinsed with buffer solution, and the measurement was repeated with a higher concentration of BNP. The Dirac point of the buffer solution was taken as the reference.

Figure 41a (adopted with permission from [151]) shows the Dirac shift response to increasing BNP concentration introduced to the antibody-functionalized channel. As seen from the figure, the Dirac point of the buffer solution was at -0.3 V. The Dirac point shifted to higher voltages for increasing concentrations of BNP in buffer. The lowest shift of approximately 25 mV was observed for 10 aM BNP, so this concentration was determined as the LOD of the biosensor.

To determine the detection range that the biosensor offers, it is customary to plot the biosensing response versus the logarithmic value of the biomarker concentration [162]. The detection range is determined as the range of biomarker concentration for which the biosensing response has a linear dependence. From Figure 41b (adapted with permission from [151]) it was found that the detection range of this biosensor stretches over 11 orders of magnitude, i.e., 10 aM-1 μM, with an R-square value of 0.936. The incredible LOD and long detection ranges are expected to be a direct result of the high charge carrier mobility and I_{ON}/I_{OFF} ratio of the BN-GO gel FET. However, none of this would be possible unless the Debye layer was increased, since the expected Debye layer for the buffer used is ~1 nm, and the length of the antibody is ~10 nm [61].

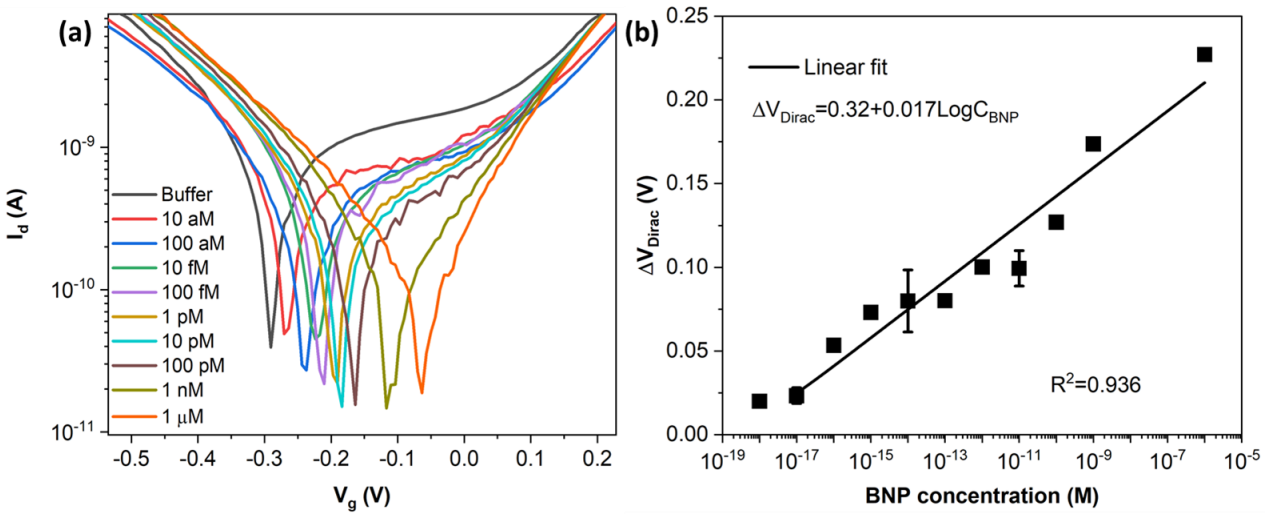

Figure 41 – (a) BNP biosensing through Dirac point monitoring of a BN-GO gel FET biosensor. (b) The detection range of the biosensor. Adapted with permission from [151]**.**

The increase in the Debye screening length is expected to stem from several reasons. First, the 3D structure of the BN-GO gel is a non-flat structure [151], and it was previously reported [7] that curved structures could be used to increase the Debye screening length. Second, it is expected that the 3D structure has some pores [131], and it has been shown that permeable layers increase the Debye screening length [64].

The biosensing performance was compared to all state-of-the-art FET biosensors targeting HF biomarkers [151]. The best biosensing performance was achieved by Lei et al. [73] who reported an LOD of 100 fM for an rGO/Pt NPs hybrid. Alas, their detection range was 100 fM- 1 nM in buffer and 50-200 nM in blood, and their detection time was 30 min. In comparison, the biosensor discussed here has a x10000 times improved LOD and a much larger detection range. In addition, it has a very short detection time of 2 min.

In Chapter 2, the LOD and the detection range for the state-of-the-art GFET biosensors targeting small proteins were plotted against the charge carrier mobility of the GFET (Figure 6 a and b, respectively). Extrapolating the trends of these plots, it was found that the LOD and detection range would be 1 aM and 8 orders of magnitude, respectively, for a GFET with a mobility of 10^5 $cm^2V^{-1}s^{-1}$. The BNP biosensor used in this work was added to the two plots in Figure 6, as presented in Figure 42. As seen from Figure 42a, the result achieved in this thesis is in line with other reported protein biosensors.

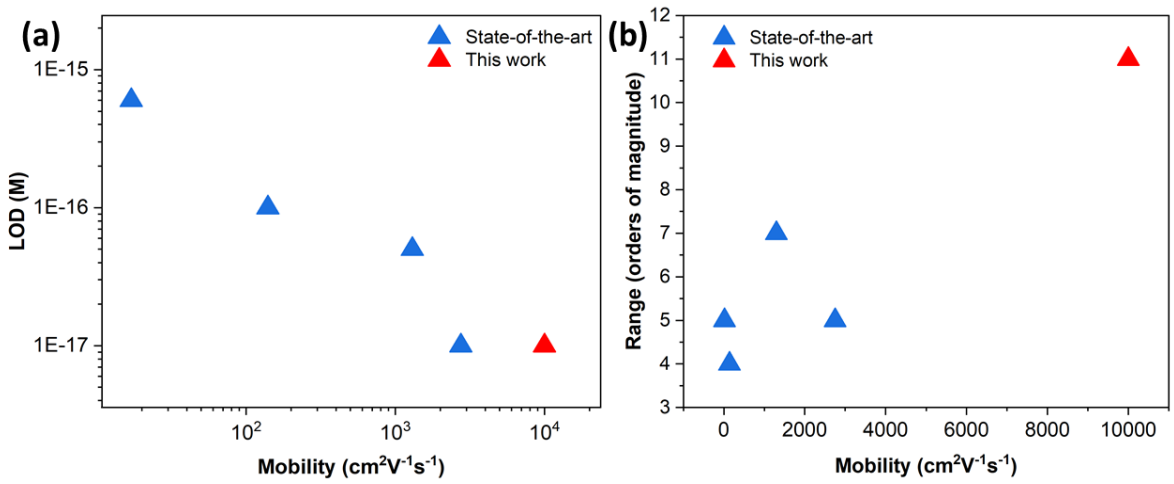

Figure 42 - The (a) LOD and (b) detection range vs the charge carrier mobility of the BN-GO gel FET BNP biosensor compared with the state-of-the-art GFET biosensors targeting small proteins.

Since no blocking agent was used to block any biomarker from attaching directly to the BN-GO gel, specificity experiments were also performed. For this purpose, 2.5 µL of BNP solution with increasing concentrations was dropped onto the bare BN-GO channel, and a drain current vs gate voltage plot was obtained after 2 minutes. The biosensing response was monitored by the Dirac point change in response to increasing BNP concentrations. The Dirac point had not shifted when the BNP was introduced to the channel up to a concentration of 1 nM. It was also found that the ON and OFF currents were not affected by the addition of the BNP. It is hypothesized that the BNP, which is a small positively charged molecule, needs more time to attach to the channel. It is suggested to examine this point in future experiments.

The selectivity of the BNP biosensor was measured against HER2 [151]. The Dirac point shifted by 3 mV in response to 1 ng/mL HER2 and did not shift further for an additional 1 µg/mL, a concentration 70 times higher than the normal level in blood. The 3 mV shift is within the noise range. The sensitivity of both devices was calculated using equation 8:

$$Sensitivity\ (\%) = (100\%)\ \mathrm{x}\ \frac{V_{Dirac_{response}} - V_{Dirac_{buffer}}}{V_{Dirac_{buffer}}} \qquad (8)$$

The sensitivity in equation 8 is the shift in Dirac voltage for the addition of biomarker from that of the buffer, divided by the Dirac voltage when only a buffer is present. The sensitivity for 1 ng/mL

HER2 was calculated as 1.1 % while the sensitivity for the 10 aM BNP (the biosensor's LOD) was almost 10 times higher (10%).

5.4 Future work

While the biosensing results achieved for the BN-GO gel FET targeting BNP are impressive, they were attained for a small number of devices (6 in total). It is therefore advised to perform more experiments to measure the repeatability and stability of the device. Second, several samples did not have antibody functionalization, even though the functionalization process was the same for all samples (these samples were not included in this work). Thus, it is advisable to find a functionalization process that would enhance the reaction between the amine groups in the antibodies and the carboxyl groups in the BN-GO gel. One suggestion may be to shake the device during the incubation process.

The selectivity of the device was only measured against HER2 protein and K^+ OH^- ions. However, real samples are much more complex and could have many interfering molecules [19]. So, it is suggested to measure the device's selectivity against a larger number of charged biomolecules or using a more complex medium, such as blood. In addition, the measurements should be repeated with a blocking agent that would reduce any unwanted reactions with the BN-GO gel [132]. Lastly, a further improvement in sensitivity may be achieved by replacing antibodies with aptamers.

5.5 Summary

In conclusion, a BN-GO gel FET covalently functionalized with BNP antibodies was tested as a BNP biosensor in a pH=7 buffer solution. Real-time measurements were able to give a detection in as little as 5 seconds, however, had a high LOD of 10 fM and a low detection range of 10 fM – 1 pM. The selectivity of the device was measured against K^+ OH^- ions, demonstrating 40 times higher sensitivity towards BNP. The biosensor was also monitored through changes to the Dirac point in response to the addition of BNP in buffer. The biosensor was able to detect BNP with an LOD of 10 aM within 2 minutes. It also had a superior detection range stretching over 11 orders of magnitude (10 aM – 1 μM). The biosensor showed minimal response towards non-specific interactions, and 10 times improved selectivity towards BNP than HER2. While these results show a great improvement compared with the state-of-the-art FET biosensors targeting BNP, it is meant here only as a proof of concept, and future experiments should target detection in more complex matrices.

Chapter 6
Other sensors using BN-GO gels

6.1 Introduction

Graphene and graphene-based materials have been studied as the transducer materials in FET biosensors targeting a large array of biomarkers [7], [70] , as was discussed in Chapter 2. In addition, they were also used in many other sensing and biosensing platforms including gas sensors [163], and optical and electrochemical sensors and biosensors [164]. Gas sensors could be used for environmental monitoring [163] or for disease diagnosis, in the form of a breathalyzer [165]. Graphene-based materials are attractive for gas sensing since they have a high surface area and can be easily functionalized to adsorb gases [163]. They are attractive for electrochemical biosensing platforms because of their high electrocatalytic activity [164]. In optical biosensors such as surface plasmon resonance, they are useful for signal enhancement.

This chapter will discuss the BN-GO gel in a gas sensor published in [165]. The sensor type is categorized as a piezoresistive nanomechanical membrane-type surface stress sensor (MSS). This sensor was tested against different types of volatile organic compounds (VOCs). VOCs in breath were associated with diseases such as diabetes, liver and lung disorders, and some cancers. In addition, efforts in using the BN-GO gel FET discussed in Chapter 5 as a COVID-19 biosensor would also be covered. The biosensing medium was studied, and it was found that a pH=7 buffer gives an LOD of 10 fg/mL with a narrow detection range of 10 fg/mL-1 pg/mL. However, unlike the PCR methods used in clinical tests of COVID-19 [77], this biosensor gives an almost immediate detection, thus attractive for further development.

6.2 BN-GO gel receptors in an MSS VOC sensor

6.2.1 Background and experimental

The working principle of the MSS sensor was reported elsewhere [166]. In short, a circular membrane with a 0.3 mm diameter coated with 300 pL of the BN-GO gels by an inkjet sputtering system is subjected to different VOCs. The gases penetrate the thin gel film and adsorb onto the active adsorption sites and induce the film to “swell”. Consequently, the membrane deflects which strains the four piezoresistors connected to it, resulting in voltage change (measured by Wheatstone bridge circuit).

The data were recorded at the bridge voltage of −0.5 V and a sampling rate of 10 Hz. Unlike the FET biosensor in Chapter 5, the gels served as the receptor rather than the transducer materials.

Nitrogen gas was bubbled into the analytes to produce vapors which were carried into an enclosed environment containing the sensor. The analytes included water, ethanol, hexanol, hexanal, heptane, methylcyclohexane, toluene, ethyl acetate, and acetone. Each analyte was tested for 10 ON/OFF cycles of 10 seconds each for varying vapor pressures of 2%, 5%, and 10%.

The motivation behind using graphene-based materials in gas sensors is due to their large surface area [163]. However, since pristine graphene is a chemically inert material, it needs to be functionalized or doped to increase its chemical reactivity. Nonetheless, it was shown that some functionalization and doping reduces the conductivity of graphene [73], [47] which would reduce the signal and the sensitivity of a resistive sensor. The MSS structure circumvents this problem [165], and the BN-GO gel has been shown to have good chemical reactivity [130]. Since chemical reactivity is very important in the receptor material, only S_2 and S_3 gels were used in these experiments.

6.2.2 Results and discussion

Table 13 - The estimated sensitivities in μV/ppm for S_2 and S_3 gels MSS for different VOCs (dapted with permission from [165]**. ©2020 Wiley).**

Analyte	S_2 gel	S_3 gel
Water	0.49±0.01	0.53±0.01
Ethanol	0.01±0.03	0.1±0.03
Hexanol	14.49±0.01	16.85±0.01
Hexanal	0.079±0.01	0.75±0.02
Heptane	0.02±0.01	0.16±0.04
Methylcyclohexane	0.38±0.01	0.36±0.06
Toluene	0.82±0.01	0.82±0.02
Ethyl Acetate	0.14±0.05	0.16±0.01
Acetone	0.04±0.02	0.05±0.02

The estimated sensitivities for S_2 and S_3 gels MSS for different VOCs are summarized in Table 13 (adapted with permission from [165]. ©2020 Wiley). As seen from the table, the sensitivity of the sensor is enhanced when using an S_3 receptor compared with the S_2 receptor for all analytes with two exceptions. The enhanced sensitivity of the S_3 gel is contributed to the increased concentration of boron [167] and nitrogen [168] atoms compared with the S_2 gel, as discussed in Chapter 4. The largest effect on the sensitivity was observed for Ethanol, where the sensitivity increased from 0.01±0.03 μV/ppm to 0.1±0.03 μV/ppm. Similarly, Hexanal also showed a great improvement in sensitivity from 0.079±0.01 μV/ppm to 0.75±0.02 μV/ppm. The lowest effect on the sensitivity was observed for Toluene, where it stayed constant at ~0.82 μV/ppm.

The LOD was calculated and compared with different 2D materials receptors, such as GO gel, MoS_2, and WS_2. It was found that the S_3 gel enhances the LOD for water (0.084 ppm) by 3-11 times and the LOD for Hexanol (0.001 ppm) by 7-52 times compared to the other receptors. The LOD for Heptane, Ethyl Acetate, and Acetone were also enhanced for S_3 gel compared with the other receptor types tested. For Heptane, the LOD was 0.091 ppm with an enhancement of 1-2 times. For Ethyl Acetate, the LOD was 0.16 ppm with an enhancement of 7-30 times. Lastly, the LOD of Acetone (1.24 ppm) was enhanced by 2-8 times. Interestingly, for Toluene and Hexanal, the best LOD was observed for the S_2 gel (0.028 ppm and 0.032 ppm, respectively). With a single exception being Ethanol, the LODs were enhanced for all VOCs when either S_2 or S_3 gels were used as the receptors.

6.2.3 Summary

In conclusion, BN-GO gels were used as the receptor materials in an MSS sensor targeting a large array of gases including VOC gases. The sensitivity and the LOD of these sensors were tested for each gas and compared to other receptors consisting of 2D materials. It was found that the sensitivity of the sensor is enhanced for S_3 gel compared with S_2 gel, most likely due to its higher boron and nitrogen concentrations and improved chemical reactivity. In addition, it was found that sensors using BN-GO gels as the receptor material had improved LODs compared with other 2D materials receptors such as GO gel, MoS_2, and WS_2. Overall, the BN-GO MSS sensor showed the lowest LOD of 0.001 ppm and the highest sensitivity of 16.85±0.01 μV/ppm for Hexanol. This work demonstrates the ability of the BN-GO gels to be used as receptor materials in gas sensor applications.

6.3 BN-GO gel FET COVID-19 biosensor

6.3.1 Introduction

In the past year, a virus has been the focus of many different biosensing platforms. This is the coronavirus 2 (SARS-CoV-2) which causes the COVID-19 which became vastly studied, especially since the World Health Organization (WHO) has classified the COVID-19 outbreak as a pandemic [77]. GFET is one of the solutions researchers target for highly sensitive point-of-care biosensor applications. In April 2020, Seo et al. [77] reported a GFET biosensing device for detecting SARS-CoV-2 in clinical samples. The channel was CVD-grown graphene functionalized with a specific antibody against SARS-CoV-2 spike protein through a PBASE linker. They reported an LOD of 1 fg/mL in phosphate-buffered saline and 100 fg/mL in clinical transport medium. The selectivity of the biosensor was tested against Middle East respiratory syndrome coronavirus (MERS-CoV) with 6 times higher detection signal towards the target. Lastly, the detection range stretched over 3 orders of magnitude. The charge carrier mobility and the I_{ON}/I_{OFF} ratio were calculated as ~125 $cm^2V^{-1}s^{-1}$ and 1.5, respectively.

Considering that the BN-GO gel FETs discussed in this thesis demonstrate considerably improved electrical performance than that reported by Seo et al. [77], the COVID-19 biosensing performance could be improved. On this premises, a series of experiments targeting the detection of a synthetic SARS-CoV-2 spike protein in different buffer mediums with a "new" S_2 gel FET were executed. The incubation period with the corresponding antibody solution was also tested, as well as different channel lengths and substrate.

6.3.2 Experimental

All electrical and biosensing measurements in this sub-section were performed using a probe station setup connected to a software-controlled source measure unit (KEYSIGHT B2900A Series). The "new" S_2 gel discussed in Chapter 4 was deposited as a top channel in the same process covered in that chapter. The biosensing experiments were performed 9-12 months past the fabrication date of the gel. SARS-CoV-2 (2019-nCoV) nucleoprotein antibodies (recombinant monoclonal antibody expressed from HEK293 cells of rabbits) were purchased from Sino Biological (~50 kDa) and diluted in a pH=7 buffer solution or 0.1x phosphate-buffered saline (PBS; pH 7.4) to a 10 µg/mL concentration. 5 µL droplets were dropped onto the BN-GO channels and left at 4 ˚C for 24, 48, or 72 hours, similar to a previously

reported method [157]. A single sample was also incubated for 24 hr in 3 µL of 10 mM ethanolamine solution at 4 ˚C.

The immobilization of the antibodies was confirmed by the shift of the Dirac point in the I_d-V_g plot, similar to observations made elsewhere [73]. To confirm a strong immobilization of antibodies, one device went through seven consecutive rinsing rounds. In each rinsing round, 10 µL droplets of buffer solution were pipetted on and off the device 5 times.

The COVID-19 biomarker was serially diluted to multiple concentrations (1 ag/mL- 1 µg/mL) in a buffer solution (1x and 0.1x pH=7 buffer or 0.1x and 0.01x PBS). All solutions were mixed by pipetting 100 µL of the solution in and out of the vials 10 times each. 3 µL of COVID-19 solution was dropped onto the channel and an I_d-V_g curve was plotted every minute for 3-5 times. Then, the device was continuously rinsed by the buffer solution, and another COVID-19 solution with an increased concentration was dropped on top, and so on until reaching the most concentrated solution.

6.3.3 Results and discussion

6.3.3.1 Antibody immobilization and incubation times

The BN-GO gel channel incubation time in the antibody solution was studied to find optimal incubation times. For a pH=7 buffer (VWR) two samples were incubated for 24 hours in the antibody solution at 4 ˚C, while two other samples were incubated for 48 hours at the same conditions. It was found that incubation for 24 hr is not enough for functionalization with only one of the samples demonstrating some functionalization, while the 48 hr incubation time gave a 100 % success rate in antibody functionalization, as seen in Figure 43c-d and a-b, respectively. The sample in Figure 43a (denoted as 100_10.1) demonstrated a large reduction in the ON current (from ~100 µA to ~1 µA) and approximately a -30 mV shift in the Dirac point, all consistent with antibody functionalization [73]. Similarly, the sample in Figure 43b (denoted as 100_9.1) demonstrated a reduction in the ON current (from ~100 µA to ~10 µA) and approximately a -30 mV shift in the Dirac point. In contrast, the samples in Figure 43c and d showed no Dirac point shift, while the sample in Figure 43d showed some decrease in the charge carrier mobility, confirming some attachment of antibodies to the channel.

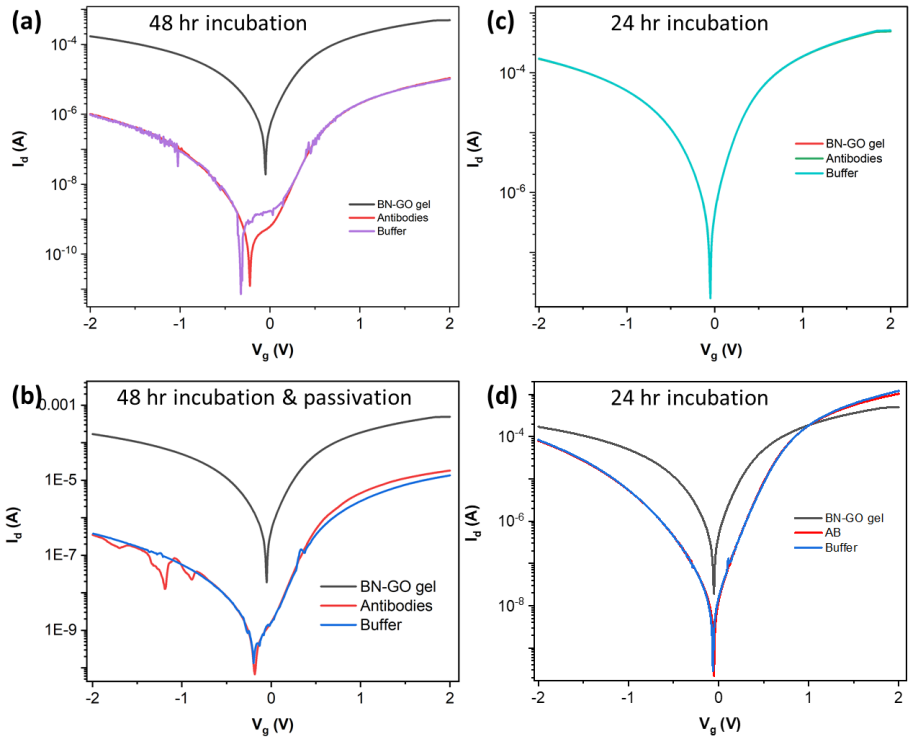

Figure 43 - Antibody functionalization for (a)-(b) 48 hr and (c)-(d) 24 hr incubation time, as seen from the change in the I_d-V_g plots. The antibodies were in a pH=7 buffer solution.

After antibody immobilization measurements, 3 µL of pH=7 buffer solution was dropped onto the channel and the I_d-V_g was plotted after 3 minutes. The results are seen in Figure 43a-d. As seen from the figures, the buffer solution had no effect over the unfunctionalized sample, and little effect over the slightly functionalized sample in Figure 43c and d, respectively. The Dirac point in Figure 43a shifted by approximately -55 mV when the sample was introduced with buffer, while the passivated sample in Figure 43b shifted by only -12 mV.

To test the functionalization strength of the antibodies to the BN-GO gel channel, the same sample went through seven washing cycles [151], as demonstrated in Figure 44. As seen from the figure, the buffer had a slight effect over the Dirac point, which downshifted by 26 mV. After the first four washing cycles, the Dirac point stayed approximately unchanged, but after the fifth washing cycle, the Dirac point upshifted by ~200 mV, indicating detachment of the antibodies. Since the antibodies were only detached from the channel after vigorous rinsing, it is deduced that their attachment was through covalent bonds via the amine groups in the antibodies and the carboxyl groups in the BN-GO gel [151].

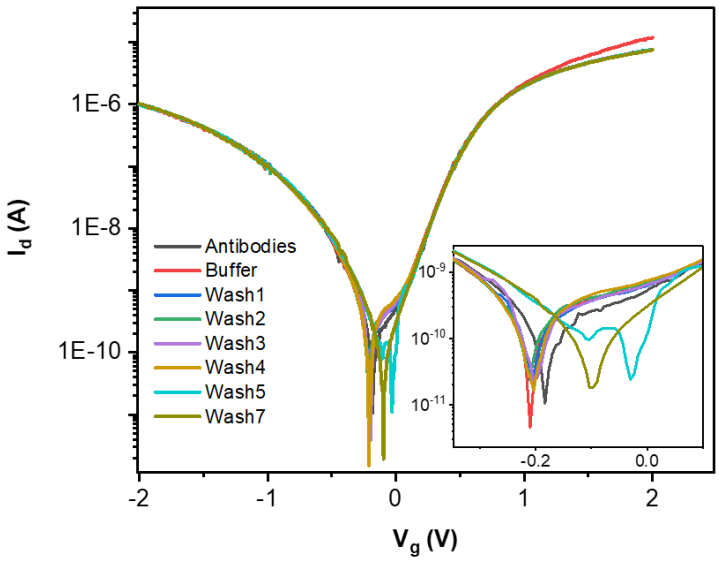

Figure 44 - Antibody attachment strength monitored by the I_d-V_g plots after seven consecutive washing cycles. The inset is an enlargement of the Dirac points.

Five additional samples were incubated in 5 µL of antibodies in 0.1x PBS solution (10 µg/mL) at 4 ˚C for 72 hours. One of the samples was the S_1 gel sample that was measured after two years (Chapter 4, section 4.5). Another sample used an h-BN/SiO_2/Si substrate, as discussed in chapter 4. Out of the five samples, three demonstrated the characteristic I_d-V_g plot changes confirming the antibody functionalization, so the success rate was determined as 60 %. The devices that demonstrated the characteristic changes in the I_d-V_g plot in response to the antibody functionalization are presented in Figure 45. In Figure 45a, a "new" S_2 gel FET device was used, and the Dirac point downshifted by ~65 mV in response to the antibody functionalization. Similarly, in Figure 45b the same gel was used but there was an additional h-BN buffer layer between the gel and the substrate. The Dirac point downshifted by ~260 mV in response to the antibody functionalization. Lastly, in Figure 45c, a two-year-old S_1 gel FET device was used, and the Dirac point downshifted by ~300 mV in response to the antibody functionalization.

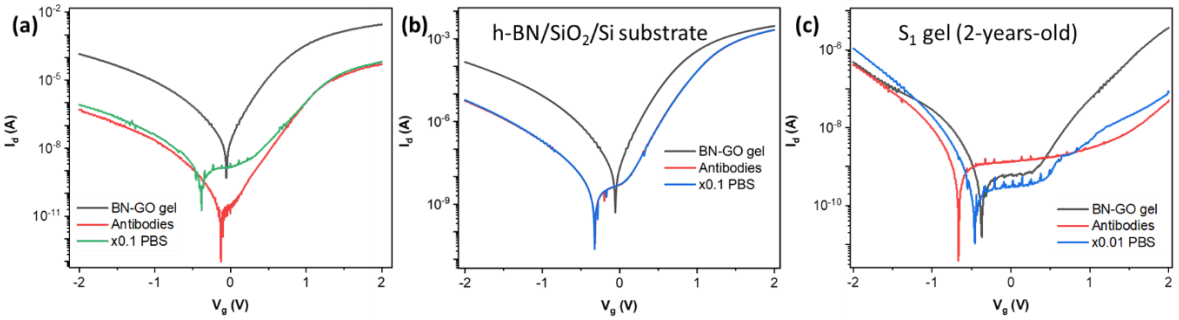

Figure 45 - Antibody functionalization for 72 hr incubation time, as seen from the change in the I_d-V_g plots. "New" S_2 gel on (a) a SiO_2/Si substrate and (b) an h-BN/SiO_2/Si substrate. (c) A two-year-old S_1 gel FET. The antibodies were in a 0.1x PBS buffer solution.

PBS was deposited onto the channels and the I_d-V_g curves were plotted after a 2-minute incubation time. The devices in Figure 45a and c showed a large shift in the Dirac point as a result of the 0.1x and 0.01x PBS addition, respectively, while the I_d-V_g plot in Figure 45b demonstrated minimal reaction to the addition of 0.1x PBS. It is unfavorable for the device to have a Dirac point shift response to the buffer solution since the device is expected to only react to the analyte. The use of a PBS buffer is therefore unfavorable for the BN-GO gel FET COVID-19 biosensor.

6.3.3.2 COVID-19 biosensing results

This sub-section will present all the COVID-19 biosensing results achieved by the different BN-GO gel FET configurations. The results would be divided by the biosensing medium, i.e., the 1x and 0.1x pH=7 buffer and the 0.1x and 0.01x PBS. As was discussed earlier, out of the four devices tested using the 1x pH=7 buffer, two devices demonstrated antibody functionalization and another device demonstrated partial functionalization. These three devices, however, showed no Dirac shift in response to the addition of COVID-19 up to a concentration of 100 ng/mL, as seen from Figure 46a-b. The inability to sense the COVID-19 protein could stem from one of two reasons. The first is that the antibody-protein pair is incompatible, and the second is that the protein capture is beyond the Debye screening length [7].

Two experiments were performed to discover which of the two is the culprit. The first experiment was performed by Dr. D. Eleftherios' lab in Mt. Sinai Hospital, where they performed an enzyme-linked immuno-sorbent assay (ELISA) test to measure the reaction between the antibody and the COVID-19 protein used in this work [169]. It was found that compared to two other non-specific antibodies from a mouse source (purchased from PT and Abcam), the signal for 1-100 ng of the

COVID-19 protein and antibody pair used in this work was 2-400 times larger (depending on the COVID-19 amount). Thus, the antibody-protein pair was confirmed as specific.

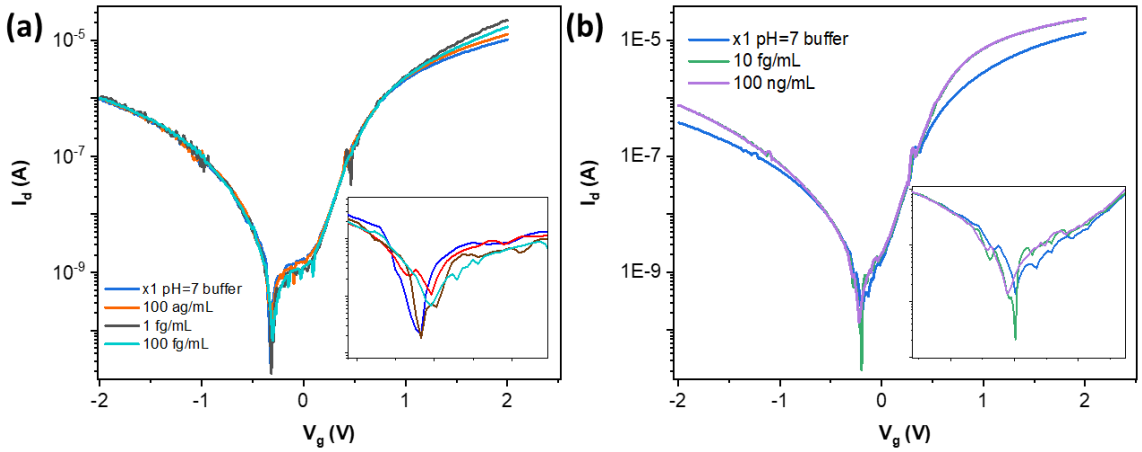

Figure 46 - COVID-19 biosensing in 1x pH=7 buffer by BN-GO gel FET, as observed from the Dirac point monitoring of the I_d-V_g plots. The insets are enlargements of the Dirac points.

In the second experiment, the 1x pH=7 buffer was diluted with DI water to a 0.1x concentration. The dilution was performed in order to reduce the ionic strength of the solution which in turn, increases the Debye screening length [63]. The same two samples (100_9.1 and 100_10.1 stored at 4 ˚C) were washed with the diluted buffer and measured one month later using COVID-19 solutions in 0.1x pH=7 buffer. The Dirac point monitoring of the biosensor as a response to increasing concentrations of COVID-19 protein for sample 100_10.1 (one month after antibody functionalization) is presented in Figure 47a.

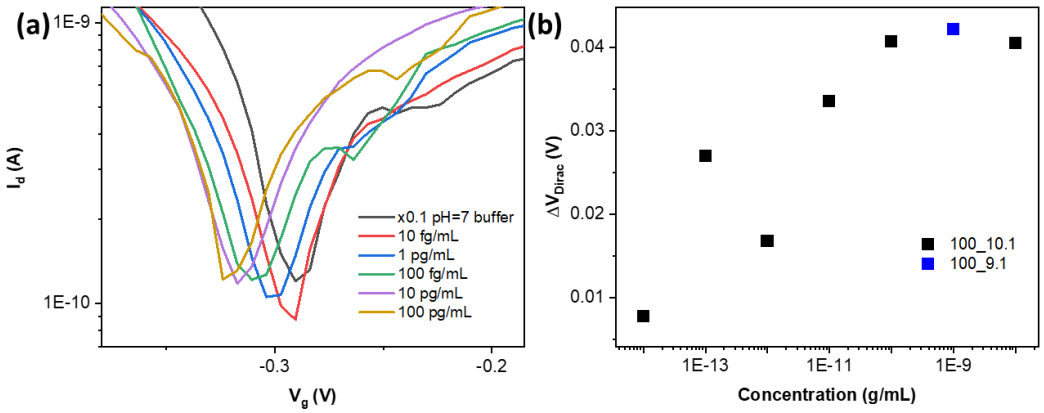

Figure 47 - (a) The Dirac point monitoring of the biosensor as a response to increasing concentrations of COVID-19 protein for sample 100_10.1 one month after fabrication. (b) The shift in Dirac point for different COVID-19 protein concentrations.

The Dirac point of the buffer solution was taken as the reference point, and any additional shift caused by the introduction of COVID-19 protein in buffer is caused by the protein's charge. The shift in the Dirac point in response to increasing concentrations of the COVID-19 protein is presented in Figure 47b. As seen from the figure, the LOD is observed at ~30 fg/mL, as calculated by three times the measurement noise [7]. The detection range is 0.01-100 pg/mL, as observed from the approximately linear region in Figure 47b. Beyond 100 pg/mL the detection signal (Dirac point shift) saturates. These results are encouraging for further investigation since the devices were a month-old and used.

PBS is a recognized buffer solution [7], so the next set of experiments was performed using 0.1x and 0.01x PBS solutions. The biosensing results are presented in Figure 48. The Dirac shift results for all PBS solutions were unstable, so the shift was calculated as the average shift of 2-3 measurements after a 2-4 minute incubation. In Figure 48a, the limit of detection was calculated as ~3 fg/mL (as three times the noise [7]). However, the detection range was only 3-100 fg/mL. In contrast, the biosensing results for 0.01x PBS buffer presented in Figure 48b were observed for concentrations as little as 10 ag/mL, but the shift was unreliable and within ~1.5 times the noise. In addition, the I_d-V_g plots were highly unstable and unreliable. It is thus deduced that either the PBS buffer is incompatible or that a passivation layer should be used.

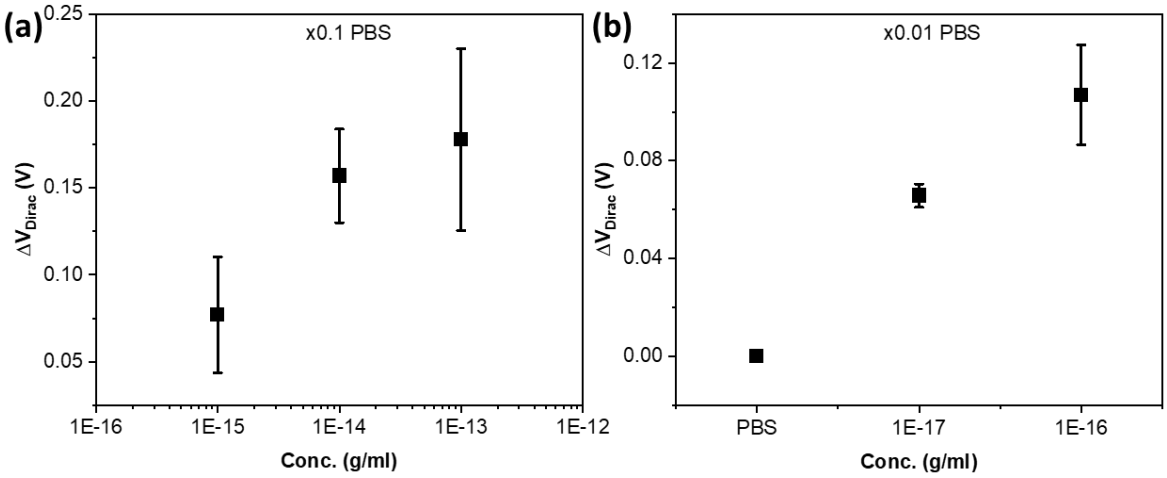

Figure 48 - Dirac point shift in response to the increasing concentrations of COVID-19 protein in (a) 0.1x and (b) 0.01x PBS buffer.

The sample using the h-BN buffer layer demonstrated a very small Dirac shift in response to the addition of 1, 10, and 100 pg/mL of 4±3 mV, 10±5 mV, and 13 mV, respectively. These results are within the 3x(noise) range, and therefore are unreliable. The stabling effect of the h-BN over the

graphene [17] might also be responsible for the small Dirac shifts in response to the COVID-19 protein, but this should be further examined.

6.3.4 Summary

In conclusion, a BN-GO gel FET was used for COVID-19 biosensing in buffer as a proof-of-concept. The sensor demonstrated the best antibody attachment results after 48 hours incubation in antibody solution in a 1x pH=7 buffet at 4 ˚C, compared with 0.1x pH=7 and 0.1x and x0.0.1 PBS buffers and different incubation times. The Dirac shift was monitored in response to the addition of COVID-19 protein solutions in different buffers. The best biosensing performance in terms of stability and detection range was observed for 0.1x pH=7 buffer solution, and the LOD and detection range were calculated as ~30 fg/mL and 0.01-100 pg/mL, respectively. Further investigation should target the repeatability and selectivity of the biosensor. A 0.01x pH=7 buffer should also be investigated because it may increase the Debye screening length further and allow for better LOD and detection range. Lastly, the channels should be passivated to decrease the non-specific reactions and Dirac shift caused by the buffer solution.

Chapter 7
Conclusions and future work

7.1 Conclusions

In conclusion, graphene is an attractive material for a multitude of applications due to its 2D structure and theoretical electrical conductance. Nonetheless, the fabrication of pure graphene is costly and challenging for large-area applications. In this work, the state-of-the-art pristine graphene fabricated by CVD, epitaxial growth, and exfoliation were compared based on their room temperature mobilities and I_{ON}/I_{OFF} ratios. Small area (~2 μm^2) exfoliated graphene demonstrated the highest reported charge carrier mobilities, but they were still an order of magnitude lower than theoretical values. Charge carrier mobilities decreased proportionally to increased channel area as a direct result of grain boundary scattering. Additionally, GFETs demonstrated very low I_{ON}/I_{OFF} ratios (<13) which hinders their use in FET applications.

Many graphene-based materials were developed and studied to overcome these issues, with structures ranging from 1D nanoribbons to 3D gels and heterostructures. The electrical performance of the different state-of-the-art graphene-based materials was compared. The highest I_{ON}/I_{OFF} ratios were observed for rGO, and the highest mobilities were observed for heterostructures of graphene and h-BN.

Investigation of several of the state-of-the-art graphene-based FET biosensors revealed that improved electrical performance of the FET device gives lower LODs and larger detection ranges for similar biosensor types. However, enhanced electrical performance alone does not guarantee improved biosensing performance. Careful selection of bioreceptors and device configuration is necessary, while Debye length engineering should also be considered for improved biosensing performance. Beyond biosensing and electrical performance, there are two additional considerations. First, is the environmental impact of fabrication, and second, is the industrial feasibility.

In this regard, several steps were taken throughout the thesis. First, a novel non-hazardous graphene-based material fabrication method was developed with the ability to tune the material's electrical properties. Second, the fabrication process was adjusted to optimize the electrical properties of the graphene-based FET device. Additionally, different sensing and biosensing strategies were employed using the graphene-based material and FET platform. Lastly, some biosensing performance enhancement strategies were examined.

The significant research outcomes of the thesis are summarised below:

- A novel laser ablation process was used on precursor GO and h-BN which are non-hazardous chemicals. This process allowed a simultaneous GO reduction and B/N co-doping. Control over the doping percentage was achieved by controlling precursor ratios in the solution. The B doping varied between 1.8-4.1 at%, while the N doping varied between 3.4-5.9 at%. This fabrication method preserves the mono- to few-layer nanoflakes structure but does not allow control over the doping sites. These nanoflakes could be used in micro-scale ultra-thin FET devices, but are incompatible with large-area ultrathin devices.
- The rGO thin films revealed an approximate 10^{-4} times decrease in sheet resistance compared to the precursor GO thin films. The sheet resistance decreased further for BN-rGO thin films with increased co-doping percentages. Lastly, it was found that devices with a longer channel length had higher sheet resistance, as a result of a larger number of grain boundaries.
- A novel laser ablation process was used to transform insulating 2D materials (GO and h-BN) in a solution into a 3D gel structure. The laser ablation process restored the conjugation and co-doped the GO gels with boron and nitrogen up to a total concentration of 2.3 at%. A top-channel BN-GO gel FET with a channel length of 100 µm demonstrated a charge carrier mobility comparable to short-channel (1-2 µm) pristine graphene, and an I_{ON}/I_{OFF} ratio 1000 times higher than the state-of-the-art with a single exception. The improved electrical performance was attributed to the restored conjugation and reduced number of grain boundaries as a direct result of the gel formation. The BN-GO gels demonstrated good stability over a 2-year period and good repeatability.
- Electrical performance enhancement strategies such as reducing the pulse duration during the laser ablation process, increasing the volume fraction of h-BN precursor, decreasing the channel length, and introducing an h-BN buffer layer between the gel and the substrate were employed. It was found that reducing the pulse duration increases the charge carrier mobility to that of theoretical values of pristine graphene. Additionally, using an h-BN buffer layer between the gel and the SiO_2/Si substrate demonstrated some hole mobility enhancement.

- An FET using a BN-GO gel channel was used as a real-time heart failure biosensor. The channel was covalently functionalized with BNP antibodies. The biosensor gave real-time detection of BNP biomarker in a buffer in as little as 5 seconds with an LOD of 10 fM and a detection range of 10 fM – 1 pM. The biosensor demonstrated 40 times higher sensitivity towards BNP compared to K^+ OH^- ions.
- An FET using a BN-GO gel channel functionalized with BNP antibodies was used as a heart failure biosensor using Dirac point monitoring. The biosensor was able to detect BNP with an LOD of 10 aM within 2 minutes. It also had a superior detection range stretching over 11 orders of magnitude (10 aM – 1 μM). The biosensor was highly selective to BNP compared with HER2 proteins, demonstrating10 times higher detection signal towards BNP. The biosensing capabilities compared with the state-of-the-art HF FETs biosensors were attributed to the improved electrical properties of the device and the increased Debye screening length.
- BN-GO gels were used as the receptor materials in a membrane-type surface stress sensor targeting a large array of gases including volatile organic compounds. The sensitivity and the LOD of these sensors were tested for each gas and compared to other receptors consisting of 2D materials. It was found that the sensitivity of the sensor is enhanced for gels containing higher concentrations of B and N co-doping. In addition, it was found that sensors using BN-GO gels as the receptor material had improved LODs compared with other 2D materials receptors such as GO gel, MoS_2, and WS_2. Overall, the BN-GO MSS sensor showed the lowest LOD of 0.001 ppm and the highest sensitivity of 16.85±0.01 μV/ppm for Hexanol.
- A BN-GO gel FET was covalently functionalized with COVID-19 antibodies in different buffers. The device demonstrated the best antibody attachment results after 48 hours of incubation in antibody solution in a pH=7 buffet at 4 ˚C. Poorer antibody functionalization was observed for different buffers (0.1x pH=7 and 0.1x and x0.0.1 PBS) and different incubation times (24 and 72 hours).
- A BN-GO gel FET covalently functionalized with COVID-19 antibodies was used for COVID-19 biosensing in buffer as a proof-of-concept by Dirac shift monitoring. The best biosensing performance in terms of stability and detection range was observed for 0.1x pH=7 buffer solution, and the LOD and detection range were calculated as ~30 fg/mL and 0.01-100 pg/mL, respectively.

7.2 Future work

7.2.1 FET biosensor arrays

The idea of creating an FET biosensor array capable to detect a range of biomarkers or DNA molecules is not new [9],[162]. However, the incorporation of BN-GO gel in such an array has not been previously tested. In this regard, an FET biosensor device could be designed to have multiple BN-GO channels covalently functionalized to different biomarkers. By monitoring the Dirac point change of each channel separately a disease could be diagnosed, prognosed, and the proper treatment plan could be planned [170]. For example, breast cancer has a large array of biomarkers, each used for a different classification (i.e., prognostic, therapeutic, or diagnostic). Thus, each channel could be functionalized with a different biomarker to allow health professionals to best plan the required course of action. Each device could be used for a different disease monitoring based on the biomarkers used.

7.2.2 Wearable devices

Packaging is another consideration that should be further investigated. Several diseases, such as diabetes require constant monitoring [171]. While viral diseases such as COVID-19 should optimally be diagnosed as soon as infection occurs [77]. It is therefore favorable to design wearable biosensors capable of giving real-time information. It is suggested to design a BN-GO FET biosensor which could be worn as a bracelet to continuously monitor desired biomarkers in sweat [171] or blood [172].

7.2.3 Transparent electrodes

Laser ablation is a useful tool for the fabrication and processing of nanomaterials [95]. It could also be used as a way to form 2D materials into 3D structures [130] or into 1D nanorods [173]. In this study [173], an array of 2D materials (including graphene, WS_2, and MoS_2) were ablated at a beam power of 0.25 W for different lengths of time (5-60 min). It was found that the 2D structures grow in length and reduce in width in as little as 5 min. These nanorods continue growing up to 20-25 min of ablation time, at which point they start to dissociate. The fabricated WS_2 nanorods were studied for transparent electrode applications, and they demonstrated increased electrical current and increased transparency compared to the precursor WS_2 nanoflakes. It is therefore suggested to investigate different laser powers to find the optimal growth conditions of the different 2D materials. The nanorods with the best aspect ratios could be further studied for transparent electrode applications.

Bibliography

[1] H.R. and M. Roser, Causes of Death, Our World Data. (2018). https://ourworldindata.org/causes-of-death.

[2] COVID-19 Coronavirus Pandemic, Worldmeter. (2020). https://www.worldometers.info/coronavirus/.

[3] and X.C. Magdalena Swierczewskaa, Gang Liua, Seulki Leea, High-sensitivity nanosensors for biomarker detection, Chem. Soc. Rev. 41 (2012) 2641–2655. doi:10.1002/bmb.20244.DNA.

[4] D.S. Allam, Z., Dey, G. and Jones, Artificial intelligence (AI) provided early detection of the coronavirus (COVID-19) in China and will influence future Urban health policy internationally, AI. 1(2) (2020) 156–165.

[5] S. Mansouri Majd, A. Salimi, Ultrasensitive flexible FET-type aptasensor for CA 125 cancer marker detection based on carboxylated multiwalled carbon nanotubes immobilized onto reduced graphene oxide film, Anal. Chim. Acta. 1000 (2018) 273–282. doi:10.1016/j.aca.2017.11.008.

[6] Z. Li, I.R. Ausri, Y. Zilberman, X.S. Tang, Towards label-free, wash-free and quantitative B-type natriuretic peptide detection for heart failure diagnosis, Nanoscale. 11 (2019) 18347–18357. doi:10.1039/c9nr05386g.

[7] M.T. Hwang, M. Heiranian, Y. Kim, S. You, J. Leem, A. Taqieddin, V. Faramarzi, Y. Jing, I. Park, A.M. van der Zande, S. Nam, N.R. Aluru, R. Bashir, Ultrasensitive detection of nucleic acids using deformed graphene channel field effect biosensors, Nat. Commun. 11 (2020) 1543. doi:10.1038/s41467-020-15330-9.

[8] I. Novodchuk, M. Bajcsy, M. Yavuz, Graphene-based field effect transistor biosensors for breast cancer detection: A review on biosensing strategies, Carbon N. Y. 172 (2021) 431–453. doi:10.1016/j.carbon.2020.10.048.

[9] G. Xu, J. Abbott, L. Qin, K.Y.M. Yeung, Y. Song, H. Yoon, J. Kong, D. Ham, Electrophoretic and field-effect graphene for all-electrical DNA array technology, Nat. Commun. 5 (2014) 1–9. doi:10.1038/ncomms5866.

[10] S. V. Morozov, K.S. Novoselov, M.I. Katsnelson, F. Schedin, D.C. Elias, J.A. Jaszczak, A.K.

Geim, Giant intrinsic carrier mobilities in graphene and its bilayer, Phys. Rev. Lett. 100 (2008) 11–14. doi:10.1103/PhysRevLett.100.016602.

[11] W. Choi, I. Lahiri, R. Seelaboyina, Y.S. Kang, Synthesis of graphene and its applications: A review, Crit. Rev. Solid State Mater. Sci. 35 (2010) 52–71. doi:10.1080/10408430903505036.

[12] and F.W. Zhang, Yuanbo, Tsung-Ta Tang, Caglar Girit, Zhao Hao, Michael C. Martin, Alex Zettl, Michael F. Crommie, Y. Ron Shen, Direct observation of a widely tunable bandgap in bilayer graphene, Nature. 459 (2009) 820–823.

[13] D. Reddy, L.F. Register, G.D. Carpenter, S.K. Banerjee, Graphene field-effect transistors, J. Phys. D. Appl. Phys. 45 (2012) 019501. doi:10.1088/0022-3727/45/1/019501.

[14] P.A. Denis, Band gap opening of monolayer and bilayer graphene doped with aluminium, silicon, phosphorus, and sulfur, Chem. Phys. Lett. 492 (2010) 251–257. doi:10.1016/j.cplett.2010.04.038.

[15] O.S. Kwon, S.J. Park, J.Y. Hong, A.R. Han, J.S. Lee, J.S. Lee, J.H. Oh, J. Jang, Flexible FET-Type VEGF aptasensor based on nitrogen-doped graphene converted from conducting polymer, ACS Nano. 6 (2012) 1486–1493. doi:10.1021/nn204395n.

[16] A.K.-B.L. Sung Myung, Aniruddh Solanki, Cheoljin Kim, Jaesung Park, Kwang S. Kim, Graphene-Encapsulated Nanoparticle-Based Biosensor for the Selective Detection of Cancer Biomarkers, Adv Mater. 23 (2011) 2221–2225. doi:10.1038/jid.2014.371.

[17] M.A. Stolyarov, G. Liu, S.L. Rumyantsev, M. Shur, A.A. Balandin, Suppression of 1/ f noise in near-ballistic h -BN-graphene- h- BN heterostructure field-effect transistors, Appl. Phys. Lett. 107 (2015) 28–33. doi:10.1063/1.4926872.

[18] I. Lee, J.N. Kim, W.T. Kang, Y.S. Shin, B.H. Lee, W.J. Yu, Schottky Barrier Variable Graphene/Multilayer-MoS2 Heterojunction Transistor Used to Overcome Short Channel Effects, ACS Appl. Mater. Interfaces. 12 (2020) 2854–2861. doi:10.1021/acsami.9b18577.

[19] S. Mittal, H. Kaur, N. Gautam, A.K. Mantha, Biosensors for breast cancer diagnosis: A review of bioreceptors, biotransducers and signal amplification strategies, Biosens. Bioelectron. 88 (2017) 217–231. doi:10.1016/j.bios.2016.08.028.

[20] S. Some, J. Kim, K. Lee, A. Kulkarni, Y. Yoon, S. Lee, T. Kim, H. Lee, Highly Air-Stable Phosphorus-Doped n-Type Graphene Field-Effect Transistors, Adv. Mater. 24 (2012) 5481–

5486. doi:10.1002/adma.201202255.

[21] C. Xu, X. Shi, A. Ji, L. Shi, C. Zhou, Y. Cui, Fabrication and characteristics of reduced graphene oxide produced with different green reductants, PLoS One. 10 (2015). doi:10.1371/journal.pone.0144842.

[22] Graphene Supermarket, (2021). https://graphene-supermarket.com/home.php.

[23] P. Russo, A. Hu, G. Compagnini, W.W. Duley, N.Y. Zhou, Femtosecond laser ablation of highly oriented pyrolytic graphite: A green route for large-scale production of porous graphene and graphene quantum dots, Nanoscale. 6 (2014) 2381–2389. doi:10.1039/c3nr05572h.

[24] R. Campos, J. Borme, J.R. Guerreiro, G. Machado, M.F. Cerqueira, D.Y. Petrovykh, P. Alpuim, Attomolar label-free detection of dna hybridization with electrolyte-gated graphene field-effect transistors, ACS Sensors. 4 (2019) 286–293. doi:10.1021/acssensors.8b00344.

[25] B. Zhan, C. Li, J. Yang, G. Jenkins, W. Huang, X. Dong, Graphene field-effect transistor and its application for electronic sensing, Small. 10 (2014) 4042–4065. doi:10.1002/smll.201400463.

[26] M.A. Morales, J.M. Halpern, Guide to Selecting a Biorecognition Element for Biosensors, Bioconjug. Chem. 29 (2018) 3231–3239. doi:10.1021/acs.bioconjchem.8b00592.

[27] A.B.A.E.Y.A. XU DU, IVAN SKACHKO, Approaching ballistic transport in suspended graphene, Nat. Nanotechnol. 3 (2008) 491–495. doi:10.1038/nnano.2008.199.

[28] V.B. Mohan, K. tak Lau, D. Hui, D. Bhattacharyya, Graphene-based materials and their composites: A review on production, applications and product limitations, Compos. Part B Eng. 142 (2018) 200–220. doi:10.1016/j.compositesb.2018.01.013.

[29] Y. Huang, E. Sutter, N.N. Shi, J. Zheng, T. Yang, D. Englund, H.J. Gao, P. Sutter, Reliable Exfoliation of Large-Area High-Quality Flakes of Graphene and Other Two-Dimensional Materials, ACS Nano. 9 (2015) 10612–10620. doi:10.1021/acsnano.5b04258.

[30] R. Mertens, Sony developed a new R2R method to make graphene, produced a 100-meter long sheet, Graphene-Info. (n.d.). https://www.graphene-info.com/sony-developed-new-r2r-method-make-graphene-produced-100-meter-long-sheet.

[31] J. Li, J.-F. Hsu, H. Lee, S. Tripathi, Q. Guo, L. Chen, M. Huang, S. Dhingra, J.-W. Lee, C.-B.

Eom, P. Irvin, J. Levy, B. D'Urso, Method for Transferring High-Mobility CVD-Grown Graphene with Perfluoropolymers, ArXiv Prepr. ArXiv1606.08802. 1 (2016) 1–6.

[32] X.D. Yanbing Yang, Xiangdong Yang, Xuming Zou, Shiting Wu, Da Wan, Anyuan Cao, Lei Liao, Quan Yuan, Ultrafine Graphene Nanomesh with Large On Off Ratio for High-Performance Flexible Biosensors, Adv. Funct. Mater. 2017, 27, 1604096. 27 (2017) 1604096.

[33] R. Ma, Q. Huan, L. Wu, J. Yan, W. Guo, Y.Y. Zhang, S. Wang, L. Bao, Y. Liu, S. Du, S.T. Pantelides, H.J. Gao, Direct Four-Probe Measurement of Grain-Boundary Resistivity and Mobility in Millimeter-Sized Graphene, Nano Lett. 17 (2017) 5291–5296. doi:10.1021/acs.nanolett.7b01624.

[34] H.H. Choi, J. Park, S. Huh, S.K. Lee, B. Moon, S.W. Han, C. Hwang, K. Cho, Photoelectric Memory Effect in Graphene Heterostructure Field- Effect Transistors Based on Dual Dielectrics, ACS Photonics. 5 (2018) 329–336. doi:10.1021/acsphotonics.7b01132.

[35] E. Diez, T. Taniguchi, K. Watanabe, T. Otsuji, Y.M. Meziani, Asymmetric Dual Grating Gate Graphene-based THz detectors, IEEE. (2019).

[36] 조인수, Optimizing the Electrical Properties of CVD Graphene by Substrate and Doping Control, (Doctoral Diss. 서울대학교 대학원). (2017).

[37] D. Nguyen, W. Chiang, Y. Su, M. Hofmann, Y. Hsieh, Solid-diffusion-facilitated cleaning of copper foil improves the quality of CVD graphene, Sci. Rep. 9(1) (2019) 1–6. doi:10.1038/s41598-018-36390-4.

[38] F. Zhang, X. Chen, C. Yu, X. Xu, X. Hu, X. Qin, Q. Li, X. Zhao, P. Yu, R. Wang, High mobility and large domain decoupled epitaxial graphene on SiC surface obtained by nearly balanced hydrogen etching, Mater. Lett. 195 (2017) 82–85. doi:10.1016/j.matlet.2017.02.105.

[39] R.E. Obrzut, J., White, K., Yang, Y. and EImquist, Characterization of Graphene Conductance Using a Microwave Cavity, 2018 IEEE 13th Nanotechnol. Mater. Devices Conf. (Pp. 1-4). (2018).

[40] C. Melios, M. Winters, W. Strupiński, V. Panchal, C.E. Giusca, K.D.G. Imalka Jayawardena, N. Rorsman, S.R.P. Silva, O. Kazakova, Tuning epitaxial graphene sensitivity to water by hydrogen intercalation, Nanoscale. 9 (2017) 3440–3448. doi:10.1039/c6nr09465a.

[41] N. Fatihah, T. Arifin, M. Aziz, Effect of reduction time on optical properties of reduced

graphene oxide, J. Teknol. 79 (2017) 25–28. doi:10.11113/jt.v79.10432.

[42] C.J. Shih, Q.H. Wang, Y. Son, Z. Jin, D. Blankschtein, M.S. Strano, Tuning on-off current ratio and field-effect mobility in a MoS 2-graphene heterostructure via schottky barrier modulation, ACS Nano. 8 (2014) 5790–5798. doi:10.1021/nn500676t.

[43] Y.L. JIA-NAN MA, YAN HE, D.-D. HAN, A.Y.-L.Z. YU-QING LIU, JIANG-WEI MAO, HAO-BO JIANG, Facile fabrication of flexible graphene FETs by sunlight reduction of graphene oxide, 42 (2017) 3403–3406. doi:10.1364/OL.42.003403.

[44] H. Chen, P. Chen, J. Huang, R. Selegård, M. Platt, A. Palaniappan, D. Aili, A.I.Y. Tok, B. Liedberg, Detection of Matrilysin Activity Using Polypeptide Functionalized Reduced Graphene Oxide Field-Effect Transistor Sensor, Anal. Chem. 88 (2016) 2994–2998. doi:10.1021/acs.analchem.5b04663.

[45] A. Haque, A. Mamun, M.F.N. Taufique, P. Karnati, K. Ghosh, Properties of High Carrier Mobility Reduced Graphene Oxide Thin Film Devices, IEEE Trans. Semicond. Manuf. 31 (2018) 535–544.

[46] H. Juvaid, M.M., Sarkar, S., Gogoi, P.K., Ghosh, S., Annamalai, M., Lin, Y.C., Prakash, S., Goswami, S., Li, C., Hooda, S. and Jani, Direct Growth of Wafer-Scale, Transparent, p-Type Reduced-Graphene-Oxide-like Thin Films by Pulsed Laser Deposition. ., ACS Nano. 14(3) (2020) 3290–3298.

[47] F. Khan, S.H. Baek, J.H. Kim, One-step and controllable bipolar doping of reduced graphene oxide using TMAH as reducing agent and doping source for field effect transistors, Carbon N. Y. 100 (2016) 608–616. doi:10.1016/j.carbon.2016.01.064.

[48] and X.Y.C. J. X. Wan, Y. You, Y. L. Xu, C. Wang, P. B. Zhang, X. Y. Jiang, X. H. Fang, L. Y. Yang, Synthesis of nitrogen-doped graphene via pentachloropyridine as the sole solid source, Appl. Phys. Lett. 033106 (2017). doi:10.1063/1.4995228.

[49] E. Vaziri, S., Chen, V., Cai, L., Jiang, Y., Chen, M.E., Grady, R.W., Zheng, X. and Pop, Ultrahigh Doping of Graphene Using Flame-Deposited MoO3, IEEE Electron Device Lett. 41(10) (2020) 1592–1595.

[50] L. Banszerus, M. Schmitz, S. Engels, J. Dauber, M. Oellers, F. Haupt, K. Watanabe, T. Taniguchi, B. Beschoten, C. Stampfer, Ultrahigh-mobility graphene devices from chemical

vapor deposition on reusable copper, Sci. Adv. 1 (2015) 1–7. doi:10.1126/sciadv.1500222.

[51] E. Kim, N. Jain, R. Jacobs-gedrim, Y. Xu, B. Yu, Exploring carrier transport phenomena in a CVD-assembled graphene FET on hexagonal boron nitride, Nanotechnology. 23 (2012) (2012). doi:10.1088/0957-4484/23/12/125706.

[52] Rajesh, Z. Gao, R. Vishnubhotla, P. Ducos, M.D. Serrano, J. Ping, M.K. Robinson, A.T.C. Johnson, Genetically Engineered Antibody Functionalized Platinum Nanoparticles Modified CVD-Graphene Nanohybrid Transistor for the Detection of Breast Cancer Biomarker, HER3, Adv. Mater. Interfaces. 3 (2016) 1–8. doi:10.1002/admi.201600124.

[53] C. Zhang, J.Q. Xu, Y.T. Li, L. Huang, D.W. Pang, Y. Ning, W.H. Huang, Z. Zhang, G.J. Zhang, Photocatalysis-Induced Renewable Field-Effect Transistor for Protein Detection, Anal. Chem. 88 (2016) 4048–4054. doi:10.1021/acs.analchem.6b00374.

[54] X. Song, Y. Zhang, H. Zhang, Y. Yu, M. Cao, J. Wang, X. Ding, J. Yao, O. Devices, Improved hybrid polymer/PbS quantum dot infrared phototransistors incorporating single-layer graphene, Proc. SPIE. SPIE/COS P (n.d.). doi:10.1117/12.2242775.

[55] Z. Zuo, Z. Xu, R. Zheng, A. Khanaki, J. Zheng, In-situ epitaxial growth of graphene / h-BN van der Waals heterostructures by molecular beam epitaxy, Nat. Sci. Reports. 5 (2015) 1–6. doi:10.1038/srep14760.

[56] L. Zhou, H. Mao, C. Wu, L. Tang, Z. Wu, H. Sun, H. Zhang, H. Zhou, C. Jia, Q. Jin, X. Chen, J. Zhao, Label-free graphene biosensor targeting cancer molecules based on non-covalent modification, Biosens. Bioelectron. 87 (2017) 701–707. doi:10.1016/j.bios.2016.09.025.

[57] K.S. Novoselov, A.K. Geim, S. V. Morozov, D. Jiang, M.I. Katsnelson, I. V. Grigorieva, S. V. Dubonos, A.A. Firsov, Two-dimensional gas of massless Dirac fermions in graphene, Nature. 438 (2005) 197–200. doi:10.1038/nature04233.

[58] M.Y. Shen, B.R. Li, Y.K. Li, Silicon nanowire field-effect-transistor based biosensors: From sensitive to ultra-sensitive, Biosens. Bioelectron. 60 (2014) 101–111. doi:10.1016/j.bios.2014.03.057.

[59] M.S. Belluzo, M.É. Ribone, C.M. Lagier, Assembling amperometric biosensors for clinical diagnostics, Sensors. 8 (2008) 1366–1399. doi:10.3390/s8031366.

[60] S. Mansouri Majd, A. Salimi, Ultrasensitive flexible FET-type aptasensor for CA 125 cancer

marker detection based on carboxylated multiwalled carbon nanotubes immobilized onto reduced graphene oxide film, Anal. Chim. Acta. 1000 (2018) 273–282. doi:10.1016/j.aca.2017.11.008.

[61] X. Wei, Porous silicon waveguide biosensors with a grating coupler, Vanderbilt Univ. (2012).

[62] B. Abraham-Shrauner, Models for Electrostatic Interactions Between Protein Molecules and Surfaces Involved in Blood Clot Formation, Math. Biosci. 20 (1974) 85–103.

[63] M. Park, J., Nguyen, H.H., Woubit, A. and Kim, Applications of field-effect transistor (FET)-type biosensors, Appl. Sci. Converg. Technol. 23(2) (2014) 61–71.

[64] N. Gao, T. Gao, X. Yang, X. Dai, W. Zhou, A. Zhang, C.M. Lieber, Specific detection of biomolecules in physiological solutions using graphene transistor biosensors, Proc. Natl. Acad. Sci. U. S. A. 113 (2016) 14633–14638. doi:10.1073/pnas.1625010114.

[65] Z. Wang, Y. Jia, Graphene solution-gated field effect transistor DNA sensor fabricated by liquid exfoliation and double glutaraldehyde cross-linking, Carbon N. Y. 130 (2018) 758–767. doi:10.1016/j.carbon.2018.01.078.

[66] Z. Gao, H. Xia, J. Zauberman, M. Tomaiuolo, J. Ping, Q. Zhang, P. Ducos, H. Ye, S. Wang, X. Yang, F. Lubna, Z. Luo, L. Ren, A.T.C. Johnson, Detection of Sub-fM DNA with Target Recycling and Self-Assembly Amplification on Graphene Field-Effect Biosensors, Nano Lett. 18 (2018) 3509–3515. doi:10.1021/acs.nanolett.8b00572.

[67] S. Chen, Y. Sun, Y. Xia, K. Lv, B. Man, C. Yang, Donor effect dominated molybdenum disulfide / graphene nanostructure-based field-effect transistor for ultrasensitive DNA detection, Biosens. Bioelectron. 156 (2020) 1–7. doi:10.1016/j.bios.2020.112128.

[68] and J.W. Z., Tian, M., Xu, S., Zhang, J., Wang, X., Li, Z., Liu, H., Song, R., Yu, RNA Detection Based on Graphene Field-Effect Transistor Biosensor, Hindawi. 2018 (2018).

[69] M. Tian, M. Qiao, C. Shen, F. Meng, L.A. Frank, V. V Krasitskaya, T. Wang, X. Zhang, R. Song, Y. Li, Highly-sensitive graphene field effect transistor biosensor using PNA and DNA probes for RNA detection, Appl. Surf. Sci. 527 (2020). doi:10.1016/j.apsusc.2020.146839.

[70] Y. Yang, X. Yang, X. Zou, S. Wu, D. Wan, A. Cao, L. Liao, Q. Yuan, X. Duan, Ultrafine Graphene Nanomesh with Large On/Off Ratio for High-Performance Flexible Biosensors, Adv. Funct. Mater. 27 (2017) 1–9. doi:10.1002/adfm.201604096.

[71] S. Hideshima, K. Fujita, Y. Harada, M. Tsuna, Y. Seto, S. Sekiguchi, S. Kuroiwa, T. Nakanishi, T. Osaka, Signal amplification in electrochemical detection of buckwheat allergenic protein using field effect transistor biosensor by introduction of anionic surfactant, Sens. Bio-Sensing Res. 7 (2016) 90–94. doi:10.1016/j.sbsr.2016.01.011.

[72] C.H. Yeh, V. Kumar, D.R. Moyano, S.H. Wen, V. Parashar, S.H. Hsiao, A. Srivastava, P.S. Saxena, K.P. Huang, C.C. Chang, P.W. Chiu, High-performance and high-sensitivity applications of graphene transistors with self-assembled monolayers, Biosens. Bioelectron. 77 (2016) 1008–1015. doi:10.1016/j.bios.2015.10.078.

[73] Y.M. Lei, M.M. Xiao, Y.T. Li, L. Xu, H. Zhang, Z.Y. Zhang, G.J. Zhang, Detection of heart failure-related biomarker in whole blood with graphene field effect transistor biosensor, Biosens. Bioelectron. 91 (2017) 1–7. doi:10.1016/j.bios.2016.12.018.

[74] M. Khosravi-Nejad, F., Teimouri, M., Marandi, S. J., & Shariati, The highly sensitive impedimetric biosensor in label free approach for hepatitis B virus DNA detection based on tellurium doped ZnO nanowires, Appl. Phys. A. 125(9) (2019) 616.

[75] J. Basu, C. Roychaudhuri, S. Member, Attomolar Sensitivity of FET Biosensor Based on Smooth and Reliable Graphene Nanogrids, 492 IEEE ELECTRON DEVICE Lett. 37 (2016) 492–495.

[76] J. Basu, N. Samanta, S. Jana, C. Roychaudhuri, Towards reliability enhancement of graphene FET biosensor in complex analyte : Arti fi cial neural network approach, Microelectron. Reliab. 91 (2018) 154–159. doi:10.1016/j.microrel.2018.09.001.

[77] G. Seo, G. Lee, M.J. Kim, S.H. Baek, M. Choi, K.B. Ku, C.S. Lee, S. Jun, D. Park, H.G. Kim, S.J. Kim, J.O. Lee, B.T. Kim, E.C. Park, S. Il Kim, Rapid Detection of COVID-19 Causative Virus (SARS-CoV-2) in Human Nasopharyngeal Swab Specimens Using Field-Effect Transistor-Based Biosensor, ACS Nano. 14 (2020) 5135–5142. doi:10.1021/acsnano.0c02823.

[78] S. Hun, K. Ho, S. Eun, S. Joo, O. Seok, Cytochrome C-decorated graphene field-effect transistor for highly sensitive hydrogen peroxide detection, J. Ind. Eng. Chem. 83 (2020) 29–34. doi:10.1016/j.jiec.2019.11.009.

[79] Z. Chen, F.W., Ilatikhameneh, H., Klimeck, G., Rahman, R., Chu, T. and Chen, Achieving a higher performance in bilayer graphene FET-strain engineering., in: 2015 Int. Conf. Simul.

Semicond. Process. Devices IEEE, 2015: pp. 177–181.

[80] R. Verona, M.D., Verdolino, V., Palazzesi, F. and Corradini, Focus on PNA Flexibility and RNA binding using molecular dynamics and metadynamics, Sci. Rep. 7 (2017) 42799.

[81] K.S. Novoselov, S. V. Morozov, D. Jiang, Y. Zhang, S. V. Dubonos, I. V. Grigorieva, A.A. Firsov, A.K. Geim, Electric Field Effect in Atomically Thin Carbon Films, Science (80-.). 306 (2004) 666–669.

[82] J. Ma, H. Zhu, W. Huang, T. Lin, X. Pan, W. Wang, Graphene nanoribbons from tetraphenylethene-based polymeric precursor: Chemical synthesis and application in thin-film field-effect transistor, Chinese J. Chem. 33 (2015) 1380–1388. doi:10.1002/cjoc.201500672.

[83] V. Georgakilas, K. Vrettos, K. Katomeri, A. Kouloumpis, K. Dimos, D. Gournis, R. Zboril, Highly dispersible disk-like graphene nanoflakes, Nanoscale. 7 (2015) 15059–15064. doi:10.1039/C5NR04422G.

[84] P.T. Yin, S. Shah, M. Chhowalla, K.B. Lee, Design, synthesis, and characterization of graphene-nanoparticle hybrid materials for bioapplications, Chem. Rev. 115 (2015) 2483–2531. doi:10.1021/cr500537t.

[85] Y. Sun, Y. Cheng, K. He, A. Zhou, H. Duan, One-step synthesis of three-dimensional porous ionic liquid–carbon nanotube–graphene gel and MnO_2 –graphene gel as freestanding electrodes for asymmetric supercapacitors, RSC Adv. 5 (2015) 10178–10186. doi:10.1039/C4RA16071A.

[86] L. Ci, L. Song, C. Jin, D. Jariwala, D. Wu, Y. Li, A. Srivastava, Z.F. Wang, K. Storr, L. Balicas, F. Liu, P.M. Ajayan, Atomic layers of hybridized boron nitride and graphene domains, Nat. Mater. 9 (2010) 430–435. doi:10.1038/nmat2711.

[87] S. Umrao, T.K. Gupta, S. Kumar, V.K. Singh, M.K. Sultania, J.H. Jung, I.K. Oh, A. Srivastava, Microwave-Assisted Synthesis of Boron and Nitrogen co-doped Reduced Graphene Oxide for the Protection of Electromagnetic Radiation in Ku-Band, ACS Appl. Mater. Interfaces. 7 (2015) 19831–19842. doi:10.1021/acsami.5b05890.

[88] T. Schiros, D. Nordlund, L. Palova, L. Zhao, M. Levendorf, C. Jaye, D. Reichman, J. Park, M. Hybertsen, A. Pasupathy, Atomistic Interrogation of B-N Co-dopant Structures and Their Electronic Effects in Graphene, ACS Nano. 10 (2016) 6574–6584.

doi:10.1021/acsnano.6b01318.

[89] L.K. Putri, B.J. Ng, W.J. Ong, H.W. Lee, W.S. Chang, S.P. Chai, Heteroatom Nitrogen- and Boron-Doping as a Facile Strategy to Improve Photocatalytic Activity of Standalone Reduced Graphene Oxide in Hydrogen Evolution, ACS Appl. Mater. Interfaces. 9 (2017) 4558–4569. doi:10.1021/acsami.6b12060.

[90] Z. Song, Z. Li, H. Wang, X. Bai, W. Wang, H. Du, S. Liu, C. Wang, J. Han, Y. Yang, Z. Liu, J. Lu, Z. Fang, J. Yang, Valley Pseudospin with a Widely Tunable Bandgap in Doped Honeycomb BN Monolayer, Nano Lett. 17 (2017) 2079–2087. doi:10.1021/acs.nanolett.7b00271.

[91] S. Huang, L. Zhang, J. Zhu, S.P. Jiang, P.K. Shen, Crumpled nitrogen- and boron-dual-self-doped graphene sheets as an extraordinary active anode material for lithium ion batteries, J. Mater. Chem. A. 4 (2016) 14155–14162. doi:10.1039/C6TA05623G.

[92] Y. Sun, C. Du, G. Han, Y. Qu, L. Du, Y. Wang, G. Chen, Y. Gao, G. Yin, Boron, nitrogen co-doped graphene: a superior electrocatalyst support and enhancing mechanism for methanol electrooxidation, Electrochim. Acta. 212 (2016) 313–321. doi:10.1016/j.electacta.2016.06.168.

[93] I.T. Kim, M.J. Song, Y.B. Kim, M.W. Shin, Microwave-hydrothermal synthesis of boron/nitrogen co-doped graphene as an efficient metal-free electrocatalyst for oxygen reduction reaction, Int. J. Hydrogen Energy. 41 (2016) 22026–22033. doi:10.1016/j.ijhydene.2016.08.069.

[94] S. Elumalai, C.Y. Su, M. Yoshimura, Scalable One-Pot Synthesis of Nitrogen and Boron Co-doped Few Layered Graphene by Submerged Liquid Plasma Exfoliation, Front. Mater. 6 (2019) 1–6. doi:10.3389/fmats.2019.00216.

[95] I. Novodchuk, M. Irannejad, B. Wales, K. Ibrahim, J. Sanderson, M. Bajcsy, M. Yavuz, Controlled volume production of simultaneously B/N co-doped reduced graphene oxide nanoflakes using femtosecond laser ablation, Mater. Res. Bull. 111 (2019) 80–86. doi:10.1016/j.materresbull.2018.10.039.

[96] and A.B. Allmen, Martin V., Laser-beam interactions with materials: physical principles and applications, Springer Sci. Bus. Media. 2 (2013).

[97] J. Gao, F. Liu, Y. Liu, N. Ma, Z. Wang, X. Zhang, Environment-friendly method to produce graphene that employs vitamin C and amino acid, Chem. Mater. 22 (2010) 2213–2218. doi:10.1021/cm902635j.

[98] S. Yang, W. Yue, D. Huang, C. Chen, H. Lin, X. Yang, A facile green strategy for rapid reduction of graphene oxide by metallic zinc, RSC Adv. 2 (2012) 8827–8832. doi:10.1039/c2ra20746j.

[99] L. Graf, D., Molitor, F., Ensslin, K., Stampfer, C., Jungen, A., Hierold, C., & Wirtz, Spatially resolved Raman spectroscopy of single-and few-layer graphene, Nano Lett. 7(2) (2007) 238–242.

[100] L.M. Malard, M.A. Pimenta, G. Dresselhaus, M.S. Dresselhaus, Raman spectroscopy in graphene, Phys. Rep. 473 (2009) 51–87. doi:10.1016/j.physrep.2009.02.003.

[101] A.C. Ferrari, Raman spectroscopy of graphene and graphite: Disorder, electron-phonon coupling, doping and nonadiabatic effects, Solid State Commun. 143 (2007) 47–57. doi:10.1016/j.ssc.2007.03.052.

[102] F. Rosenburg, E. Ionescu, N. Nicoloso, R. Riedel, High-temperature Raman spectroscopy of nano-crystalline carbon in silicon oxycarbide, Materials (Basel). 11 (2018). doi:10.3390/ma11010093.

[103] E. Dervishi, Z. Ji, H. Htoon, M. Sykora, S.K. Doorn, Raman spectroscopy of bottom-up synthesized graphene quantum dots: Size and structure dependence, Nanoscale. 11 (2019) 16571–16581. doi:10.1039/c9nr05345j.

[104] B. Tang, H. Guoxin, H. Gao, Raman spectroscopic characterization of graphene, Appl. Spectrosc. Rev. 45 (2010) 369–407. doi:10.1080/05704928.2010.483886.

[105] V. Loryuenyong, K. Totepvimarn, P. Eimburanapravat, W. Boonchompoo, A. Buasri, Preparation and characterization of reduced graphene oxide sheets via water-based exfoliation and reduction methods, Adv. Mater. Sci. Eng. 2013 (2013). doi:10.1155/2013/923403.

[106] L. Röhrl, J., Hundhausen, M., Emtsev, K. V., Seyller, T., Graupner, R., & Ley, Raman spectra of epitaxial graphene on SiC (0001), Appl. Phys. Lett. 92(20) (2008) 201918.

[107] S. Perumbilavil, P. Sankar, T.P. Rose, R. Philip, S. Perumbilavil, P. Sankar, T.P. Rose, R. Philip, White light Z-scan measurements of ultrafast optical nonlinearity in reduced graphene

oxide nanosheets in the 400 – 700 nm region White light Z-scan measurements of ultrafast optical nonlinearity in reduced graphene oxide nanosheets in the 400 – 700 nm re, 051104 (2016). doi:10.1063/1.4928124.

[108] J. Zhang, C. Zhao, N. Liu, H. Zhang, J. Liu, Y.Q. Fu, B. Guo, Z. Wang, S. Lei, P.A. Hu, Tunable electronic properties of graphene through controlling bonding configurations of doped nitrogen atoms, Sci. Rep. 6 (2016). doi:10.1038/srep28330.

[109] Y. Liu, J. Li, W. Li, Y. Li, F. Zhan, H. Tang, Q. Chen, Exploring the nitrogen species of nitrogen doped graphene as electrocatalysts for oxygen reduction reaction in Al-air batteries, Int. J. Hydrogen Energy. 41 (2016) 10354–10365. doi:10.1016/j.ijhydene.2015.10.109.

[110] A. Kovtun, D. Jones, S. Dell'Elce, E. Treossi, A. Liscio, V. Palermo, Accurate chemical analysis of oxygenated graphene-based materials using X-ray photoelectron spectroscopy, Carbon N. Y. 143 (2019) 268–275. doi:10.1016/j.carbon.2018.11.012.

[111] G.S. Kang, S. Lee, D.C. Lee, C.W. Yoon, H.I. Joh, Edge-enriched graphene with boron and nitrogen co-doping for enhanced oxygen reduction reaction, Curr. Appl. Phys. 20 (2020) 456–461. doi:10.1016/j.cap.2020.01.008.

[112] A. Mannan, Y. Hirano, A.T. Quitain, M. Koinuma, T. Kida, Graphene Oxide to B , N Co-doped Graphene through Tris-dimethylaminoborane Complex by Hydrothermal Implantation, Am. J. Mater. Sci. 9 (2019) 22–28. doi:10.5923/j.materials.20190901.04.

[113] S.H. Dave, C. Gong, A.W. Robertson, J.H. Warner, J.C. Grossman, Chemistry and Structure of Graphene Oxide via Direct Imaging, ACS Nano. 10 (2016) 7515–7522. doi:10.1021/acsnano.6b02391.

[114] N. Koos, A.A., Dillon, F., Obraztsova, E.A., Crossley, A. and Grobert, Comparison of structural changes in nitrogen and boron-doped multi-walled carbon nanotubes, Carbon N. Y. 48 (2010) 3033–3041.

[115] and A.K.G. K. S. Novoselov, D. Jiang, F. Schedin, T. J. Booth, V. V. Khotkevich, S. V. Morozov, Two-dimensional atomic crystals, Proc. Natl. Acad. Sci. 102 (2005) 10451–10453. doi:10.1063/1.4797258.

[116] H. Tu, Y., Ichii, T., Khatri, O.P. and Sugimura, Reductive patterning of graphene oxide by vacuum–ultraviolet irradiation in high vacuum, Appl. Phys. Express. 7 (2014) 075101.

[117] R.V. Schwartz, L.W. and Roy, Theoretical and numerical results for spin coating of viscous liquids, Phys. Fluids. 16 (2004) 569–584.

[118] C. Reiner-Rozman, C. Kotlowski, W. Knoll, Electronic biosensing with functionalized rGO FETs, Biosensors. 6 (2016) 1–12. doi:10.3390/bios6020017.

[119] H.B. Mampallil, D. and Eral, A review on suppression and utilization of the coffee-ring effect, Adv. Colloid Interface Sci. 252 (2018) 38–54.

[120] G. Zhao, D. Shao, C. Chen, X. Wang, Synthesis of few-layered graphene by H2 O2 plasma etching of graphite, Appl. Phys. Lett. 98 (2011) 96–99. doi:10.1063/1.3589354.

[121] A.D. Bobadilla, L.E. Ocola, A. V. Sumant, M. Kaminski, J.M. Seminario, PMMA-Assisted Plasma Patterning of Graphene, J. Nanotechnol. 2018 (2018). doi:10.1155/2018/8349626.

[122] Y.-J. Hung, Y.-C. Liang, C.-W. Huang, J.-F. Shih, S. Hu, T.-H. Yen, C.-W. Kao, C.-H. Chen, Narrowband silicon waveguide Bragg reflector achieved by highly ordered graphene oxide gratings, Opt. Lett. 42 (2017) 4768. doi:10.1364/ol.42.004768.

[123] H. Park, G.H. Shin, K.J. Lee, S.Y. Choi, Atomic-scale etching of hexagonal boron nitride for device integration based on two-dimensional materials, Nanoscale. 10 (2018) 15205–15212. doi:10.1039/c8nr02451k.

[124] S. Park, J. An, J.R. Potts, A. Velamakanni, S. Murali, R.S. Ruoff, Hydrazine-reduction of graphite- and graphene oxide, Carbon N. Y. 49 (2011) 3019–3023. doi:10.1016/j.carbon.2011.02.071.

[125] L. Xie, L. Jiao, H. Dai, Selective etching of graphene edges by hydrogen plasma, J. Am. Chem. Soc. 132 (2010) 14751–14753. doi:10.1021/ja107071g.

[126] Y. Zhang, Z. Li, P. Kim, L. Zhang, C. Zhou, Anisotropic hydrogen etching of chemical vapor deposited graphene, ACS Nano. 6 (2012) 126–132. doi:10.1021/nn202996r.

[127] I. Childres, L.A. Jauregui, J. Tian, Y.P. Chen, Effect of oxygen plasma etching on graphene studied using Raman spectroscopy and electronic transport measurements, New J. Phys. 13 (2011). doi:10.1088/1367-2630/13/2/025008.

[128] F. Bonaccorso, A. Lombardo, T. Hasan, Z. Sun, L. Colombo, A.C. Ferrari, Production and processing of graphene and 2d crystals, Mater. Today. 15 (2012) 564–589. doi:10.1016/S1369-7021(13)70014-2.

[129] A. V. Zaretski, D.J. Lipomi, Processes for non-destructive transfer of graphene: Widening the bottleneck for industrial scale production, Nanoscale. 7 (2015) 9963–9969. doi:10.1039/c5nr01777g.

[130] I. Novodchuk, M. Kayaharman, K. Ibrahim, S. Al-Tuairqi, M. Irannejad, E. Abdel-Rahman, J. Sanderson, M. Bajcsy, M. Yavuz, B/N co-doped graphene oxide gel with extremely-high mobility and ION/IOFF for large-area field effect transistors, Carbon N. Y. 158 (2020) 624–630. doi:10.1016/j.carbon.2019.11.034.

[131] K.H. Ibrahim, M. Irannejad, M. Hajialamdari, A. Ramadhan, K.P. Musselman, J. Sanderson, M. Yavuz, A Novel Femtosecond Laser-Assisted Method for the Synthesis of Reduced Graphene Oxide Gels and Thin Films with Tunable Properties, Adv. Mater. Interfaces. 3 (2016) 1–10. doi:10.1002/admi.201500864.

[132] M.K. Filippidou, C.M. Loukas, G. Kaprou, E. Tegou, P. Petrou, S. Kakabakos, A. Tserepi, S. Chatzandroulis, Detection of BRCA1 gene on partially reduced graphene oxide biosensors, Microelectron. Eng. 216 (2019) 111093. doi:10.1016/j.mee.2019.111093.

[133] S.C. Hernández, F.J. Bezares, J.T. Robinson, J.D. Caldwell, S.G. Walton, Controlling the local chemical reactivity of graphene through spatial functionalization, Carbon N. Y. 60 (2013) 84–93. doi:10.1016/j.carbon.2013.03.059.

[134] T.V. Cuong, V.H. Pham, Q.T. Tran, J.S. Chung, E.W. Shin, J.S. Kim, E.J. Kim, Optoelectronic properties of graphene thin films prepared by thermal reduction of graphene oxide, Mater. Lett. 64 (2010) 765–767. doi:10.1016/j.matlet.2010.01.009.

[135] Y.F. Lu, S.T. Lo, J.C. Lin, W. Zhang, J.Y. Lu, F.H. Liu, C.M. Tseng, Y.H. Lee, C. Te Liang, L.J. Li, Nitrogen-doped graphene sheets grown by chemical vapor deposition: Synthesis and influence of nitrogen impurities on carrier transport, ACS Nano. 7 (2013) 6522–6532. doi:10.1021/nn402102y.

[136] H. Li, Y.J. Zeng, X.J. Hu, H.H. Zhang, S.C. Ruan, M.J. Van Bael, C. Van Haesendonck, Thickness-dependent magnetotransport: from multilayer graphene to few-layer graphene, Carbon N. Y. 124 (2017) 193–200. doi:10.1016/j.carbon.2017.08.017.

[137] M.K. Joo, J. Kim, J.H. Park, V.L. Nguyen, K.K. Kim, Y.H. Lee, D. Suh, Large-Scale Graphene on Hexagonal-BN Hall Elements: Prediction of Sensor Performance without

Magnetic Field, ACS Nano. 10 (2016) 8803–8811. doi:10.1021/acsnano.6b04547.

[138] Y. Yu, Z. Li, W. Wang, X. Guo, J. Jiang, H. Nan, Z. Ni, Investigation of multilayer domains in large-scale CVD monolayer graphene by optical imaging, J. Semicond. 38 (2017). doi:10.1088/1674-4926/38/3/033003.

[139] C. Mackin, T. Palacios, Large-scale sensor systems based on graphene electrolyte-gated field-effect transistors, Analyst. 141 (2016) 2704–2711. doi:10.1039/C5AN02328A.

[140] T. Wu, X. Zhang, Q. Yuan, J. Xue, G. Lu, Z. Liu, H. Wang, H. Wang, F. Ding, Q. Yu, X. Xie, M. Jiang, Fast growth of inch-sized single-crystalline graphene from a controlled single nucleus on Cu-Ni alloys, Nat. Mater. 15 (2016) 43–47. doi:10.1038/nmat4477.

[141] V. Miseikis, F. Bianco, J. David, M. Gemmi, V. Pellegrini, M. Romagnoli, C. Coletti, Deterministic patterned growth of high-mobility large-crystal graphene: A path towards wafer scale integration, 2D Mater. 4 (2017). doi:10.1088/2053-1583/aa5481.

[142] S.J. Jeong, S. Jo, J. Lee, K. Yang, H. Lee, C.S. Lee, H. Park, S. Park, Self-Aligned Multichannel Graphene Nanoribbon Transistor Arrays Fabricated at Wafer Scale, Nano Lett. 16 (2016) 5378–5385. doi:10.1021/acs.nanolett.6b01542.

[143] J.D. Buron, D.M.A. Mackenzie, D.H. Petersen, A. Pesquera, A. Centeno, P. Bøggild, A. Zurutuza, P.U. Jepsen, Terahertz wafer-scale mobility mapping of graphene on insulating substrates without a gate, Opt. Express. 23 (2015) 30721. doi:10.1364/OE.23.030721.

[144] J. Sun, Z. Chen, L. Yuan, Y. Chen, J. Ning, S. Liu, D. Ma, X. Song, M.K. Priydarshi, A. Bachmatiuk, M.H. Rümmeli, T. Ma, L. Zhi, L. Huang, Y. Zhang, Z. Liu, Direct Chemical-Vapor-Deposition-Fabricated, Large-Scale Graphene Glass with High Carrier Mobility and Uniformity for Touch Panel Applications, ACS Nano. 10 (2016) 11136–11144. doi:10.1021/acsnano.6b06066.

[145] M. Chen, G. Li, W. Li, D. Stekovic, B. Arkook, M.E. Itkis, A. Pekker, E. Bekyarova, R.C. Haddon, Large-scale cellulose-assisted transfer of graphene toward industrial applications, Carbon N. Y. 110 (2016) 286–291. doi:10.1016/j.carbon.2016.09.029.

[146] Z. Wang, P. Li, Y. Chen, J. Liu, H. Tian, J. Zhou, W. Zhang, Y. Li, Synthesis of nitrogen-doped graphene by chemical vapour deposition using melamine as the sole solid source of carbon and nitrogen, J. Mater. Chem. C. 2 (2014) 7396. doi:10.1039/C4TC00924J.

[147] H. Gao, L. Song, W. Guo, L. Huang, D. Yang, F. Wang, Y. Zuo, X. Fan, Z. Liu, W. Gao, R. Vajtai, K. Hackenberg, P.M. Ajayan, A simple method to synthesize continuous large area nitrogen-doped graphene, Carbon N. Y. 50 (2012) 4476–4482. doi:10.1016/j.carbon.2012.05.026.

[148] W. Xu, T.S. Lim, H.K. Seo, S.Y. Min, H. Cho, M.H. Park, Y.H. Kim, T.W. Lee, N-doped graphene field-effect transistors with enhanced electron mobility and air-stability, Small. 10 (2014) 1999–2005. doi:10.1002/smll.201303768.

[149] W.C. Shin, S. Seo, B.J. Cho, Highly air-stable electrical performance of graphene field effect transistors by interface engineering with amorphous fluoropolymer, Appl. Phys. Lett. 98 (2011) 2009–2012. doi:10.1063/1.3578396.

[150] A.H. Hamad, Effects of different laser pulse regimes (nanosecond, picosecond and femtosecond) on the ablation of materials for production of nanoparticles in liquid solution, High Energy Short Pulse Lasers. (2016) 305–325.

[151] I. Novodchuk, M. Kayaharman, I.R. Ausri, R. Karimi, X.S. Tang, I.A. Goldthorpe, J. Sanderson, M. Bajcsy, M. Yavuz, An ultrasensitive heart-failure BNP biosensor using B/N co-doped graphene oxide gel FET, Biosens. Bioelectron. 180 (2021) 113114. doi:10.1016/j.bios.2021.113114.

[152] K.P. Singh, D. Bhattacharjya, F. Razmjooei, J.S. Yu, Effect of pristine graphene incorporation on charge storage mechanism of three-dimensional graphene oxide: Superior energy and power density retention, Sci. Rep. 6 (2016) 1–10. doi:10.1038/srep31555.

[153] F.S. Kshirsagar SV, Singh B, Comparative study of human and animal hair in relation with diameter and medullary index, Indian J. Forensic Med. Pathol. 2(3):105â (2009).

[154] H. Alawieh, T. El Chemaly, S. Alam, M. Khraiche, Towards point-of-care heart failure diagnostic platforms: Bnp and nt-probnp biosensors, Sensors (Switzerland). 19 (2019) 1–25. doi:10.3390/s19225003.

[155] Y.K. Vilian, A.E., Kim, W., Park, B., Oh, S.Y., Kim, T., Huh, Y.S., Hwangbo, C.K. and Han, Efficient electron-mediated electrochemical biosensor of gold wire for the rapid detection of C-reactive protein: A predictive strategy for heart failure, Biosens. Bioelectron. 142 (2019).

[156] H.J. Jang, H.R.; Wark, A.W.; Baek, S.H.; Chung, B.H.; Lee, Ultrasensitive and ultrawide

range detection of a cardiac biomarker on a surface plasmon resonance platform., Anal. Chem. 86, 814–81 (2014).

[157] C. Ju, Q. Fan, Y. Jia, A novel biomedical sensor for tumor marker based on Flexible supported solution gated graphene field effective transistor, in: Int. Conf. Mater. Environ. Biol. Eng. (MEBE 2015), 2015: pp. 429–432. doi:10.2991/mebe-15.2015.101.

[158] N. Tsang, D. K. H., Lieberthal, T. J., Watts, C., Dunlop, I. E., Ramadan, S., Armando, E., & Klein, Chemically functionalised graphene FET biosensor for the label-free sensing of exosomes, Sci. Rep. 9(1) (2019) 1–10.

[159] X. Fu, H., & Liu, Experimental comparison of surface chemistries for biomolecule immobilization on paper-based microfluidic devices, J. Micromechanics Microengineering. 29(12) (2019) 124003.

[160] V. Georgakilas, M. Otyepka, A.B. Bourlinos, V. Chandra, N. Kim, K.C. Kemp, P. Hobza, R. Zboril, K.S. Kim, Functionalization of Graphene : Covalent and Non-Covalent Approaches , Derivatives and Applications, Chem. Rev. 112(11) (2012) 6156–6214. doi:10.1021/cr3000412.

[161] W. Yuan, Q., Wu, S., Ye, C., Liu, X., Gao, J., Cui, N., Guo, P., Lai, G., Wei, Q., Yang, M. and Su, Sensitivity enhancement of potassium ion (K+) detection based on graphene field-effect transistors with surface plasma pretreatment, Sensors Actuators B Chem. 285. (2019) 333–340.

[162] A. Sinha, T.Y. Tai, K.H. Li, P. Gopinathan, Y. Da Chung, I. Sarangadharan, H.P. Ma, P.C. Huang, S.C. Shiesh, Y.L. Wang, G. Bin Lee, An integrated microfluidic system with field-effect-transistor sensor arrays for detecting multiple cardiovascular biomarkers from clinical samples, Biosens. Bioelectron. 129 (2019) 155–163. doi:10.1016/j.bios.2019.01.001.

[163] W. Tian, X. Liu, W. Yu, Research progress of gas sensor based on graphene and its derivatives: A review, Appl. Sci. 8 (2018). doi:10.3390/app8071118.

[164] L. Xu, Y. Wen, S. Pandit, V.R.S.S. Mokkapati, I. Mijakovic, Y. Li, M. Ding, S. Ren, W. Li, G. Liu, Graphene-based biosensors for the detection of prostate cancer protein biomarkers: a review, BMC Chem. 13 (2019) 1–12. doi:10.1186/s13065-019-0611-x.

[165] K. Mistry, K.H. Ibrahim, I. Novodchuk, H.T. Ngo, G. Imamura, J. Sanderson, M. Yavuz, G.

Yoshikawa, K.P. Musselman, Nanomechanical Gas Sensing with Laser Treated 2D Nanomaterials, Adv. Mater. Technol. 2000704 (2020) 1–11. doi:10.1002/admt.202000704.

[166] M. Yoshikawa, G., Akiyama, T., Loizeau, F., Shiba, K., Gautsch, S., Nakayama, T., Vettiger, P., Rooij, N.F.D. and Aono, Two dimensional array of piezoresistive nanomechanical membrane-type surface stress sensor (MSS) with improved sensitivity, Sensors. 12(11) (2012) 15873–15887.

[167] S.I. Choi, C.H., Park, S.H. and Woo, Binary and ternary doping of nitrogen, boron, and phosphorus into carbon for enhancing electrochemical oxygen reduction activity, ACS Nano. 6(8) (2012) 7084–7091.

[168] W. Luo, E., Xiao, M., Ge, J., Liu, C. and Xing, Selectively doping pyridinic and pyrrolic nitrogen into a 3D porous carbon matrix through template-induced edge engineering: enhanced catalytic activity towards the oxygen reduction reaction, J. Mater. Chem. A. 5(41) (2017) 21709–21714.

[169] T.A. Sergeyeva, A.P. Soldatkin, A.E. Rachkov, M.I. Tereschenko, S.A. Piletsky, A. V El`skaya, β-Lactamase label-based potentiometric biosensor for α-2 interferon detection, Anal. Chim. Acta. 390 (1999) 73–81.

[170] S. Mittal, H. Kaur, N. Gautam, A.K. Mantha, Biosensors for breast cancer diagnosis: A review of bioreceptors, biotransducers and signal amplification strategies, Biosens. Bioelectron. 88 (2017) 217–231. doi:10.1016/j.bios.2016.08.028.

[171] N. Chauhan, T. Maekawa, D.N.S. Kumar, Graphene based biosensors - Accelerating medical diagnostics to new-dimensions, J. Mater. Res. 32 (2017) 2860–2882. doi:10.1557/jmr.2017.91.

[172] J.D. Newman, A.P.F. Turner, Home blood glucose biosensors: A commercial perspective, Biosens. Bioelectron. 20 (2005) 2435–2453. doi:10.1016/j.bios.2004.11.012.

[173] K. Ibrahim, I. Novodchuk, K. Mistry, M. Singh, C. Ling, J. Sanderson, M. Bajcsy, M. Yavuz, K.P. Musselman, Laser-Directed Assembly of Nanorods of 2D Materials, Small. 15 (2019) 1904415. doi:10.1002/smll.201904415.